Microsegregation in Manganese Steels

by

Altan Türkeli

Thesis submitted in fulfilment of the degree of
Doctor of Philosophy at the Department of Metallurgy
of the University of Sheffield

August 1989

To my parents

SUMMARY

Dendritic morphology and microsegregation in the ternary Fe- 1.6 % Mn - 0.1 to 0.8 % C alloys have been investigated by quenching the unidirectionally solidified specimens. The microprobe analysis of these specimens showed that the manganese segregation was significantly controlled by the back diffusion. This back diffusion was extremely high in the case of ferritic solidification whereas only a small rise in Cmin was obtained for the austenitic phase. It was found that the manganese microsegregation between the primary arms was always higher than between the secondary arms. The measured segregation ratios indicated a rise with increasing carbon content for both morphologies. No clear effect of cooling rate on segregation was seen for secondary arms and only a slight increase was recorded with increasing the cooling rate for primary arms. Secondary dendrite arms solidified to produce asymmetric distribution profiles (saw-tooth or TGZM effect).

Measurements of the secondary dendrite arms during growth showed that the rate of the coarsening in these manganese steels was higher than other steels resulting in high homogenization between the arms. No tertiary arms have been observed. The primary arms grew mainly in the so-called 'close packed' arrangement and their spacing did not change with time. By increasing the growth rate and the temperature gradient in the liquid a decrease in primary arm spacings was seen. The results agree well with available experimental data in the literature.

The microsegregation calculations obtained from the secondary dendrite arm coarsening model is in a very good agreement with

the experimental measurements. The same model without arm coarsening was applied to different primary arm morphologies and the predictions of these models are also in reasonable agreement with observations.

CONTENTS

CHAPTER 1 SOLIDIFICATION

1.1 Nucleation

1.1.1 Homogeneous nucleation

When a liquid cools, a change from liquid to solid may occur. This transformation is initiated by a nucleus. Volmer and Weber(1) developed a nucleation theory. Later, this theory was slightly changed by Becker and Doring(2). Both consider the embryo in the form of the number of atoms in a liquid. These embryos are continuously appearing and disappearing in liquid. The probability of the number of such embryo (Ni) containing na atoms in a system is given by both models as

$$N_i = na \exp\left(- \frac{\Delta G_v}{kT}\right) \qquad 1.1$$

where k Boltzmann's constant

T temperature

ΔG_v free energy of formation of new phase

The Volmer-Weber theory assumes that once a nucleus of the critical size obtains an additional atom,it always grows into a stable nucleus. This assumption is not strictly true. Becker and Doring recognized this fact and postulated a different theory. The addition of an atom or even several atoms, to a critical nucleus will certainly tend to make it more stable. However, this increase in stability has to be small. Therefore, an embryo that has grown slightly beyond the critical size always has a nearly equal chance of shrinking back and becoming smaller.

In thermodynamic terms, the nucleation is controlled by two

factors: the change in volume free energy (ΔG_v, - ve) and the change in surface free energy (σ_{sl} +ve). The formation of the solid/liquid interface retards the nucleation, therefore if the embryo is assumed to be spherical, the total free energy change of the formation can be expressed as :

$$\Delta G_T = 4 \pi r^2 \sigma_{sl} + \frac{4}{3} \pi r^3 \Delta G_v \qquad 1.2$$

where σ_{sl} surface energy of interface between liquid and solid

ΔG_v volume energy

r radius of sphere

The volume free energy driving force (ΔG_v) can be related directly to the undercooling(ΔT) by

$$\Delta G_v = -\frac{L}{T_m} \Delta T \qquad 1.3$$

where L latent heat of fusion

Tm equilibrium melting temperature

The maximum as a function of size ΔG_T^m can be calculated from $\frac{\partial \Delta G_T}{\partial r} = 0$ this gives the critical embryo size

$$r_c = \frac{2 \sigma_{sl}}{\Delta G_v} \qquad 1.4$$

and correspondingly

$$\Delta G_T^m = \frac{16 \Pi \sigma_{sl}}{3 (\Delta G_v)^2} \qquad 1.5$$

When undercooling is increased in liquid, the total free energy barrier is reduced and therefore nucleation starts easier.

Turnbull and Fisher investigated the undercooling required for homogeneous nucleation in pure melts. They obtained undercoolings generally equivalent to about 0.2 Tm(3). These undercoolings have been increased using new techniques and obtained as 0.32 Tm and 0.34 Tm in Bi and Sn, respectively(4).

1.1.2 Heterogeneous nucleation

In practice, homogeneous nucleation is rarely encountered in solidification. Instead heterogeneous nucleation occurs at crevices in mould walls or at impurity particles suspended in the liquid. Consider a solid embryo forming in contact with a perfectly flat mould wall. Assuming σ_{SL} is isotropic it can be shown that for a given volume of solid, the total interfacial energy of the system is minimized if the embryo has the shape of a spherical cap with a wetting angle (Θ). When the interfacial tension balance is combined with the homogeneous nucleation equation, we can obtain

$$\Delta G_v = \Delta G_T \, f(\Theta) \qquad 1.6$$

$$\text{where} \quad f(\Theta) = \left[2 + \cos \Theta \right] \left[1 - \cos \Theta \right]^2 / 4 \qquad 1.7$$

It is significant that this factor $f(\Theta)$ is very small to even rather large values of the contact angle. Thus, when Θ is 10 degrees, the multiplying factor is of the order of about 10^{-4}. When Θ is 30 degrees, it is only about 0.02 and at 90 degrees, or at the limit of applicability of the above equation, it is still

only equal to one-half. This factor cannot affect the critical size, but does reduce the undercooling to 1-3 K (5).

1.2 Morphological instability of a solid/liquid interface

Kurz and Fisher discussed the morphological instability as given below(7). There are two kinds of the morphology of the interface between solid and liquid, faceted and non-faceted. When the latter exhibits the non-faceted growth morphology typical of a metal, it can be assumed that the kinetics of transfer of atoms from the liquid to the crystal are so rapid that they can be neglected since the kinetic undercooling is of the order of 0.002 K. When the solid exhibits the faceted mode of growth typical of non-metals or intermetallic compounds, a relatively large kinetic undercooling is required for the growth of the interface and was shown to be approximately 1 K (6).

Jackson et al. suggested that the melting entropy (ΔS_m). is a convenient criterion for predicting this aspect of the crystallisation behaviour. If values of α ($\alpha = \frac{\Delta S_m}{R}$) are less than 2, solid has a tendency to non-faceted crystal growth, while higher α-values exhibit faceted growth(6).

The conditions which lead to instability can be easily understood in the case of a pure substance. This is illustrated in figure 1. In a pure substance, stability depends on the direction of heat flow. In directional solidification, as in the columnar zone of a casting, the temperature always increases with distance ahead of the interface into the liquid. Therefore, the heat flow direction is opposite to that of solidification. When a perturbation of amplitude, ε, forms at an initially smooth

interface, the temperature gradient in the liquid increases while the gradient in the solid decreases. Since the heat flux is proportional to the gradient, more heat flows into the tip of the perturbation and less flows out of it into the solid. As a result, the perturbation melts back and the planar interface is stabilised. In equiaxed solidification, the opposite situation is found. The free crystals grow into an undercooled melt and the latent heat produced during growth also flows down the negative temperature gradient in the liquid. A perturbation which is formed on the sphere will make this gradient steeper and permit the tip to reject more heat. As a result, the local growth rate is increased and the interface is always morphologically unstable. This dendrite is known as a thermal dendrite(7).

In alloys, the criterion for stable/unstable behaviour is more complicated because the local equilibrium melting points can vary along the solid/liquid interface. During the solidification of an alloy, solute will pile up ahead of the interface due to the smaller solubility of the solid when the distribution coefficient is less than unity. Tiller at al(8) showed that this distribution of solute ahead of the interface under the steady-state condition can be given as

$$C_l = C_o + \left\{ 1 + \frac{1 - k_o}{k_o} \exp\left(- \frac{V}{D_l} z \right) \right\} \qquad 1.8$$

where C_o solute concentration in liquid at $z = \infty$

C_e solute concentration in liquid at $z = 0$

k_o partition coefficient between liquid and solid

V velocity of interface

D diffusivity of solute in liquid

z distance from interface

They assumed that there is no convection in the liquid and no diffusion in the solid. This solute boundary changes the liquidus temperature at the interface as shown in figure 2. When the actual temperature gradient in liquid is less than the temperature gradient of liquidus, the liquid is constitutionally undercooled and the planar interface becomes unstable. Under this condition, the dendritic growth occurs when

$$G_{(\ell)} < -\frac{\beta V C_s^* (1-k_o)}{D_l C_s k_o} \qquad 1.9$$

where C_s^* solute concentration in solid at interface

β slope of liquidus

The constitutional undercooling criterion does not say anything about the scale of the perturbation. The perturbation morphology is very important because this will influence the spacing of the resultant growth morphologies. The constitutional undercooling criterion also ignores the effect of the surface tension of the interface.

Mullins and Sekerka(9.10) recognised this point and developed a theory of instability of solid/liquid interface. They calculated the response of a planar solid interface to a shape perturbation. Solute is accumulated at the interface and the distribution is taken as $k_o < 1$. Equations are solved which

determine whether the shape perturbation decays or grows with time. In this development of the theory, convection was neglected. The theory predicts stability at the low growth rates, such as single crystal growth and at the high cooling rates such as laser surface melting. Between these two extreme cases, the unstable interface will be obtained(7).

Recently the planar to cellular interface transition during the directional solidification of a binary alloy was studied in the succinonitrile-acetone system by Eshelman and Trivedi(11). They found that the critical velocity of the interface agrees with that predicted by the linear stability analysis of Mullins and Sekerka.

1.3 Dendrite growth

The dendritic growth can be divided into two categories(7).

a) Constrained growth

b) Unconstrained growth

The situation in which the heat flow is opposite to the growth direction, i.e. columnar solidification, is often referred to as constrained growth. That is, the rate of advance of the isotherms constrains the dendrites to grow at a given velocity. This forces them to adopt the corresponding tip undercooling. When the heat flows from the crystal into the melt, i.e. equiaxed solidification, the dendrites can grow freely as rapidly as the imposed undercooling permits. It is known as unconstrained growth.

1.3.1 Unconstrained growth

Several mathematical analyses have been developed for dendrite growth.

Ivantsov(12) gave a mathematical analysis of the relation of growth rate to undercooling. The solid in growth has a temperature slightly in excess of the melt, and the latent heat of the solid phase is transferred to the melt at the interface, allowing the solid to grow. The solid achieves a limiting rate, which has a constant value if the supercooling is constant. Ivantsov derived exact solution for the growth of crystals of specific shapes. These analyses were for one-component systems, for a constant interface temperature. For a paraboloid of revolution, Ivantsov's solution was

$$\Delta\phi = P \exp(P)\, E_i(P) \qquad 1.10$$

$$P = \frac{V r}{2 \alpha}$$

where $V r$ = constant for small P number

Ei the exponential integral function,

V the velocity.

P the Peclet number

r tip radius.

α thermal (mass) diffusivity

$\Delta\phi$ dimensionless undercooling $= \frac{(T_e - T_\infty) C_p}{L}$

Ivantsov(12) and Horvay and Cahn(13) gave exact steady-state

solutions for the growth of parabolic cylinder and a paraboloid of revolution. In these solutions, it was assumed that the composition of the matrix in contact with solid was constant. However, Zener(14), Hillert(15) and Horvay and Cahn(13) pointed out the non-isoconcentrate nature of the interface. This is due to the presence of a large interface curvature and an interface kinetic effect.

Recently, Huang and Glicksman(16) presented an extensive review of dendritic growth, providing a critical evaluation of the different theories. They described the dendritic growth mode as the most common mode of solidification, in particular for metals and systems that freeze with low entropy of fusion. They considered dendritic growth as proceeding by two seemingly independent growth processes:

a) steady-state propagation of the dendrite stem

b) non-steady-state evolution of dendrite branches

They stressed the importance of understanding the time-dependent features of dendritic growth. The stem studies of dendrites gave a mathematical description of a branchless geometrical form growing at a constant rate in a shape-preserving manner. The growth was confined to the steady-state development of an one-component geometrical form growing in a melt mainly by heat conduction. The results of the theories express the axial dendritic growth velocity as a function of undercooling ΔT ($= T_m - T_\infty$) where T_m is the melting point and T_∞ is melt temperature far from the interface.

$$V_{max} = \beta G^* (\Delta T)^b \qquad 1.11$$

where σ^* lumped material parameter

β a numerical coefficient

b an exponent.

β and b are determined by each theoretical model and are specific to it.

Glicksman and Schaeffer(17) had previously made experiments to test this equation and had measured dendritic growth velocity of succinonitrile over a range of supercoolings from 1 to 10 K. The experiments were designed to test the diffusion-controlled steady-state dendritic growth theory related to the equation 1.11. The results of Glicksman's experiments revealed that although two of the theories predicted a correct power-law relationship $V \propto \Delta T^{2.65}$, none of the theories predicted the correct growth velocity, i.e. the coefficient β in equation 1.11 to within twice that of the measured value.

Nash and Glicksman(18) discussed the theoretical analyses of dendritic growth in terms of the Peclet number P. The Peclet number relates the velocity of growth V to the tip radius r, i.e. $p=V\, r/2\alpha$, where α is the coefficient of thermal (or mass) diffusion. The results of the theories have the following form :

$$\Delta\phi = P \exp(P)\, E_i(P) + \Delta\phi_c \qquad 1.12$$

In this expression, $\Delta\phi$ represents dimensionless supercooling and is equal to $\frac{\Delta T c}{L}$, c is specific heat and L is the heat of fusion. Other terms are as previously described. $\Delta\phi_c$ is a term

reflecting the influence of capillarity(Gibbs-Thomson effect) and is hence a function of tip radius and also related to velocity. Equation 1.12 reflects two physical effects:

1. The point effect (V r = constant) . This part is solution to the thermal diffusion model with an isothermal interface. In this, $\sigma = 0$ and $\Delta\phi_c = 0$.

2. For the case where $\sigma \neq 0$ the Gibbs-Thomson effect lowers the interface equilibrium by Tm/L. This effectively reduces the supercooling for thermal diffusion.

As the radius of the tip becomes smaller, the reduction in supercooling becomes bigger. This mechanism effectively prevents dendritic growth velocity from growing increasingly fast as $r \longrightarrow 0$. It was pointed out that this is the physical meaning of the point effect. Then the equation 1.12 represents a limitation of V by capillarity and provides an upper bound value of Vmax for given $\Delta\phi$. Huang and Glicksman related this to the absence of unique relations for V versus $\Delta\phi$ and r versus $\Delta\phi$, so that these are absent in these models. A unique relationship had been expressed by assuming that dendrites grow at the maximum possible velocity allowed by the capillarity effect(Vmax.). Glicksman's results, however, disagreed with a Vmax versus ΔT relationship as in equation 1.11.

Nash and Glicksman suggested that the maximum growth velocity hypothesis might be at fault. They measured the tip radius and corresponding growth velocity of a dendrite at a given supercooling. They expected that the measured point (V and r) would fall on the line described by equation 1.10 but not at the point of Vmax.

Figure 3 shows their test results. The graph plots V and r at $\Delta T=1.2$ K for the theories of Ivantsov(12), a modified Ivantsov equation(18), and a theory due to Temkin(19). An experimental point obtained from their measurements is plotted on the curve.

Current theories outlined by Nash and Glicksman are based on the stability of a steady-state dendrite tip. Oldfield(20) had previously recognized the need for a dendrite tip to achieve a stable condition in steady-state growth.

The condition of marginal stability for a pure material growing its supercooled melt may be shown to be

$$R_e(\sigma) = 0 = -\Gamma w^{*2} - \bar{G} \qquad 1.13$$

where G is the average thermal conductivity and w^* is the wavenumber of the marginal perturbation. Langer and Muller-Krumbhaar(21) suggested the wavelength $\lambda^*=2\pi w^*$ of the marginal perturbation. The average temperature gradient at the dendrite tips is

$$\bar{G} = -\frac{P}{r}\frac{L}{c} = -\frac{V}{2}\frac{L}{\alpha c} \qquad 1.14$$

Then we can find that the marginally stable state $R_e(\sigma)=0$ occurs when $r = \lambda^*$, which after some rearrangement yields the condition for growth :

$$V r^2 = \frac{8\pi^2}{L}\alpha c \Gamma \qquad 1.15$$

The marginal stability criterion ($V r^2$ = constant) can then be

used to separate V and r predicted by the steady-state models. Figure 3 shows the measured point falling on the plot of V and r with $\sigma^* = 1.95 \quad 10^{-2}$.

Recently, Lipton, Glicksman and Kurz(22,23) developed a relationship considering both the diffusion field for a parabolic tip and the stability criterion for binary alloys. This relationship indicated that the dendrite tip radius passes through a minimum with increasing solute concentration and at a given undercooling the growth velocity should increase with increasing solute concentration and then decreases as higher solute levels are reached. These findings are shown to correspond to experimental results obtained using succinonitrile-acetone solutions(24).

1.3.2 Constrained growth

Tewari discussed the several current primary arm spacing theories as given below. These theories have been proposed to explain the solidification behaviour of binary alloy melts in positive temperature gradients. The aim of these models is to predict the radius of curvature, temperature, and liquid composition at the cell or dendrite tip and for some models, the primary arm spacing as a function of the variables: alloy composition, imposed thermal gradient at the liquid-solid interface and alloy growth velocity. These models can be classified into three groups. The first, consisting of models due to Bower, Brody and Flemings(25), Burden and Hunt(26) and Laxmanan(27), consider steady-state behaviour of a dendrite array and assume that the dendrite grows with minimum tip undercooling,

i.e., maximum temperature at the tips. The second group, consisting of the Trivedi(28,29,30), Kurz and Fisher(31) and Laxmanan(32,33) models, assume that marginal stability concepts determine the dendrite tip characteristics at the operating point of the dendrite. The third group, the models of Jin and Purdy(34) and Kirkaldy(35), assume that the observed cell shape minimizes the rate of entropy production for the liquid to solid transformation.

The first significant treatment was presented by Hunt. His model was based on three major assumptions:

1) a dendritic interface with sidearms is approximated as a smooth steady-state interface and

2) a constant temperature and a constant liquid composition in the direction normal to the primary dendrite growth direction

3) there is no diffusion of solute into the solid

Under these assumptions, Hunt derived the shape of the cell by following the procedure developed earlier by Bower, Brody and Flemings. Since the second assumption of the Hunt model is valid only for the dendrite or cell region which is far behind the tip, the interface shape is not valid near the tip region. Hunt circumvented this problem by fitting part of a sphere to the derived at the growing front. Under these assumptions, he obtained the following relationships at the high velocities,

$$\lambda_1 = \lambda_{Hunt} = \left(\frac{-4\, 2^{1/2}\, r_t\, \beta\, C_o\, (k_o - 1)}{G} \right)^{1/2} \qquad 1.16$$

$$r_t = \left(\frac{2\,\Gamma\,D_l}{\beta\,V\,C_o\,(k_o-1)}\right)^{1/2} \qquad 1.17$$

where λ_1 primary arm spacing

β slope of the liquidus line

C_o alloy concentration

k_o equilibrium solute partition coefficient

G thermal gradient at the dendrite tip

r_t dendrite tip radius

Γ Gibbs-Thomson coefficient

D_l solute diffusivity in liquid

V growth velocity

ΔT solidification range

Tip undercooling measurements showed a good agreement with the model(36). However, it has been criticized for not predicting the proper dependence of the radius of the curvature on temperature gradient in liquid(28,32). It also fails to predict the proper undercooling at the absolute stability limit of Mullins and Sekerka(32,10). Laxmanan(27) has recently proposed a further model, which while incorporating the minimum tip undercooling assumption, predicts the radius of the curvature dependence on the temperature gradient in liquid and satisfactorily explains the limiting behaviour, both in the small growth velocity regime (Chalmers constitutional stability limit (37)) and at the rapid growth rates (absolute stability limit (10)). His equation can be expressed at the high velocities as,

$$\lambda_{L(M)} = \lambda_{Hunt} \qquad 1.18$$

where
$$r_t = \left(-\frac{2}{\lambda}\frac{l_c}{V}\frac{D_l}{(1-S)}\right)^{1/2} \qquad 1.19$$

$$l_c = -\frac{\Gamma}{k_o \Delta T_o} \qquad S = -\frac{D_l}{V}\frac{G}{\Delta T_o}$$

Another theoretical model to characterize primary dendrite arm spacing was developed by Kurz and Fisher(31). They assumed that the shape of cell or dendrite can be approximated as ellipsoids so that

$$r_t = \frac{b^2}{a} = \frac{\lambda_1^2}{3}\frac{G}{\Delta T_o} \qquad 1.20$$

and they obtained the tip radius from the marginal stability criterion for an isolated dendrite or cell. The equation at the high velocities becomes(figure 4)

$$\lambda_1 = 4.3\left(\frac{\Delta T_o D_l \Gamma}{k_o}\right)^{1/2} V^{-1/4} G^{-1/2} \qquad 1.21$$

In another approach, Laxmanan(32,33) has examined the dendrite growth problem by incorporating the stability requirements obtained by Trivedi into the solute transport equations and predicted the corresponding radius of curvature, the temperature

and the concentration of solute at the tip. The equation at high velocities is

$$\lambda_{L(MS)} = \lambda_{Hunt} \qquad 1.22$$

$$r_t = \frac{l_c L \lambda (1-k_o)}{(1-S)} \left[\left\{ 1 + \frac{l_s (1-S)}{l_c L \lambda^2 (1-k_o)} \right\}^{1/2} - 1 \right] \qquad 1.23$$

$$l_s = \frac{2D}{V} \qquad \lambda = 1/16 \qquad L = 28$$

The Trivedi(28,29,30) model based on the marginal stability concepts has been shown to predict accurately the observed growth rate dependence of the radius of curvature at the tip in the succinonitrile-acetone model system(figure 5). Trivedi has incorporated Hunt's approach in his model to predict the primary arm spacing. His equation are

$$\frac{\lambda_1 G}{r_t k_o \Delta T_o} = \frac{4 \, 2^{1/2} A L}{P^2} \qquad 1.24$$

$$A = \frac{l_c}{l_s} = \frac{\Gamma V}{2 D_l k_o \Delta T_o} \qquad 1.25$$

$$(1/2) \xi [1 - F_1(P)] + \left[\frac{A L}{P^2} \right] [1 - F_2(p)] = [1 - \phi (1-k_o)]^{-1} \qquad 1.26$$

$$\xi = \frac{2 D G}{V k_o \Delta T_o} \qquad 1.27$$

$$F1(P) = \left\{ \phi\,(1-ko)/\,[1-\phi(1-ko)] \right\} \left\{ [1-\phi]/(\phi-P+P\phi) \;-\; (1/\phi) \right\} \quad 1.28$$

$$F2(P) = (2/L) \left\{ \phi\,(1-ko)/[1-\phi(1-ko)] \right\} \left[1 + P - (P/\phi) \right] \quad 1.29$$

$$\phi = P\, exp(P)\, E_i(P) \quad 1.30$$

It can be easy to calculate V for a given value of P and then we use the relationship $r_t = \frac{2PD}{V}$ to obtain the tip radius value. Note that 1.26 is quadratic for V so that for each value of P, two sets of v and r_t values are obtained. One set of values corresponds to the dendritic region whereas the other set of values corresponds to the cellular region.

Trivedi and his colleagues(38,39,40) have directionally solidified several metallic alloys to examine the dependence of λ_1 on V and G. It has been shown that the primary arm spacings observed in Pb-Au, Pb-Pd and Pb-Sn alloys qualitatively follow the trend predicted by the Trivedi model, especially under dendritic growth conditions. However, the primary arm spacing deviates significantly, as the growth conditions approach the cellular growth regime. McCartney and Hunt(41) observed similar behaviour in Al-Cu alloys and suggested that convection present in the liquid is responsible for this decrease in arm spacing.

The major difference between the Hunt and Kurz-Fisher theories is in the constants. The final expressions derived differ by $1.52\sqrt{ko}$. On the other hand, the difference between the Hunt

and Laxmanan theories(for minimum undercooling) is

$$\frac{\lambda_{Hunt}}{\lambda_{L(M)}} = \left\{ \frac{k_o (\Delta T_o V - D_l G)}{16 V \Delta T_o} \right\}^{1/4} \qquad 1.31$$

1.4 Measurements of primary arm spacing

In the past 10 to 20 years, many experimental works to measure the primary spacings of many alloy systems have been carried out. In the literature, these data are generally presented in two ways. In the fist, the temperature gradient in liquid and the growth rate can be independently varied; the results are presented in the form :

$$\lambda_1 = b\, G^{-n}\, V^{-m} \qquad 1.32$$

In the second, both of the variables can be combined into the form :

$$\lambda_1 = b (G V)^{-n} = b (W)^{-n} \qquad 1.33$$

where n,m,b are constants

The unidirectional solidification technique has been developed to control these variables independently. These experimental results are reviewed.

Klaren, Verhoeven and Trivedi(39) investigated the primary

arm spacing in Pb-Sn, Pb-Pd and Pb-Au systems as a function of temperature gradient, solidification rate and composition. Variation of temperature gradient was carried out at a moderate growth rate, 0.6 mm/min and variation of growth rate was carried out at high gradients, around 35 deg C/mm. Based on these experiments, the primary dendrite arm spacings are found to follow this correlation

$$\lambda_1 \alpha G_\ell^{-1/3} V^{-1/2} \qquad 1.34$$

They also found that the primary arm spacing increases slightly with the solute content.

Young and Kirkwood(42) investigated the morphology of Al-Cu alloys ranging from 2 to 10 % Cu in the unidirectionally solidified specimens. They found the primary arm spacing can be described in the form of

$$\lambda_1 \alpha G_\ell^a V^b \qquad 1.35$$

where both a and b are close to - 1/2.

It is also found that the primary arm spacing increases slightly with solute content.

Hunt(36) checked his model with Young and Kirkwood results. He found that when the experimental results are plotted against $G_\ell^{1/2} V^{1/4}$, the reasonable agreement can be shown with his model.

Other work on dendrite spacings was examined by Suzuki et al(43). Using vertical semi-steady state solidification, they suggested that the primary arm spacing of two steels Fe-25 % Cr-

20 % Ni and Fe-1 % Cr-0.25 % Mo gave a relationship of

$$\lambda_1 \alpha G_\ell^{-0.40} V^{-0.20} \quad 1.36$$

in good agreement with the Hunt model exponents

In other published work on Fe-1.4 % Cr-1 % C, Rickinson(44) showed good agreement with Young and Kirkwood by plotting the primary arm spacing against the cooling rate in the liquid, $(G_\ell V)^{-1/2}$ and if variables are separated, the results indicated a relationship of

$$\lambda_1 \alpha G_\ell^{-0.70} V^{-0.50} \quad 1.37$$

McCartney and Hunt(41) agree with earlier findings(45) that gravitational convection in a specimen cannot be eliminated by growing dendrites upwards in a system in which the solute rejected causes the liquid to become denser. By balancing the rejected solutes in the ternary Al-Mg-Si system, they developed a series of alloys that exhibited no density change with composition along the liquidus, and thus eliminated any gravitational convection. They measured the primary arm spacing by counting the number of tips in an area at the interface. The results show a very close agreement with exponents of the general form of models.

$$\lambda_1 \alpha G_\ell^{-0.55} V^{-0.28} \quad 1.38$$

Jacobi and Schwerdtfeger(46) investigated two high carbon

manganese steels. They calculated average primary arm spacing from the number of arms present in the observed area using the model of a hexagonal arrangement. They found this method more objective and reproducible than the line counting method. They also defined several primary arm spacings due to the close packed arrangment. Their results based on G(s+l) are

$$\lambda_1 \alpha G_{(s+\ell)}^{-0.72} V^{-0.25} \qquad 1.39$$

When these data were recalculated due to G in liquid, the results show very good agreement with the exponents of the models.

$$\lambda_1 \alpha G_{\ell}^{-0.56} V^{-0.25} \qquad 1.40$$

In their latter paper, they and their colleagues(47) investigated the morphology of five highly alloyed steels, ferritic and austenitic, by using the unidirectional technique. They found that the dendrite arm spacings can be correlated by the equation

$$\lambda_1 \alpha G_{\ell}^{-0.50} V^{-0.25} \qquad 1.41$$

The exponents m and n are fairly close to the theoretical values. However, when they compared their results with the Hunt and Kurz-Fisher models, it was shown that K-F overestimates the actual values seriously, whereas Hunt underestimates them.

Edvardsson, Fredriksson and Svensson(48) studied the morphology

of four low carbon manganese steels in large cooling range. They found

$$\lambda_1 \alpha (G V)^n \qquad 1.42$$

n is between -0.30 and -0.20

They also reported that the primary arm spacing decreases with increasing carbon content.

Botas(49) investigated the solidification structures of Cu-Sn, Cu-Co and Cu-Mn alloys. He found that the results generally are in good agreement with $G_L^{-1/2} V^{-1/4}$ relationship form.

Recently, Somboonsuk, Mason and Trivedi(30) carried out the directional solidification experiments in a succinonitrile- 5.5 mol pct acetone system in order to characterize dendrite spacings as a function of growth rate and temperature gradient in liquid. They found that the results of the primary arm spacings fall between the Kurz-Fisher and Hunt models as other investigators observed. But they showed that Trivedi model which is based on the marginal stability criterion can predict more closely the actual data.

Tewari(50) checked the current models in Pb-8 % Au and Pb-3 % Pd alloy systems by using the directional solidification technique. He calculated the dendrite tip radius and solute concentration at the tip and the primary arm spacing. It is found that the Hunt model, based on the minimum undercooling approach, does not predict the observed behaviour. However, a modification of this model recently proposed by Laxmanan shows a good fit to the

experimentally observed parameters. The models based on the marginal stability approach also predict most of the observed behaviour well (figure 6).

1.5 Development of side arms

The constitutional undercooling was introduced by Tiller et al(8). Using this concept, it is also possible to explain the formation of the side arms. If the conditions for constitutional undercooling ahead of an interface are considered to apply to the side of the dendrite behind the tip, then it can be seen that any solute built up between the dendrites will produce undercooling in liquid. The solid-liquid interface becomes unstable. This causes the formation of side arms.

Later, Sekerka and Mullins(9.10) suggested that the morphological instabilities are intrinsically kinetic rather than thermodynamic in nature. Langer and Muller-Krumbhaar(21) used this marginal stability condition instead of the maximum growth velocity principle to select the steady-state of a dendrite tip. Under this condition, the tip is the only point on a needle dendrite which is stable. Instability would still persist at all other portions of the dendrite surface and lead ultimately to side arm formation. The first ten arms show a nearly constant spacing. This is a characteristic of wave-controlled mechanisms. But the initial side arm spacing was found to be about three times the wavelength of the critical perturbation wave(16).

Huang and Glicksman(16) carried out the experiments to study the development of the side arm structure in succinonitrile. They suggested, based on their laboratory observations, that the

slight anisotropy in solid-liquid interfacial energy plays an important role in the side arm mechanism. Anisotropy in solid-liquid interfacial energy provides an additional source for interfacial distortion other than the interfacial instabilities associated with paraboidal dendrites. In the early stage of side perturbation, the slight, cubically symmetric anisotropy in solid-liquid interfacial energy seems to be the dominating force. Thereby, four branching sheets in 100 planes are always formed. It is only in later stages that the dendritic instabilities take over and periodic bumps evolve into branches along the branching sheets.

These perturbations grow, become cell-like, sometimes eliminated by their neighbours. A number of them finally become real secondary dendrites growing perpendicularly to the primary trunk (in the case of a cubic crystal). These secondary arms, with their higher-order branches, grow and eliminate each other as long as their length is less than $\lambda/2$. Once the diffusion fields of their tips come into contact with those of the branches growing from the neighbouring dendrites, they stop growing. A ripening process causes the highly-branched arms to change with time into coarser, less branched and more widely-spaced ones(7).

1.6 Measurements of secondary arm spacing

The secondary arm spacing plays a significant role in the solidification of metals, together with primary arm spacing because it determines the spacing of microsegregation, precipitates or microporosity. Thus, it has a considerable effect

on the mechanical properties of solidified alloys(51).

In the earliest investigation, Horwath and Mondolfo(52) studied the secondary arms in Al-Cu alloys. They reported that the secondary dendrite arm spacings λ decrease with increasing cooling rate and solute content.

Bower, Brody and Flemings(26) investigated the secondary arm spacing in Al-Cu alloys in the solidified ingots under known thermal conditions and by unidirectional solidification. They compared these measurements with several previous studies. All the points fitted this empirical equation

$$\lambda_2 = 7.5 \left(\theta_f \right)^{0.39} \qquad 1.43$$

Later, Kattamis et al(53) showed that the results from the isothermal and interrupted solidification experiments could be represented by the same line.

This power law expression of the secondary dendrite arm with solidification time has been shown to be true for all systems, but there was a disagreement about exponent of the equation as well as pre-exponent constants.

In parallel with the study of secondary arm spacings in casting, similar studies were being undertaken in unidirectionally partly solidified specimens, cooled under steady-state conditions.

Young and Kirkwood(42) investigated in detail secondary arm spacings in Al-Cu alloys, ranging from 2 to 10 % Cu, in the unidirectionally partly solidified specimens under low and high

cooling rates. They found that the exponent value is 0.32. They reported also that the effect of increasing the solute content is to reduce the spacing at any point behind the tip and increasing the growth velocity of the tips produces finer spacings for the same value of local solidification time. Recently, the results of Mortensen at al.(59) on Al-4.5 % Cu alloy showed a good agreement with Young an Kirkwood results.

Jacobi and Schwerdtfeger(46) studied the morphology of two manganese steels at 0.6 and 1.5 % C by using steady-state unidirectional solidification technique. They found that the exponents of coarsenings of these alloys were 0.44 and 0.50 but they did not quench these specimens during growth. Their results were based on the final arm spacing as a function of solidification time. Suzuki(54) reported the coarsening exponent as n=0.40 for commercial low alloy steels(figure 7). Fe-Cr-C alloys studied by Okamoto et al(55) showed a cubic root dependence of the solidification time but, over a small range. Rickinson(56) found that the secondary arms coarsen linearly with solidification time. He also reported that the increase in Cr content reduces the secondary arm spacing.

Taha et al.(47) investigated the dendrite morphology of five steady-state unidirectionally solidified steels. Their compositions were in the range of 0.57 to 27 % Mn , 0 to 27 % Ni, 0 to 12 Co and 0 to 28 % Cr. The coarsening exponents generally changed between 0.44 to .40 for all specimens. They agree with Rickinson that the secondary arm spacing decreases at the fixed carbon content with increasing solute contents. Ogilvy(57) showed that this exponent in the tool steels is 0.23 under controlled

solidification condition for large cooling rate range.

1.7 Dendrite arm coarsening

Dendrite arm coarsening models may be classified into two regions, ripening and coalescence, but the driving force in both processes is the reduction of the total surface energy of the system (figure 8).

The ripening models are also classified into three groups as shown in figure 8 . The first of these has been considered by Kattemis et al(51), the second by Chernov, Klia and Kattamis et al(51) and the third by Kahlweit(51). In the first model, the radius of dendrite arms is considered to be constant(radius= a) except for one arm which is r , where $r < a$. Therefore the melting point of the smaller arm is less than that of the remaining arms, the liquid concentration is vice versa; due to the Gibbs-Thomson effect so that the solute diffuses to the smaller arm causing dissolution by reducing its radius. Consequently, the total dendrite arm spacing increases(53). This can be expressed as :

$$t_{crit} = \frac{\Delta H\, C_l\, (1-k_o)\, \beta\, \lambda_2}{D_l\, T}\, a^2 \ln\left(1 - \frac{r_o}{a}\right) + a\, r_o \qquad 1.44$$

In the second model(53), a dendrite arm is considered whose root is slightly smaller than its remainder; this arm tends to melt off by transport of liquid from the necked region. This mechanism can be important when there is a thermal fluctuation

in the cast (figure 8).

In the third model(58), a single dendrite arm of radius a is considered. This dendrite dissolves from its tip to root. Kahlweit presented this model with the equation below

$$t_{crit} = \frac{C_l (1-k_o) \Delta H \beta}{D_l \sigma T} \frac{r^2}{4} \frac{1}{} \qquad 1.45$$

Young and Kirkwood(42) observed the secondary arm coarsening in Al-Cu alloys with coalescence mechanism. Then they proposed a different model as shown in figure 9. They considered that the actual dendrite geometry could promote coarsening. As the root of a dendrite has a negative curvature there will be solute enhancement in the adjacent liquid while there will be solute depletion by the sides of the dendrite where the curvature is positive. Diffusion of solute takes place leading to deposition of solid at the root while the tip shrinks back due to solvent diffusing away. It was further pointed out that a shorter path for diffusion existed if the slight curvature of the dendrite side was considered. Diffusion can take place from the roots and tip to the sides for the solute and solvent respectively causing the head of the dendrite to swell. As the heads of the dendrite swell they touch so that coalescence occurs leaving a small liquid region at the roots apparently isolated from the main liquid which rapidly sphereoidizes. The main attraction of this model is that it occurs as necessary consequence of the dendrite morphology (figure 9). They applied Kahlweit model to the

coalescence model as

$$t_{crit} = \frac{C_l (1 - k_o) \Delta H \beta}{D_l \sigma T} \frac{1^2}{2} \left(\frac{1}{r_A} - \frac{1}{r_B} \right)^{-1} \quad 1.46$$

Recently, Mortensen et al(59) suggested that the ripening is predominant coarsening mechanism at low volume fractions of solid whereas coalescence becomes predominant at high volume fraction of solid. They proposed a different equation for coalescence. They considered that the coalescence is limited by solute diffusion from the region of maximum positive curvature at the dendrite tips to that of maximum negative curvature, at the bottom of the trough. It is assumed that the coalescence process is slow enough for the solute concentration profile to obtain the steady-state diffusion condition so that

$$\frac{\partial (R_B J)}{\partial t} = 0 \quad 1.47$$

and the equation can be expressed as :

$$t_{crit} = \frac{C_o \beta}{\omega} \left\{ \left(\frac{0.1 \lambda_2 R_B^2}{D_l \Gamma} + \frac{1}{1 + f_{sl}} \right)^{1-k_o} - 1 \right\} \quad 1.48$$

It is also assumed that λ_2 is constant. In this equation, the volume fraction of solid f_{sl} where coalescence begins should be defined.

All these models are derived for isothermal coarsening.

However, Kirkwood(60) and Feurer and Wunderlin(61) developed two different secondary arm coarsening models during solidification by employing the Kahlweit model and the Kattamis, radial melting, model, respectively, for constant cooling rate. λ_2 in both models is proportional to $t^{1/3}$. The only difference lies in the constant. Kirkwood checked his equation with available data in the literature for Al-Cu alloys. He found very good agreement over a wide range of solidification rate as shown in figure 10.

1.8 Secondary arm migration under temperature gradient

Migration process under temperature gradient has been well known in the fields of single crystal manufacture, nuclear fuel element degredation and interface kinetics studies. The migration process of a liquid droplet in a solid alloy was for the first time discussed in more general terms by Pfann(62) as temperature gradient zone melting (TGZM). The mechanism is shown in figure 11. When we consider a liquid droplet inside a solid specimen under a temperature gradient, we can expect that the opposite ends of the droplet have different temperatures and therefore have different compositions. Hence, there is a concentration gradient across the droplet and solute diffuses from cold to hot. This causes solidification at the cold end and melting at the hot end, so that the droplet migrates up the temperature gradient.

A vapour or gas bubble in a solid placed under a temperature gradient will also be expected to move towards the hot end of the solid sample, because the vapour pressure increases as temperature increases resulting in a concentration gradient in the bubbles.

Similarly a solid inclusion, where solubility in the solid matrix increases with temperature, should in a temperature gradient migrate up the gradient in response to the concentration gradient produced by the temperature variation(63).

Recently, Allen and Hunt(64,65) investigated the possible occurence of TGZM during dendritic solidification in organic transparent materials. By using a photographic technique, they observed that individual dendrite arms migrate towards the tip during solidification and it is suggested that it could be as much as four arm spacings. This was also explained by TGZM, considering the interdendritic liquid pool between secondary arms as a liquid droplet in a solid. Under temperature gradient, the remelting of the secondary arm on the hotter side of the liquid pool and the solidification at the colder side of the liquid pool occur simultaneously (figure 12). Allen and Hunt analysed the kinetics of this situation and showed that if the interdendritic pool width, L ,exceeds a value of $2D_l/V$, where D_l is the solute diffusivity in liquid and V is the growth rate of the primary tips, then the pool will solidify normally. If $L \ll 2D_l/V$, then TGZM becomes dominant and produces asymmetric distribution of solute profile across secondary arms called a saw tooth profile. Under TGZM effect, the velocity of a migration dendrite(V) is given by

$$V = \frac{D_l G}{\beta C_l (1-k_o)} \qquad 1.49$$

and the total migration distance(d) during solidification is

$$d \cong -\frac{D_l}{V(1-k_o)} \ln\left(\frac{C_2}{C_1}\right) \qquad 1.50$$

where C_2 concentration of liquid at the end of solidification

C_1 concentration of liquid at the start of solidification

This effect was used to explain the discrepancy of minimum concentration between the prediction of segregation models and the experimental results in Bi-Sn system(66,67).

It can be concluded that TGZM, solute back diffusion, dendrite arm coarsening and a high degree of undercooling at the dendrite tips have all been invoked to reduce the microsegregation during solidification.

CHAPTER 2 MICROSEGREGATION

2.1 Determination of microsegregation

Microsegregation can be expressed by different indices as given below

a) Segregation ratio :

$$S = \frac{Cmax}{Cmin} \qquad 2.1$$

Where Cmax maximum solute concentration

Cmin minimum solute concentration

This is most commonly used in the literature and also in the present study.

b) Effective partition ratio :

$$ke = \frac{Cmin}{Co} \qquad 2.2$$

Where Co average concentration

This is used to express the increase in the minimum concentration where Cmax is difficult to determine, for instance in Al-Cu alloys.

c) The quantity of non-equilibrium second phase.

For example, the amount of non-equilibrium eutectic phases in Al alloys is very often used to define the microsegregation and is still referred to in the literature. This value is represented as a volume fraction(68).

d) Segregation parameter

The segregation parameter is defined as the area between the average concentration line and the actual solute profile, when the cumulative solute concentration is plotted against the

fraction of solid(44,69,58).

2.1.1 Methods of determination of microsegregation

Different techniques can be used to determine the microsegregation in alloys. In the early years, microradiography(70,71), hardness(72) and metallographic techniques were employed to investigate inhomogeneity in alloys. However, these methods give qualitative results rather than quantitative.

Later, electron probe microanalysis was used to obtain more accurate data on the solute concentration in alloys and this generated renewed interest and debate in the field of microsegregation. Most recently, the concentration map of segregation pattern has become available with advancing technology, so that segregation can be related more easily to the geometry of dendritic structure.

2.2 Distribution coefficients

The equilibrium distribution coefficient ko is given by the ratio of solute in solid(Cs) to solute in liquid(Cl), as defined by the liquidus and solidus lines over the solidification interval of a binary phase diagram. If these lines are assumed to be straight for the ideal case, then the equilibrium distribution coefficient can be taken as a constant during solidification

$$ko = \frac{Cs}{Cl} \qquad 2.3$$

The solid/liquid interface rejects solute into the liquid, if the solubility of the solute element in the solid is smaller than in the liquid. In this case, the liquidus slope, β, is negative and the distribution coefficient is smaller than unity. On the other hand, β is positive and ko is greater than unity when the solubility is greater in the solid than in the liquid. In this case, solute will diffuse from the liquid to the solid.

This equilibrium distribution defines a local equilibrium condition which can be maintained under normal cooling rate or growth rate. It is a useful approximation in many cases of casting solidification and has been used extensively by Flemings and his co-workers(26,73,74) to model the solute redistribution during solidification both analytically and numerically. For a rapidly advancing interface it becomes unrealistic. The distribution of solute between solid and bulk liquid is influenced by the diffusion of solute in the liquid, diffusion in the solid and convection. Under these circumstances, it is convenient to define an effective distribution coefficient (ke).

$$ke = \frac{Cs}{C\infty} \qquad 2.4$$

where Cs is the solute content in the solid at the interface and C∞ is the solute concentration in liquid far from the interface. Burton et al(75) considered that there was complete mixing in the liquid behind the interface and this planar interface advances at velocity V into the liquid. Under these circumstances, they related ke to ko with this equation

$$k_e = \frac{k_o}{k_o + (1-k_o)\exp\left(-\frac{V\,\delta}{D_l}\right)} \qquad 2.5$$

where V growth rate of planar interface

δ diffusion boundary layer

Dl solute diffusivity in liquid

For slow growth rates, ke tends to ko and the situation of complete mixing is achieved. If no mixing occurs in the liquid, the solute concentration in the boundary layer reaches Co/ko and ke=1. Generally however, partial mixing occurs in the liquid ahead of the solid /liquid interface, and then ke becomes a function of hydrodynamic conditions in the melt.

Bolling and Tiller(76) replaced the planar interface assumption with the parabolic dendrite tip interface. Then ke becomes

$$k_e = \frac{k_o}{1 + (1-k_o)\alpha_b \exp(\alpha_b) E_i(-\alpha_b)} \qquad 2.6$$

where

$$\alpha_b = \frac{V\,E_t}{2\,D_l} \quad \text{and} \quad E_i(-\alpha_b) = -\int_{\alpha_b}^{\infty} \frac{\exp(-t)}{t}\,dt$$

These models can predict the solute builds-up in front of the interface in the liquid. Kohn and Philibert(77) observed this

boundary in Al-Cu castings by crossing the solid/liquid interface into the liquid with electron probe microanalysis. This result indicated that solute undercooling must have been present during growth and the measured ke was found to be greater than ko. Doherty and Melford(78) reported the similar result in Fe-Cr-C alloys. However, Subramanian, Haworth and Kirkwood(79) disagreed with these results and suggested that the enhanced solute at the interface was caused by very rapid solute rejection on quenching. By ignoring the interfacial liquid, they calculated ke as approximately equal to ko

2.2.1 Determination of equilibrium distribution coefficient

The equilibrium distribution coefficient can be determined mainly by four methods.

a) Thermodynamic

If the solid-liquid interface is thermodynamically at equilibrium, then the chemical potential of the solute elements in both phases should be equal to each other, so that ko becomes

$$ko = \frac{Xs}{Xl} = \exp\left\{ (\mu_x^l - \mu_x^s)/R\,T \right\} \exp\left[\ln \gamma_x^l - \ln \gamma_x^s \right] \quad 2.7$$

where μ_x^i chemical potential of i phase in standard state

R gas constant

T temperature

γ_x^i activity coefficient of i phase

Xi mol fraction of i phase

This should be converted to weight percentage as used in practice. In the multicomponent alloys, the interaction cofficients are required in the calculation. Recently, several workers have employed this method in the iron alloys in order to check the experimental results(80-86).

b) Phase diagram

ko can be easily obtained from phase diagrams if the solid and liquid lines are known as a function of temperature. This method is usually used for binary alloy when there is no direct experimental data in the literature. The effect of third element on it can be simply checked by thermal analysis, but this method can not give true solidus temperature because of microsegregation.

c) Microanalysis of directionally solidified specimens

In this method the specimen is solidified under steady-state condition and quenched rapidly during growth, so that the interface allows us to measure the solid and the liquid concentration. However, this technique needs very slow cooling rate or growth rate to maintain planar or cellular interface. In addition, it also needs homogeneous liquid behind the solid-liquid interface.

d) Microanalysis of quenched equilibrated specimens

The specimen is held at the fixed temperature in the solid-liquid region for several hours to obtain thermodynamic equilibrium and then is rapidly quenched. The solid and liquid phases are analysed by the electron microprobe analyser. There are two major difficulties in the technique; quenching artefacts and cooling rate. Bastow and Kirkwood(87) showed that the cooling

rate can be raised by splat quenching. The other difficulty arises from the quenching artefact. Subramanian et al(79) pointed out that if this concentration rise just in front of the interface is avoided during measurement, then the actual equilibrium distribution coefficient can be determined. This suggestion can also explain the low value of ko, which was obtained previously by several workers in different systems. This technique recently has been employed in many alloy systems(44,69,58,81,82,84,88).

2.2.3 The equilibrium distribution coefficient in Fe-C-X alloys

Recently, Umeda et al and Kagawa(81) measured ko of manganese and other solute elements between the liquid and the austenite phase in carbon steels. These data have been checked thermodynamically by several workers in iron based alloys. The result is shown in figure 13. It is found that in the Fe-C-Si ternary system, the distribution coefficient of silicon was less than unity at the high temperatures or with low carbon concentration in the liquid, showing the same segregation tendency as in Fe-Si binary alloys. As the equilibrium temperature decreases, or the carbon concentration in the liquid increases, the distribution coefficient of silicon increases remarkably. A noticeable dependence of the coefficient on silicon concentration is also observed at the low temperature. In the Fe-C-Mn ternary system, the distribution coefficient of manganese decreases with temperature and the dependences of both the coefficients for manganese and carbon on the manganese concentration are small. The addition of 1 % Mn to Fe-C-Si alloys

causes an increase in the distribution coefficient of manganese itself at low temperatures, especially at the higher silicon levels, while the effect of the addition of manganese on the distribution coefficients of silicon and carbon is small.

2.3 Models of microsegregation

2.3.1 Solidification near equilibrium

Under equilibrium solidification, the diffusion in both solid and liquid phases is complete, so that homogeneous concentration across phases is maintained during growth. The mass balance is expressed as

$$C_s f_s + C_l f_l = C_o \qquad 2.8$$

$$C_s = \frac{k_o C_o}{f_s(k_o - 1) + 1} \qquad 2.9$$

where C_o initial concentration

C_i concentration in phase i

f_i fraction of phase i

This is known as the equilibrium lever rule. This situation can be realised in practice only for interstitial solute alloys, such as Fe-C , Fe-N, in the case of slow cooling.

2.3.2 Non-equilibrium solidification models

The first attempts to predict microsegregation quantitatively were derived by Gulliver(89) and Scheil(90) and the equation is

known as Scheil equation. It is assumed that there is complete mixing of solute in the liquid but no diffusion of solute in the solid can occur and local thermodynamic equilibrium exists at the solid-liquid interface, described by a constant equilibrium distribution coefficient and negligible undercooling occurs at the tip. This equation is

$$Cs = ko\ Co \left(1 - fs \right)^{ko-1} \qquad 2.10$$

where fs fraction of solid

and it predicts the worst segregation values.

Since the introduction of the probe microanalysis technique in the late 1950s, it was shown that the assumption of no solid state diffusion is unjustified. Brody and Flemings(74) recognized this and presented an analysis which quantifies the effect of solid state diffusion occurring between the Scheil and lever rule cases (without changing other assumptions of the Scheil equation). They considered a primary or secondary arm as a volume element with planar interface. Their analytical solutions for both linear and parabolic growth rates are

$$Cs = ko\ Co \left(1 - \frac{fs}{1 + \alpha ko} \right)^{ko-1} \quad \text{for linear growth} \qquad 2.11$$

$$C_s = k_o C_o \left[1 - (1 - 2\alpha k_o) f_s \right]^{\frac{k_o - 1}{1 - 2\alpha k_o}} \quad \text{for parabolic growth} \quad 2.12$$

where

$$\alpha = \frac{D_s \theta_f}{l^2}$$

l = 1/2 half element length

The dimensionless group α determines the extent of diffusion in the solid phase. If $\alpha << 1$, microsegregation approaches the Scheil equation. If $\alpha >> 1$, uniform composition is obtained. However, this treatment does not conserve solute, especially for fast diffusing elements, such as C, S, and P.

Clyne and Kurz(91) examined the influence of rapid solid-state diffusion in solidification, particularly for cast iron and steel. This is accompanied by the rapid interstitial diffusion of carbon, which influences the estimation of the freezing range and mushy zone characteristics of this type of alloy. They derived a relationship involving a modified function for α, in a heuristic way rather than by a mathematical procedure. The Ω replaced by α is

$$\Omega = \alpha \left[1 - \exp\left(-\frac{1}{\alpha} \right) \right] - \frac{1}{2} \exp\left(-\frac{1}{2\alpha} \right) \qquad 2.13$$

Recently, Ohnaka(92) has criticised this method and solved the back diffusion equation approximately for the one and two-

dimensional cases. He assumed that the solute profile in the solid can be expressed with a quadratic equation, then he obtained the following equation

$$C_s = k_o C_o \left(1 - \Gamma f_s \right)^{-\frac{k_o - 1}{\Gamma}} \qquad 2.14$$

where

$$\Gamma = 1 - \frac{\beta}{1 + \beta}$$

In this equation $\beta = 2\alpha$ and 4α for the plate and the columnar models, respectively. Comparing with the Kurz-Fisher equation he replaced Ω with

$$\Gamma = \frac{\beta}{1 + \beta} \qquad 2.15$$

In the columnar model, he assumed that the arrangement of primary dendrite arms is hexagonal close packed and he simply used a relationship between the diffusion area and the distance from the dendrite centre for two dimensional back diffusion. His results showed that his equation can estimate the liquid concentration better than the Brody-Flemings' solution but it gives similar results to the Clyne-Kurz solution. He suggested that numerical calculation or exact solution of back diffusion is required for further improvement. In addition, his numerical calculation showed that the assumption of dendrite shape, growth

mode (parabolic or constant growth) and diffusion in liquid phase did not affect so much the solute redistribution, at least for fs < 0.9, but indicated that the diffusion path length is a more important factor.

However, these attempts do not conserve solute in the system. Kobayashi(93-95) criticised all these equations, especially for fast diffusion case, i.e. $\alpha >> 1$. He solved the back diffusion equation in the solid for moving boundary conditions and obtained the exact solution of the Brody-Flemings equation :

$$Cs(fs, x^*) = ko\, Co \sum_{n=0}^{\infty} \xi_n \frac{F\left(-\frac{n}{2}, \frac{1}{2}, -\frac{x^*}{2\alpha}\right)}{F\left(-\frac{n}{2}, \frac{1}{2}, -\frac{1}{2\alpha}\right)} fs^n \qquad 2.16$$

$$\text{where} \quad \xi_n = \prod_{m=0}^{n-1} \left(1 - ko \frac{F\left(-\frac{m}{2}, \frac{3}{2}, -\frac{1}{2\alpha}\right)}{F\left(-\frac{m}{2}, \frac{1}{2}, -\frac{1}{2\alpha}\right)} \right) \qquad 2.17$$

$$F(p, q, z) = \sum_{r=0}^{\infty} \frac{(p)_r}{(q)_r} \frac{z^r}{r!} \qquad 2.18$$

x^* : fraction of solidified distance

(P) and (q) are the Pochhammer symbols which are defined by

$$(P)_r = P (P + 1) \ldots \ldots \ldots \ldots (P + R - 1)$$

$$(P)_0 = 1 \quad \text{etc.}$$

At the solid-liquid interface

$$C_s = k_o C_o \sum_{n=0}^{\infty} \xi_n f_s^n \qquad 2.19$$

This equation can be simplified approximately for very fast diffusion case, i.e. $\alpha >> 1$; then it becomes :

$$C_s(f_s, x^*) = \frac{k_o C_o}{1-(1-k_o)f_s} - \frac{k_o C_o(1-x^{*2})(1-k_o)f_s}{2\alpha(1-(1-k_o)f_s)^2} + \frac{k_o^2(1-k_o)C_o f_s^2}{3\alpha((1-k_o)f_s)^3} \qquad 2.20$$

He also simplified this exact solution for the very slow diffusion in solid case. He solved the second order differential equation for the first order approximation and the second order approximation cases. The second order approximation equation is

$$C_s = k_o C_o\left[1 + \Gamma\left\{\left(1-\frac{1+\beta}{2}k_o\right)\left(\frac{1}{\xi^2}-1\right) - 5\left(1-\frac{2+3\beta}{5}k_o\right)\left(\frac{1}{\xi}-1\right) - 3\left(1-\frac{1+2\beta}{3}k_o\right)\ln\xi\right\}\right] \qquad 2.21$$

where $\beta = \frac{\alpha}{1+\alpha}$ $\quad \alpha = \frac{8 D t_f}{\lambda^2}$ $\quad \Gamma = \frac{k_o(1-k_o)\beta^3}{2\alpha(1-\beta k)^3}$

When k is close to one, this equation becomes very close to the Brody-Flemings' solution.

He compared this exact solution with other equations for the fast diffusion element case. It is shown that the Brody-Flemings'

equation always underestimates the segregation and the Clyne-Kurz solution and the Ohnaka solution show almost the same result, because these models do not conserve totally the solute mass balance in the system. However, his solution for phosphorus and sulphur maintained the mass balance in the unit cell and therefore estimated the segregation correctly. For carbon, almost equilibrium solidification is obtained. When he calculated the average concentration numerically with an integration step of 0.001, the result was very close to the original composition; therefore, the exact solution maintained the mass balance in the system.

In his further treatment, he applied this exact solution for the hexagonal columnar dendrite model proposed by Ohnaka. It was shown that the assumption of the solidification geometry is unimportant for quantifying the microsegregation effects and he agrees with Ohnaka's result. However, these models can be only used for primary dendrite arms at very slow cooling rates, because it has been shown in this study that the morphology of primary dendrite arms becomes well developed at the high cooling rates and the secondary dendrite arm coarsening reduces the segregation between the secondary arms. These two significant effects have been ignored; therefore these models can predict the segregation only for the very limited case and the neglect of the solidification geometry on the solute distribution is an unjustified assumption.

a) Incomplete diffusion in liquid and solute flow

Bower et al(26) examined the validity of solute flow from

volume element and complete diffusion in the liquid assumptions. They pointed out that there could be significant flow of solute from the volume element by diffusion along the composition gradient in the liquid at sufficiently steep thermal gradients and long solidification times. In this case the interface composition would no longer be given by the Scheil equation. They modified this expression as

$$C_s = k_o C_o \left\{ \frac{\alpha}{k_o - 1} + \left[1 - \frac{\alpha k_o}{k_o - 1} \right] (1 - f_s)^{k_o - 1} \right\} \quad 2.22$$

where $\alpha = \frac{D_l}{C_o} \frac{G_l}{V} \frac{}{\beta}$

D_l diffusion in liquid

G_l thermal gradient in liquid

This equation reduces to the Scheil equation where $\alpha << 1$.

In the previous model of Brody and Flemings, they showed that diffusion in the solid during dendritic solidification depends on the parameter, α. By similar procedure it is readily shown for the plate-like dendrite model growing as a continuous function of time that the extent of diffusion in the liquid depends on the parameter

$$\alpha_l = \frac{D_l \theta_f}{l^2} \quad 2.23$$

When $\alpha_\ell \gg 1$, concentration differences in liquid over the distance L are small. For constant local growth rate, V, an equivalent method of determining whether or not significant composition differences can exist in the liquid, is to compare the characteristic distance of solute build-up $\frac{D_\ell}{V}$ .with the half dendrite arm spacing L. When $D_\ell / V \gg L$, negligible composition differences exist over L. Bower et al took L to be the secondary arm spacing. They calculated that α_ℓ varied between 300 to 5000 for a wide range of experimental aluminium castings and deduced that the complete mixing assumption is generally valid.

Rohatgi and Adams(96) discussed the complete diffusion in liquid assumption with a different approach. These authors analysed diffusion in the interdendritic liquid, and found that concentration differences should exist within the liquid. They calculated that the concentration difference between center and side of an interdendritic pool is

$$\Delta C_o = \frac{C_o (1-k_o) \lambda_1^2}{8 D_\ell} \frac{df_s}{dt} \qquad 2.24$$

These two approaches seem to conflict. The Bower et al analysis suggests that interdendritic concentration differences becomes negligibly small after sufficient time has elapsed. The Rohatgi and Adams analysis suggests that interdendritic concentration differences do not depend directly on the time, and remain finite throughout solidification.

Allen and Hunt(97) gave an explanation for this conflict. They

defined two regions for diffusion field between primary arms, the transient diffusion field at the near dendrite tips and the quasi-stationary diffusion field at the later stages of solidification. They showed that α is a measure of the ratio of the time taken for the diffusion fields to overlap (θ_t) to the total solidification time (θ_f)

i.e. $$\alpha = \frac{\theta_t}{\theta_f} \qquad 2.25$$

$\alpha \gg 1$ is a necessary condition for the applicability of the complete mixing model. They also showed that during transient, the width of the primary arm diffusion field is $x_t \cong \sqrt{D_e \cdot t}$ approximately. The formula $x_t = \left(\frac{D_e}{V}\right)$ is usually inapplicable. It is further pointed out that the concentration difference in liquid at the quasi-stationary stage can be calculated from this equation

$$\Delta C = -\frac{1}{2}\frac{W}{\beta D_l}\left(x - \frac{\Delta_1}{2}\right)^2 \qquad 2.26$$

where w cooling rate

x = 1/2 thickness of primary dendrite

This is a modified form of the analysis of Rohatgi and Adams. The analysis of the quasi-stationary state is essentially quite accurate, but the assumed geometry is simplified as cellular

structure. When diffusion occurs in two or three dimensions, the curvature of the diffusion field in any one direction is reduced. In addition, side-branching reduces the dendrite spacing. Under these circumstances, the concentration difference will be reduced and therefore, the validity of complete diffusion in the liquid assumption will be often justified.

Furthermore, the numerical calculation of Ohnaka(92) and Roozs et al(117) showed that the complete diffusion in the liquid assumption is justified under the practical solidification conditions. These conlusions agree with the result of Bower et al.

b) Undercooling

Solari and Biloni(98) examined the zero undercooling assumption. They suggested an equation which is a combination of the Burden and Hunt model for dendrite tip undercooling with the Brody- Flemings microsegregation equation for the primary arms. The equation becomes

$$C_s = k_o C_o \left[\frac{a}{k_o} - \frac{b}{1} + \left\{ \frac{(a-b)k_o}{1} \right\} \left\{ 1 - \frac{f_s}{1+\alpha k_o} \right\}^{k_o-1} \right] \quad 2.27$$

where $a = \frac{D_l}{\beta} \frac{G_l}{V C_o}$

$$b = \left[\frac{\Gamma V}{\beta D_l} \frac{(1-k_o)}{C_o} \right]^{1/2} \qquad \alpha = \frac{4 D_s \theta_f}{\lambda_1^2}$$

When $a = b = \alpha = 0$, the Scheil equation is obtained. If $\alpha \neq 0$ and $a = b = 0$, it reduces to the Brody and Flemings equation. This treatment is criticised by Ogilvy. He asks whether these two combined models are compatible or not, because Burden and Hunt allowed the free growth of a single dendrite and considered the undercooling at the tip, while Solari and Biloni constrained the sideways growth of the primary arm to a linear rate and then used the tip concentration predicted by the first approach to derive their equation. In addition, their analytical solution also contains the same approximation for the solute gradient in the solid at the interface as used by Brody and Flemings, therefore this treatment does not conserve solute in the volume element.

Recently, Kirkwood(99) checked the undercooling influence on microsegregation in different commercial processes by employing the Burden and Hunt's undercooling equation. Calculations in Al-4.5 % Cu alloy showed that negligible undercooling (1-2 K) occurs in many processes from the point of view of microsegregation. It was pointed out that undercooling will significantly affect microsegregation only at high growth rates. These conditions can be achieved in processes such as splat-quenching, electron beam and laser surface melting.

c) Dendrite arm coarsening

All these analytical solutions ignore the coarsening of secondary dendrite arms. In fact, it has been recognised by Flemings et al that this effect is mainly responsible for the reduction in microsegregation, rather than other variables

discussed above. Ogilvy and Kirkwood(113) proposed an equation to include this coarsening effect by ripening. Unfortunately, this equation has no analytical solution. The numerical solution is given in the computer modelling chapter.

Recently, Mortensen(66) presented a simple analytical treatment of the influence of coarsening by ripening on microsegregation. In his model, a large number of cylindrical dendrite arms are considered, each arm having a radius, r^*, The other assumptions of the model are the same as the Scheil model. The solute balance under this condition is

$$\overline{C_s}\ \pi\ r^{*2}\ L\ +\ C_l\ \pi\ (r_T^2 - r^{*2})\ L\ =\ C_o\ \pi\ r^{*2}\ L \qquad 2.28$$

where $\overline{C_s}$ is the average solute concentration in the solid

L is the dendrite arm length

After a finite time interval, the radius increases; therefore by differentiating the equation 2.28 with respect to time, we can obtain

$$\frac{\partial(\overline{C_s}\,r^{*2})}{\partial t} + (r_T^2 - r^{*2})\frac{\partial C_l}{\partial t} - 2C_l r^* \frac{\partial r}{\partial t} + 2(C_l - C_o) r \frac{\partial r}{\partial t} = 0 \qquad 2.29$$

He assumed that :

i) there is no back diffusion in solid

ii) secondary dendrite arms coarsen according to the equation

$$r_T^n - r_o^n = B^n t \qquad 2.30$$

iii) the cooling rate is constant, so that the liquid composition can be expressed by

$$Cl = Co + A\,t \qquad 2.31$$

where $A = \frac{W}{\beta}$

W = cooling rate

After some treatment, we can obtain the final solution

$$\left(\frac{r^*}{r_T}\right)^2 = \frac{1 + \frac{2}{n}}{1 - ko} \frac{Cl^{[1/(ko-1)]}}{(Cl - Co)^{2/n}} \int_{Co}^{Cl} Cl^{[k/(1-k)]} (C-Co)^{2/n} dC \qquad 2.32$$

where $\left(\frac{r^*}{r_T}\right)^2$ is the volume fraction of solid

This equation is a nonequilibrium lever rule including ripening. It will be noticed that when $n \longrightarrow \infty$, this expression reduces to the Scheil equation and no ripening occurs under this limiting case. The integral can be calculated analytically if 2/n is an integer.

When he compared his equation in Al- 4.5 % Cu and Sn- 12-30 % Bi alloys for planar, cylindrical and spherical geometries, he found that the prediction of his treatment gives higher estimates than

experimental results. He explained this difference with the coarsening mechanism. He suggested that at the low volume fraction of solid, ripening is predominant, whereas coalescence gains in importance only at higher volume fraction of solid. Therefore, by considering the coarsening mechanism only with the ripening, the model overdilutes the solution. When he plotted the calculated volume percent eutectic against the volume fraction of solid, he found that if ripening is taken to be predominant up to around 40-60 percent volume fraction of solid, reasonable agreement can be obtained with experimental results. He further pointed out that the influence of coarsening on microsegregation is independent of the cooling rate and of the coarsening law constant.

This simple attempt only demonstrated that the side arm coarsening reduces microsegregation. On the other hand, the model ignores the back diffusion which is significantly important factor for the reduction of microsegregation. The other critical suggestion that ripening is predominant up to 40-60 percent volume fraction is not based on any observation. It is just arbitrarily used in order to force agreement between calculations and experimental results.

Generally, all these models in this part were proposed for binary alloys, but they have no flexibility to be applied for multicomponent systems. In practice, alloys contain several elements which may interact with each other, therefore numerical calculations are necessarily required to overcome this and many other problems.

2.3.3 Numerical calculations

When Brody-Flemings(73,74) first employed the numerical method in Al-Cu alloys to examine the effect of back diffusion in microsegregation, their model overestimated the quantity of non-equilibrium eutectic phase. They explained this discrepency by suggesting that a smaller arm spacing must be used in the model by a factor of 0.32; then reasonable agreement can be obtained with the experimental results. Later, they applied this model to iron alloys and found that these alloys also needed a similar correction factor. This factor is 0.13 for primary arms and 0.30 for secondary arms. This difference between the actual and calculated segregation was related to the actual morphology of dendrites which are much more complex than the simple plate-like morphology. Flemings et al also observed in iron alloys that the segregation between primary arms was higher than between secondary arms and the dendrite morphology changed from rod-like to plate-like with decreasing the cooling rate.

Flemings et al used the constant cooling rate assumption in their model. Later, Kirkwood and Evans(100) replaced this with the constant heat extraction assumption. Their result showed more accurate agreement in Al-Cu and Fe-As alloys. It was suggested that the model needs reliable diffusion data as a function of temperature and composition, to improve the agreement between the measured and calculated results.

Schwerdtfeger(101) also applied the Brody-Flemings model to the numerical calculation of manganese segregation and the formation of the sulphur inclusion. He found that the manganese segregation

increases from the chill region (S= Cmax/Cmin= 1.5) to the center (S= 2.5) in the 50 kg ingot, whereas the model gives a constant manganese segregation (2.2). They used the actual primary arm spacing which was measured in ingot specimens, but the spacing was not specified. In addition, the diffusion coefficient was taken from Wells and Mehl (1941), whereas the distribution coefficient (kmn= 0.75 for austenite) was taken from Buckley and Hume-Rothery (1964). However, more recently, it has been shown that the diffusion coefficient suggested by Haworth(165) gives more accurate results when kmn= 0.78 is used. These values have been used in the present study. He also used the binary differential form of the Brody and Flemings equation in numerical calculations of manganese segregation in ternary Fe-C-Mn alloy. It simply ignored the carbon effect which mainly defines the solidification range.

Matsumiya et al(102-103) proposed a simple cellular hexagonal solidification model including $\delta \rightarrow \gamma$ phase transformation. This model can explain the solute redistribution at the slow cooling rate. However, this is not a correct geometrical description at high cooling rates because the structure changes from cellular to well developed dendritic. As a result of this, the model does not agree well with experimental results. They also experimentally and numerically found that the microsegregation could decrease by the addition of ferrite forming elements, and on the other hand it could increase by addition of austenite forming elements. This is explained by the fact that the addition of ferrite forming elements causes an increase in the extent of diffusion in the

solid.

Kobayashi et al(105,106) extended the Kobayashi exact solution to the numerical calculation procedure employing temperature dependent diffusion coefficient and including the peritectic reaction. They solved the back diffusion and heat conduction equations, simultaneously. They assumed that :

i) the dendrite morphology is plate-like

ii) the distribution coefficient is constant throughout solidification and independent of alloy content

iii) the alloy is ideal, so that the Raoultian ideal law can be used to predict the equilibrium phase diagram of a multicomponent alloy system.

The result of the model was compared with the thermal analysis rather than the solute redistribution. They found reasonable agreement between the thermal analysis of different low carbon steels and calculated results.

Recently, Clyne(107) and Cornellissen(108) combined the heat transfer analysis with microsegregation models. Clyne has combined a general macroscopic heat transfer model with the Clyne-Kurz equation, whereas Cornellissen combined his microsegregation approach (modified form of Clyne-Kurz) with the macroscopic heat transfer equation to include the peritectic reaction. However, these simple models were not compared with experimental results for solute redistribution. In addition, Cornellissen used secondary arm spacings in the Clyne-Kurz equation and obtained the microsegregation of manganese as 1.6, even for very low carbon steel (0.04 % C - 0.24 % Mn). In fact, this equation cannot apply to the secondary dendrite arms because

it does not consider the dendrite coarsening effect. Therefore it overestimates the actual solute segregation.

Battle and Pehlke(109) also proposed a microsegregation model with combining macroscopic heat transfer analysis to allow for prediction of solute redistributions throughout actual castings. Several complicated differential equations were solved. Suprisingly, this model gives similar results to the Ogilvy and Kirkwood dendrite arm coarsening model, although they used a constant secondary arm spacing. It was difficult to understand in the paper how these results were achieved without arm coarsening. But the model underestimated the Ni microsegregation in Fe-25 % Ni alloy.

Feest and Doherty(110,111) observed significant undercooling in equiaxed solidification of Ni-Cu alloys as Doherty and Melford observed in Fe-C-Cr alloys. In order to explain this effect, they suggested five different equiaxed microsegregation models and compared them with experimental results using measured morphological and undercooling data. Two of models employed the Brody-Flemings equation with and without the imposed tip undercooling of 5 deg C in Cu - 40 % Ni. The other two are based on cylindrical arms with and without the tip undercooling, the last one used the Brody-Flemings model with half of the final arm spacing allowing coarsening during growth. However, calculations were made up to fs=0.25 because the program became unstable. The result showed that the minimum concentration of Ni can be predicted, if models allow undercooling or coarsening. They assumed that the rest of solidification (75 %) can not alter

the result, although back diffusion continues. This coarsening model does not conserve solute.

A simple dendrite coarsening model was proposed by Basaran(112) He considered three different arm coarsening models.

a) dissolution of small arms

b) dissolution of arms from root

c) combination of a and b

In the model, the secondary arm spacing increases with this equation

$$L = \frac{3.75}{n} \left(\theta_f \right)^{0.39} \qquad 2.33$$

where n depends on coarsening mechanism

He simply modified the Brody-Flemings equation to the dendrite arm coarsening case. However, this equation does not conserve solute in the cell element because the extra liquid volume was added to the existing liquid. Data used in the model are unchanged from the 1966 work and this was criticised by Ogilvy.

Ogilvy and Kirkwood(58,99) recognized that the coarsening of secondary dendrite arm is an important homogenization process. This homogenization can explain the underestimation of segregation in alloys. Then they modified the Brody-Flemings equation correctly to account for secondary arm coarsening and proposed a more complete segregation equation. In order to maintain the mass balance in the model, the liquid at the average composition was added to the system (Details are given in the computer modelling chapter). This dilutes the liquid

continuously. The second advantage of this numerical calculation is that it increases the back diffusion by using the actual diffusion length during solidification. When Ogilvy compared this model in Al-4.17 % Cu alloy, very close agreement was found for the minimum solute content as well as a fair general agreement of the shape of the solute redistribution. He also compared the amount of non-equilibrium eutectic with the secondary dendrite arm coarsening model and the constant secondary dendrite arm model and with two analytical solutions for large solidification range. It was found that both the numerical calculations show better agreement with the experimental results of Michael and Bewer than the analytical models (Brody-Flemings and Clyne-Kurz). But the constant arm spacing model overestimates slightly the total eutectic, whereas the secondary dendrite arm coarsening model underestimates it slightly. The model variables such as temperature-dependent and fixed diffusion coefficient and different equilibrium distribution coefficients, were compared by Kirkwood with keff in Al-5 % Cu alloy. It is found that the excellent agreement is obtained with keff (0.34 from Bennett(166)) when the dendrite arm coarsening equation is used with the constant distribution coefficient, kcu=0.20, and the temperature dependent diffusion coefficient. This model was later modified by Ogilvy and Kirkwood(113) for ternary and multicomponent systems and iron alloys with constant cooling rate, where no growth law or local solidification time was imposed. These models are used in the present study. Howe and Kirkwood(114,115) extended these models to the peritectic reaction. It is assumed that the composition is uniform in the delta ferrite and in the liquid.

When the austenite forms, the solute diffusion balance for a subsititional element is

$$B_l(1-k^b_{\gamma/l})\frac{\partial X_2}{\partial t} = D_\gamma\left(\frac{\partial B}{\partial x}\right) + (L-X_2)\frac{\partial B_l}{\partial t} + (B_l-B_o)\frac{\partial L}{\partial t} \qquad 2.34$$

Solute balance at the austenite-delta ferrite interface is

$$B_{\gamma/\delta}\,(1-k^c_{\delta/\gamma})\frac{\partial X_1}{\partial t} = D_\delta\frac{\partial B_{\delta/\gamma}}{\partial x} - D_\gamma\frac{\partial B_{\gamma/\delta}}{\partial x} \qquad 2.35$$

Solute balance for carbon in equilibrium across the whole cell is

$$\left\{(k^c_{\gamma/l} - k^c_{\delta/l})\frac{\partial X_1}{\partial t} + (1 - k^c_{\gamma/l})\frac{\partial X_2}{\partial t}\right\} = \left\{ X_1\, k^c{}_{\delta/l} + (X_2 - X_1)\, k^c_{\gamma/l} + (L - X_2)\right\}\frac{\partial C_l}{\partial t} + (C_l - C_o)\frac{\partial L}{\partial t} \qquad 2.36$$

Roozs et al(116-119) proposed two microsegregation models assuming incomplete diffusion in the liquid in the first model and dendrite arm coarsening in the second model. The result of the first model showed that the complete diffusion in the liquid phase assumption is true under the practical solidification conditions. Only the rapid solidification needs finite diffusion

rates in the liquid. On the other hand, they extended this numerical procedure to the secondary dendrite arm coarsening case using the Ogilvy-Kirkwood mass balance equation. However, the most critical assumption in the model is that they employed a semi-empirical dendrite coarsening equation, while Ogilvy and Kirkwood employed an empirical one. This semi empirical equation which they suggested introduces a geometric factor. This factor was calculated in a heuristic way rather than any physical way and plays a correction factor role in the coarsening equation. In fact, originally, this had been suggested by Flemings and co-workers. The coarsening model also assumed that the dendrite arm spacing is proportional to $t^{1/3}$. However, it has been shown that the exponent in the equation can vary from one alloy to another.

Miettinen(120,121) also presented a multicomponent model. This model is based on thermodynamic and kinetic calculations made on a volume element of the secondary arm. It was assumed that the local thermodynamic equilibrium at the solid/liquid interface determines the distribution of solutes. This is obtained from the equilibrium chemical potential equation, but approximate data were often used in the case of multicomponent systems, because of limited available data in the literature. Although the model considers the secondary arm spacing as a volume element, it does not take account of the dendrite arm coarsening.

All these models ignored the TGZM effect. Recently, Lalli(122) presented a numerical model for Al-Cu alloys to include TGZM. The model solved the moving boundary diffusion equation in the liquid

and in the solid. It is found that the minimum copper concentration increases with temperature gradient (0.5 % Cu for 2.8 deg °C/mm and 1.3 % Cu for 11 deg °C/mm) at the constant cooling rate and alloy composition, whereas the volume percent of eutectic decreases under the same conditions. However, there is no clear evidence in the literature to compare this model with experimental results. In order to make clear the effect of the TGZM, more experimental work needs to be done in different systems.

CHAPTER 3 EQUILIBRIUM DIAGRAMS

3.1 Fe-C

Several reviews have been done on the Fe-C equilibrium phase diagram(123-125). Chipman(126) put together the more recent data in 1971 and it is in general agreement with his thermodynamic analysis. This diagram and its peritectic corner is given in figure 14. The liquidus of ferrite phase is shown as a straight line from the melting point to 0.53 % C at peritectic. The reaction here is

$$\delta\text{-Fe}\ (\ 0.09\ \%\ C\ )\ +\ L\ (\ 0.53\ \%\ C\ )\ \rightleftharpoons\ \gamma\text{-Fe}\ (\ 0.17\ \%\ C\ )$$

3.2 Fe-Mn

The Fe-Mn equilibrium binary phase diagram is based on Hellawall(127) as shown in figure 15. In the Fe-rich alloys, the liquidus falls to meet a peritectic at 1473 C. The peritectic is

$$\delta\text{-Fe}\ (\ 9.5\ \%\ Mn\ )\ +\ L\ (\ 12.8\ \%\ Mn\ )\ \rightleftharpoons\ \gamma\text{-Fe}(10.2\ \%\ Mn\ )$$

At high Mn contents, the liquidus and the solidus fall to a minimum near 87 % Mn at about 1232 C. The nature of the Mn -rich region is uncertain.

3.3 C- Mn

Only the Mn- Rich region has been analysed because of the formation of numerous carbides(128-130). The most reliable binary diagram is shown in figure 16.

3.4 Fe-C-Mn

The liquidus and the solidus equilibrium isotherm have been studied by Vogel and Doring(131), Schurmann and Geissler(129). But none of them carried out a detailed investigation into the peritectic Fe- rich corner. Recently, Scmithmann and Rakoski(132) examined the peritectic corner at the composition of 1.5 % Mn in the carbon range of 0.015 to 1 % C. An increase in Mn raises the peritectic temperature and reduces the peritectic carbon concentration. The peritectic reaction occurs within a temperature range (figure 17).

3.5 Peritectic reaction

Many steels and other alloys undergo the peritectic reaction during solidification. Recently, much attention has been drawn to the microsegregation of these kinds of steels, simply because the pre-peritectic phase, which is ferrite, has much higher diffusivity than the product of the peritectic reaction, which is austenite. This causes less segregation of solute elements in the product.

The peritectic reaction takes place between a solid and a liquid phase to produce a second solid phase. Its name originates from 'periphery', because the second phase usually grows around the periphery of the primary phase.

$$\alpha + L \rightleftharpoons \beta$$

Kerr et al(133) distinguished the definition of the peritectic reaction and the transformation. During the peritectic

reaction, all three phases are in contact with each other. In the case of peritectic transformation, the second phase isolates the primary phase from the liquid and grows into both these phases. This transformation is controlled by long-range diffusion. In this case, the diffusion coefficient becomes very significant, as well as the distribution coefficients. It is reported that the peritectic reaction and the growth occur in two different forms: the homogeneous nucleation of the second phase in the liquid without contact with the primary phase, the heterogeneous nucleation of the second phase on the primary solid phase. The first kind of the reaction rarely happens in metallic alloys and is only observed in Al-Mn, Ni-Zn and Al-U systems. This is explained by the surface energy conditions. During the transformation, the primary phase remelts and the second phase grows separately and produces different morphology to the primary phase. The second type of reaction is most commonly met in practice. The second phase is nucleated at the interface between the primary and the liquid phases. Under these circumstances, the growth of the second phase is controlled by the shape of the phase diagram, the cooling rate, the diffusion process and the concentration. The growth rate increases with the undercooling at the peritectic temperature, whereas the volume fraction of primary phase decreases under the same conditions. The second phase mostly grows from the liquid if the second phase has face-centre cubic structure, which has a lower diffusivity than body-centre cubic crystals. For body-centre cubic metals, the second phase grows into both phases(134).

Kerr et al(133) investigated the peritectic reaction in

Al-0.1-0.8 % Ti alloys under different cooling rates. At slow cooling rates, the equilibrium peritectic reaction was observed. The primary Al_3Ti phase reacting with the liquid produce α-Al phase. The thermal analysis showed a plateau at the peritectic reaction due to the heat release as expected. However, with fast cooling rates, no plateau was observed and the microstructure only consisted of α - Al. This is explained by the extension of the liquidus line of second phase which becomes stable at high undercoolings, so that the α - Al nucleation starts above the peritectic temperature and below the extension of the liquidus line of the second phase. It was further pointed out that the amount of the pre-peritectic phase decreases with increasing the cooling rate and the structure becomes more irregular.

Chalmers(37) suggested that if the temperature gradient is steep enough, then the planar interface with two coupled solid phases can be obtained like eutectic alloys.

This effect was observed for the first time by Boettinger(135) in Sn-Cd alloys by varying the G/V ratio. At the low value of G/V, the dendritic or cellular type of peritectic reaction was observed. The volume fraction of the second phase increases slightly behind interface during cooling. This indicates the existence of the solid-state diffusion in these alloys. At the moderate value of G/V, the primary phase grows with the second phase at the planar interface with high undercooling. This produces a banded microstructure which consists of one layer of the primary and one layer of the second phase continuously. In

the case of high value of G/V, the formation of primary phase is suppressed and only the second phase grows as a single planar interface. The growth temperature of this phase was above the peritectic temperature. Similar results were obtained by Brody and David(136) in the same alloys and Pb-Bi alloys. Ostrowski and Langer(137) reported the banded microstructure in Zn- 10 % Ag alloy at a high value of G/V.

The investigation of the peritectic reaction is more difficult in steels because of high back diffusion of carbon. In the early years, the thermal analysis was used to determine the peritectic range in industrial steels. These results showed that the length of the peritectic arrest decreased with carbon due to the $\delta \rightarrow \gamma$ solid-state transformation(138, 139).

Fredriksson et al(140-143) investigated the peritectic reaction in Fe-Ni and ferrous alloys under different cooling rates. They defined a critical line which is below the extension of austenite liquidus into the metastable phase. Under these circumstances, ferrite can form at low undercoolings, where austenite can also form between the critical line and the extension of the liquidus of austenite, but ferrite grows faster than austenite and becomes dominant during solidification. However, if undercooling increases below the critical line, ferrite is suppressed and only austenite grows as a stable phase. A similar result was observed in Fe-C-Mn alloys(48) and microsegregation was higher than near equilibrium solidification. However this conclusion in Fe-C-Mn alloys has not properly been proved with microprobe analysis because of limited results.

Fredriksson(141) observed that the peritectic reaction temperature decreased with increasing cooling rate in the high speed steels and high chromium alloyed steels. Remelting in the center of secondary dendrites was also observed. During the peritectic transformation, the tungsten concentration in the ferrite increases as the delta phase size is reduced. As a result, the chemical potential of the carbon is also reduced and carbon diffuses into the centre raising the concentration in the delta phase. As it is known, the carbon determines the liquidus temperature, so that this highly concentrated delta phase remelts at the interface between the ferrite and austenite phases during solidification. This has also been reported by Ogilvy(57).

Chadwick(144) examined the phase orientation in the peritectic reaction of Fe-C alloys. It was pointed out that if austenite phase grows with an orientation relationship of <100> //<100>, then the austenite deposites uniformly around the ferrite. If this crystallographic relationship is not realized, the dendrite growth form will change way through the solidification process and the resulting segregation pattern will be complex. The effect will not be important for plain carbon steels, because the carbon will readily diffuse in the solid phase and produce homogeneous solid, but when substitutional solutes are present, the segregation can change.

Recently, several attempts have been made at modelling of the peritectic reaction. The most recent one is proposed by Howe and Kirkwood. This model is given briefly in the previous chapter. Later, this model was modified to consider diffusion in both phases.

CHAPTER 4 EXPERIMENTAL PROCEDURE

4.1 Unidirectional solidification

The unidirectional growth technique was developed by Chalmers(145) and later used by many investigators to simulate the solidification of alloys during the casting process. The main advantage of this method is that the growth rate and the temperature gradient can be independently varied. In addition, the growing interface and the growth structure can be retained by quenching into water.

It is assumed in all unidirectional work that the steady-state conditions are achieved very rapidly and the primary dendrite tips grow at the traverse speed of specimen crucible. Clyne(146) showed that these are unjustified assumptions under some conditions. He checked the velocity of the interface in the unidirectional solidification furnace by mechanically probing through the liquid with a ceramic rod, using commercially pure aluminium and found that the quasi-steady state conditions were obtained at the beginning and the end of specimen, whereas the conditions were steady state between these zones. The velocity of the advancing interface was significantly greater than the crucible speed. Further investigations (147) by the same researcher using a numerical model showed that this discrepancy was a function of length, thickness, velocity and the thermal diffusivity of the specimen and a function of furnace conditions. These computer results indicated that when the specimen was longer, thinner, and having faster growth rate, the advancing interface velocity was closer to the traverse speed. For example, the ratio between the interface velocity and the traverse speed of the crucible was 1.3

and 1.2 for a 130 mm long specimen of aluminium at 6 mm/min and 60 mm/min respectively. When the length of the specimen was increased to 200 mm, the difference was reduced to 1.15 and 1.05 for the same rates. It was shown that relatively low thermal diffusivity alloys, such as iron alloys, can exhibit an interface velocity closer to the traverse speed than do high thermal diffusivity alloys, such as aluminium. For example, the interface velocity was 1.3 times faster than the traverse speed for a 130 mm long aluminium specimen, whereas this ratio was 1.05 for cast iron under the same conditions. In the present work, it is believed that the specimen was long enough (200 mm) to ensure that the interface velocity was close to the traverse speed. Also Young(156) checked the interface speed in the unidirectional technique using two thermocouples and found that the specimen interface speed was fairly close to the traverse speed in aluminium alloys.

Neumann(148,149) presented one and two dimensional heat flow models for the directional solidification, which calculate the maximum curvature of the interface for single crystal growth. However, it is difficult to apply this computer model to the unidirectional solidification of dendritic structure. The metallographic examination of the dendrite tip does not indicate any apparent curvature of the interface.

El Mahallaway (150) investigated the effect of the presence of a thermocouple on the temperature gradient in the unidirectional aluminium specimen. From his computer model results, when the ratio of the alumina thermocouple sheath diameter to the specimen crucible diameter was 0.58, then the temperature gradient computed was 8 % less than the true gradient and the presence of

the thermocouple resulted in an increase of the curvature of the interface. In the present work, it is expected that this will be less than 8 %, because the ratio used was .33 and the thermal diffusivity of iron is closer to alumina than to aluminium.

It is possible that the argon gas flow rate may affect the thermal environment in the furnace, so that different temperature gradients can result for different gas flow rates. Although the gas flux was kept constant during all experimental works, the dendrite tip direction was not parallel to the heat flow direction in some specimen and one small region of the specimen remained liquid close to the dendrite tips, as shown in figure 36. These indicated that there was radial heat flux in the furnace. The difference in diameters between the specimen crucible and the graphite susceptor was 8 mm, so that ideally there should be a 4 mm gap on each side. In practice, it was almost impossible to hold the specimen in the middle of the graphite susceptor during growth, and this asymmetry of position resulted in heat extraction on one side being less than from the other regions. It is believed that this asymmetry caused the unbalanced radial heat flux, which was almost impossible to cure without redesigning the furnace.

4.1.1 Unidirectional solidification apparatus

The unidirectional solidification apparatus used in this work was originally designed and used by B.A. Rickinson(44) and later by A.J.W. Ogilvy(57). It has undergone only minor modifications. Initially, at the top of the furnace, the bellows and the

stainless steel supporting rod were left out and the top of the furnace was sealed by a copper plate. The copper plate had three holes with 0.5 mm outer diameter (O.D.) alumina cylindrical liners. The two holes were used for inserting the thermocouple wires, the middle one for suspending the specimen crucible with copper wire. At a later stage, the two holes were sealed and the thermocouple wires were inserted from the bottom end of the furnace.

The construction of the furnace is shown in figure 18,19. The isolation of the system from the atmosphere was provided by a recrystallized alumina tube,(65 cm length X 55 mm O.D. X 46 mm I.D.) and the top and the bottom were sealed by water cooled systems. The pure argon gas was admitted in from the top, exited from the bottom and the positive pressure was maintained by passing the gas through a mineral oil bubbler.

The graphite susceptor was situated in the middle of the furnace to provide a hot zone. This susceptor was supported from the bottom with another alumina tube. Alumina powder filled the gap between the small alumina tube and the main long alumina tube to promote uniaxial heat flow in the solidifying zone. This insulating system was also supported by a Sindanyo box filled with alumina powder up to the induction coil.

A 15 KW Radyne power unit supplied power to the furnace (1.9, 2.2 and 2.4 KW.) for three different induction coils, so that three different temperature gradients were obtained. The power was increased in four stages to above liquidus temperature of the alloys and decreased slowly over one hour to avoid any possibility of cracks as a result of thermal shock. Although

every precaution and care were taken, unfortunately, a crack on the alumina tube was seen, towards the end of work, around the bottom of the graphite susceptor. It is likely that this has not any effect on the results, because no gas leak was observed.

The speed was controlled by a Multur ten speed synchromesh gearbox and an electric motor. The motor was connected through a complex of pulleys to a copper weight, so that excessive loads were not transmitted to the motor. This system provided a range of speed from 0.03 to 30 mm/min.

4.1.2 Release and quench

The copper weight was connected through a complex system of pulleys to the driving unit by an one mm diameter flexible steel wire and the assembly was hung by a 0.5 mm diameter copper wire to this copper weight. When the copper wire was cut, the specimen assembly was released. The released specimen crucible tore the polythene membrane at the bottom of the furnace and was immediately quenched in the iced brine solution. In order to increase the efficiency of quenching, the solution was stirred by an one meter copper bar during quenching. The specimen crucible was cracked due to the thermal shock and only a small amount of liquid in the liquid zone usually flowed through the cracks. It is observed metallographically that this method allowed one to distinguish clearly between dendrites present before quenching and those formed during the quench.

4.1.3 Temperature gradient measurement

In order to measure the temperature gradients in the specimen, two methods were involved using a dummy specimen.

In the first method, a groove was machined along the specimen surface to a depth of 2 mm and this sample was placed at the top the specimen crucible which contained two 100 mm long specimens. The end of a 200 mm long recrystallized alumina sheath was closed by arc-welding to protect the thermocouple from the liquid metal and the alloy from any contamination, and inserted in the groove of the top specimen. The tip of the sheath was therefore in the middle of the specimens, so that measurements were taken in the steady state zone (see fig. 20) A 0.2 mm Pt-Pt 13 % Rh thermocouple was inserted into the thermocouple sheath and the top of the thermocouple was fixed to the thermocouple sheath by Autostick cement, to protect it from any independent movement during the run. The rest of the thermocouple gap was isolated by alumina beads up to the copper plate at the top of the furnace. The thermocouple wires were inserted through two holes in this plate and isolated from the copper plate by 10 mm long 0.5 mm diameter alumina tube. These wires were connected to leads. These connectors were fed through a cold junction to a Cambridge potentiometer and backed off, so that the remaining 2 mV was fed to the servoscribe. In this method, it was necessary to leave at least 200 mm thermocouple gap between the top of the crucible and the top of the furnace, because the thermocouple should be allowed to move with the specimen crucible when the specimen was traversed down and up. However, after a small movement, the thermocouple insulating beads were attached to the top of the graphite susceptor. This caused the movement of the specimen to stop or to unstabilize. From this method, accurate measurements could not be obtained.

In the second technique, the thermocouple sheath and, of course, the thermocouple were inserted to the specimen crucible from the bottom. In order to do this, the 110 mm long thermocouple sheath was sealed to the specimen crucible by CC 60 cement at 1200 deg C for 12 hours. Then the thrmocouple was placed in the middle of the specimens and was sealed to the sheath by Autostick cement. The extra length of the thermocouple was always at the bottom of the furnace, due to gravity and, also, there was no barrier in the bottom part of the furnace for it to attach to. After this modification to the first method,temperature gradients were recorded as defined above.

Knowing the chart speed and the growth rate, the temperature gradient could be determined. This was repeated for different growth rates and for three different induction coils. A new assembly was used for each different calibration. It was assumed that the temperature gradient in the specimens (without the alumina thermocouple) was same as in the dummy specimen. Therefore the possible effect of the alumina thermocouple sheath on the temperature gradiend has been ignored in the calculation of temperatures in figures 55-64 which may suffer from a small but unknown error. The absolute temperature is not important in the calculation of the temperature gradients since only the temperature differences are involved.

4.1.4 Alloy preparation

Alloys were made up from high purity Japanese electrolytic iron, ferro-manganese and graphite by melting and casting under vacuum. The top and the bottom of ingots of three inches diameter and twelve inches length, were cut off to remove the shrinkage pipe from the top and bottom slice and sent for chemical analysis. The analysis results were determined by Quantometer for

Mn and by Leco method for carbon and sulfur.

These ingots were machined to 2.875 inches diameter and one end was rounded in order to fit the extrusion chamber. Then they were heated to 1200 deg C under a controlled gas atmosphere and extruded to 0.75 inches. The top and the bottom of the extrusion bars were analysed for segregation of manganese and carbon. The difference in the content of alloying elements from the top to the bottom was found to be less than 0.02 wt %. These last analyses were taken to show the composition of alloys which were used in the experiments. These are shown in table 1. Also the composition of some specimens was checked after the unidirectional experimental work. Good agreement was found for both elements. The bars were hot rolled to .375 inches diameter.

The section was further reduced by cold swaging to .25 inches diameter. The materials showed no tendency to crack or to produce any other defect, although swaging the 0.8 % C steel was difficult because of the high carbon content.

Finally, the swaged specimens were cut into 100 mm lengths and then the surface was ground in a centerless grinder to 5.5 mm diameter. This procedure helped to remove all traces of decarburization at the surface. These materials were used in the steady-state growth apparatus, where an alumina tube of dimensions 6 mm I.D, 10 mm O.D. and 250 mm length was filled with it.

4.1.5 Specimen assembly

The specimen crucible was an open ended recrystallized alumina tube. One end of the tube was sealed with CC60 high purity alumina cement fired at 1200 C for 12 hours. Two of the 100 mm

long samples were loaded into the tube. A groove was made 0.5 mm below the top of each tube to hold 60 mm length of stainless steel wire around it. This wire was sealed with Autostick cement to the tube. The specimen assembly was suspended by a copper wire connected to the stainless steel wire, so that the heat extraction from the top of the crucible was reduced, instead of using a stainless steel sleeve as in previous work.

4.1.6 A typical run

The specimen was lowered into the furnace and the top and bottom of the furnace were sealed by a copper plate and a polythene seal, respectively. The copper wire was inserted through a hole on the copper plate and was connected to a copper weight. The function of this copper weight was to keep the wire straight in order to avoid any possibility of a gap between the specimen drive unit and the furnace, so that the speed of the motor can be assumed equal to the velocity of the specimen. Initially, the bottom of the specimen crucible is located 20 mm below the hot zone.

Before starting to heat up the furnace, the high purity argon gas was flushed into the system for about 20 min at 10 ft^3/h, so that oxygen in the furnace was removed. Then the power supply was switched on. The temperature was raised in four stages over two hours to reach around 1600 deg C. The power input at each stage was monitored from the generator and the final setting recorded, so that the furnace temperature could be calibrated.

When the constant hot zone was maintained, the specimen assembly was allowed to move vertically downwards and upwards

twice. This was done for two reasons: Firstly, to fill the specimen crucible completely with alloy and, secondly, to have a good contact between the thermocouple sheath and the alloy, so that the possibility of gas bubble appearance in the specimen crucible would be avoided and the temperature gradient would be consisent at a given power setting.

During the run, the flux of argon gas was reduced to 6 ft^3/h. This gas flux was kept constant throughout all the experimental work because it could change the temperature gradient. Before the final run, the bottom of the crucible was kept at the beginning of the hot zone for 10 min. The motor speed was reset at the required rate and the specimen was driven down for about 120 mm. Then the copper wire was cut in order to release the specimen assembly. The polythene seal was broken and the specimen was quickly quenched into ice cooled brine, immediately followed by stirring the solution with a copper bar to increase the efficiency of heat extraction. The crucible was usually cracked and only a small amount of liquid metal flowed through the cracks.

After this, the bottom of the furnace was closed and the gas flow rate was increased to protect the graphite susceptor from any more oxidation. The furnace was gradually cooled down for 1 hour to reduce the thermal shock to the furnace tube.

This procedure was repeated for all the specimens assuming that the specimens without the thermocouple cannot change the temperature gradient.

4.2 Sample examination

4.2.1 Sample preparation

Having removed the specimen from the alumina tube, it was macro-etched with 5 and 10 % HCl to identify the dendrite tips and the interface. A mark was put 2 mm in front of the interface to slice off the directionally solidified material from the completely liquid zone. This bar was cut to 30 mm long pieces because the holder of the electron probe micro analyser and the bakelite mounting press can allow a maximum length of sample equal to 30 mm. Each piece was mounted in conductive bakelite. Then the specimens were coarse-polished about the depth of 3 mm and fine diamond polished up to 0.25 micron. After etching with 4% picral, the interface and the fine dendritic structure were clearly revealed.

When the microprobe analyses were completed on the longitudinal sections, the specimens were cut transversely by the Servomet spark machine at different distances behind the tips. These were mounted and the growth morphology of the primary dendrite arms was examined.

4.2.2 Metallography

In an attempt to reveal the microstructure, four reagents were used. The macrostructure was examined by using the 10 and 5 % HCl acid to identify the interface. The dendrite arm morphology and the peritectic structure were revealed by using the 4 % picral and $K_2S_2O_5$ etch(151).

It was found that instead of etching with $K_2S_2O_5$ solution

directly after pre-etching with 4 % picral, we may etch with picral containing only a few drops $K_2S_2O_5$ solution which gives better segregation contrast. The colour of etch depended on etching time, carbon and manganese segregation and contents. Although the same colour could not be obtained, the liquid could be identified as bright colour between the dendrites.

The low carbon steels, especially less than 0.2 % C, showed some difficulties to etch, because the high diffusion in the delta ferrite reduced the segregation. Basically the same method was used to etch them with the highly concentrated $K_2S_2O_5$ and picral solution.

The etch depended on the efficiency of quenching, as well as on the highly segregated trace elements in the steel, such as phosphorus and sulfur. It may be noticed that the sulfur and phosphorus content of all the alloys were ten times less than the commercial limits. There was another difficulty in low carbon steels to get high contrast. And also it was the object to have almost MnS inclusion free steels.

4.2.3 Secondary arm spacing measurement

Two methods were used for measurement of secondary arms. In the first technique, the microscope of the Vickers microhardness equipment was used to measure the secondary dendrite arms as a function of distance from the solid-liquid interface. The stage is controlled by the micrometers and the magnification used was X 100, so that the error was minimized. If there was any error in the measurements, it arose from the sectioning of the specimen. But also this was overcome by measuring several dendrite arms in

But also this was overcome by measuring several dendrite arms in the same region.

The second method was that after taking the sequential photographs of the longitudinal section, and printing them, the secondary arm spacings were measured on the photographs. But this method was expensive in photographic materials and slow and depended on the contrast of the photographs. In some cases, this method was used.

The secondary arms were analysed with microprobe as a function of distance. From these analyses, the secondary arm size can be easily recognized due to segregation. These results were checked with the other method. A good agreement was seen between all these methods.

4.2.4 Primary arm spacing measurement

The transverse sections were prepared metallographically, photographed and printed. As Schwerdtfeger(46) described, two different primary arm spacings of the close packed arrangement were measured on the photographs. One primary arm spacing was the perpendicular distance between rows of aligned secondary arms and the other one was along the rows(figure 22). At least 20-30 spacings were measured to present the average arm spacing along the rows. But the number of measurements between the rows was less than that along the rows, because of the limited size of the specimen.

Several specimens were cut transversely as close as possible to the tips and at different distances, behind the tips. As shown in figures 32,35,36, the primary arm spacing and the size and

location of grains in the specimens remained constant during solidification. This may confirm that steady state conditions were very closely achieved during growth. Tertiary dendrite arms were not observed even at the beginning of the solidification in the specimens.

The primary arm spacings were usually measured in the interface region because the high contrast between the solid and the liquid phases helped to identify them clearly.

4.3 Electron probe microanalysis

4.3.1 Specimen preparation

Following metallographic examination of the specimen, regions were selected for microanalysis and marked by indentation with a micro-hardness tester. The specimens were repolished and analysed by electron probe microanalyser (EPMA) After scanning, specimens were re-etched with 4 % picral and photographed, so that the actual probe scan trace was shown up, due to the surface film of carbon deposited by the beam. The corrected concentration of manganese was compared with the probe trace and concentrations were related to the dendritic morphology.

Three different regions were selected for analysis

a) Secondary dendrite arms were analysed at different distances behind the tips on the longitudinal sections, so that the change in Cmin and Cmax of manganese was obtained during growth and these results were compared with a secondary arm coarsening computer program. Usually, four secondary arms were analysed and the average of the minimum and maximum of manganese concentration were taken to represent the region.

b) On the longitudinal section, highly segregated spots were observed in the last solidification regions. These points were analysed. But it was a problem to focus the electron beam on the spot of maximum concentration. In order to overcome this problem, several scan analyses were made over the spot after 2-3 microns intervals. The maximum of analysis was taken to represent the maximum manganese concentration of the spot.

c) the manganese concentration between primary arms was analysed along the long secondary arms on the transverse sections and perpendicular to the growth direction on the longitudinal section, after solidification had been completed. At the low carbon contents, the analyses were carried out on the longitudinal section, as well as on the transverse section, because the segregation between secondary arms disappeared.

The analyses results are shown in tables 5,6,7,8.

4.3.2 Operating Conditions

The typical conditions for analysis on the CAMBRIDGE MICROSCAN-5 instrument used in this work were :

Element	Counter	Crystal	Standard	Peak angle	Back Ground Ang.
Mn	Sealed	LiF	elec.-Mn	62.56	+-2
Fe	Sealed	LiF	elec.-Fe	57.29	+-2

Spectrometer take-off angle was 75 deg. The low voltage anode was used with acceleration voltage of 15 KV. Scan velocity was 10 micron/min. The mylar window was in the out position. The dead time correction was 3.2 micron sec for the sealed counter.

There are two kinds of error. One comes from counting statistics. When the typical count of 13500 (10 sec) for a standard specimen and of 250 (30 sec) for a specimen are obtained (using a counter voltage of 1640 V to get the 2 V pulse height analysis) then the standard deviation for manganese can be expressed as :

$$\sigma = \sqrt{N}$$

N counts obtained in time t

Taking the 95 % confidence limit, i.e. $2 \cdot \sigma$, the corresponding error for any one point is $\mp$ 0.02 % . The other error arises from ZAF correction procedure. As explained below, it is believed that it was very small.

4.3.3 Analysis procedure

Electron probe microanalysis was employed for quantitative determination of concentration. The following general procedure was used throughout this work. :

After vacuum was maintained in the system, the beam was turned on and the acceleration voltage was set to 15 KV. The electron beam was focussed on the Faraday cage. The spectrometer angles were set for electrolytic manganese and iron standard specimens and the counter rate was maximized by the counter supply voltage and the spectrometer angle.

For long analyses, the specimen current decreased gradually, so that the count rate could be dropped during the analysis. In order to avoid a change in the specimen current effecting the results, four standard measurements for peak and background were taken before

The counting interval was set at 30 sec and the scan velocity was 10 micron/min, so that each measurement presented the average concentration in a 5 micron distance along the scan. In the case of primary arm analysis, the time interval was 10 sec, so that after each two microns, one measurement was taken and this could provide that a very sharp peak of manganese segregation was detectable.

A scan speed of 10 micron/min and a chart speed of 10 mm/min were used, so that one mm on the chart corresponded to one micron on the specimen.

After the electron beam was focussed on the microhardness indentation at the low and high magnification with the back scattered electron image, the analysis was run through the center of secondary dendrite arms.

4.3.4 Concentration determination

X- ray intensity ratios were converted to weight percent of manganese by using the ZAF correction computer program, which is called Sheffield FRAME 3. This program was written by C. W. Haworth and J. Horsfield(152). After ZAF correction, it was found that there is very small effect of ZAF factor on the manganese concentration, because iron and manganese atomic numbers are 25 and 26 respectively. The atomic number, absorption and fluorescence correction effect of manganese on iron and vice versa are negligible at low concentrations of manganese, such as in the present work.(153) The typical calculated correction factors are as follows :

Z- Line	Z- Absorber	Mass Abs. Coeff.	F
25	25	78.50	0.9824
25	26	88.72	0.9824
26	25	62.71	0.9866
26	26	70.88	0.9866

After ZAF correction, the results were normalized to a hundred percentage.

4.3.5 Concentration map

Two specimens were selected for analysis by CAMEBAX - SX50 computerized microprobe at the British Steel Swinden Lab. The main advantage of this equipment is that it has five spectrometers, so that five different elements can be analysed simultaneously. But in the present work, only two of them were used for manganese and iron. In addition, selected regions could be examined and concentration of these regions could be plotted as a colour map. Each colour represents a range of manganese concentration, so that the concentration can be related to the morphology. In the present work, the concentration results of each specimen were plotted in two concentration ranges as shown in figures 80,81.

A LiF crystal and flow counter were used. The acceleration voltage was 15 KV and the probe current was 100 nA. 512 X 512 pixels were counted for 100 m sec on each pixel which is two microns, so that an 1.024 X 1.024 mm. area was analysed for 8 hours for each specimen. The results were plotted as a colour concentration map.

CHAPTER 5 COMPUTER MODELLING

5.1 Introduction

Although several attempts have been done to predict the microsegregation for primary and secondary dendrite arms quantitatively(74,89,90,91,92,98), the starting point of numerical modelling for binary system was proposed by Brody and Flemings(74) which is the basic model for later modification. Kirkwood and Evans(100) extended this model to the constant heat extraction case and they assumed that there is an equilibrium at the solid /liquid interface and the complete mixing of the solute in liquid. In addition to this, the diffusion coefficient was assumed to be constant during the freezing.

By using these assumptions, the rate of growth of the solid can be calculated from the equation below :

$$\frac{\partial f}{\partial T} = \frac{\left(\frac{\partial \Theta}{\partial x}\right)_f + \frac{(1-f)}{\gamma}}{\Theta_l(1-k_o) + (1-f)\frac{W}{\gamma}} \qquad 5.1$$

$$\Theta = \frac{C}{Co} \qquad T = \frac{D\,t}{l^2} \qquad W = \frac{L\,D}{S\,\alpha\,l^2} \qquad \gamma = \frac{Co\,\beta\,D}{\alpha\,l^2}$$

where

f: fraction of solid

D: diffusion coefficient

t: time

l: half of arm spacing

L: latent heat of solidification

Co: initial composition

β: slope of liquidus

α: cooling rate

x : distance from the plate centre

In this model, the moving boundary condition suggested by Crank(154) was used.

This approach was later modified by Ogilvy and Kirkwood(112) for dendrite arm coarsening situation. Ogilvy and Kirkwood(99,57,113) extended it to multicomponent systems with and without coarsening and containing fast diffusion element cases under constant cooling rate. Finally, Howe (114,115) extended this model for constant heat extraction situation including the peritectic reaction. In these models, planar solidification is assumed.

However, it is seen in this investigation and also in other works(101-104,155-158,73,47,46,44,39,28) that microsegregation is closely related to the detailed morphology of arms and the segregation between the primary arms may be higher than that of the secondaries, especially for dilute alloys. Under these circumstances, several primary arm models are proposed by applying the Ogilvy and Kirkwood model for different morphologies.

Flemings et al.(73) and recently some Japanese authors (92,102-104) have noticed the significant effect of morphology on the segregation. They suggested analytical and numerical models of primary arm solidification for the binary system. However, they did not specify the primary arm spacing which they used.

Basaran(112) has suggested a numerical calculation of back diffusion with dendrite coarsening, but the interface composition was computed with the modified form of Brody and Flemings' equation. In addition, the extra liquid volume at the composition

of the existing liquid was added to the unit element at each time step in his assumption. This procedure cannot conserve the solute in the element. Recently, Roosz et al.(116-119) proposed two models: One for secondary arms coarsening by applying the Ogilvy and Kirkwood mass balance suggestion and the other without coarsening but incomplete mixing in the liquid. However, they used the semi- empirical coarsening equation $\lambda_2 = K t^n$ to predict the secondary arm spacing, although the coarsening exponent and the initial arm spacing can vary from one alloy to another; for example, exponent n=0.22 for tool steels and n=0.5 for carbon steels. The theory(60) predicts that at the short time of solidification, there is a single relationship of the form $\lambda_2^3 \propto t$ i.e. $n = 0.33$. Therefore, the theoretical approach is still far from predicting the secondary arm spacing accurately and its use in the computer models is undesirable. (detail of models in chapter 2)

One point that should not be forgotten is that the TGZM effect is not taken into account in the coarsening models. It might have a significant influence at the high temperature gradient as observed in this project and other UDS work (57,47,44,156,159-161) and also in the cast ingots(162,163) and the continuous casting(164). By observing the secondary arms migration to dendrite tips under high temperature gradient during solidification, Allen and Hunt(64) suggested that this migration can cause melting of solid at the trailing edge of a secondary arm, where temperature is higher. By diluting the initial liquid, the new liquid resolidifies at a leading edge of secondary arms, where temperature is lower. This produces an asymmetric

microsegregation profile called 'saw tooth '. (detail in chapter-1)

Lalli (122) has proposed a numerical model for TGZM using Allen and Hunt's assumption.

5.2 Physical assumptions of the models

The first quantitative attempt to predict microsegregation came from Gulliver(89) and Scheil(90) and it is known as the Scheil equation. It is assumed that there is complete mixing in the liquid and the diffusion in the solid during solidification is neglected. Also, local thermodynamic equilibrium is maintained at the moving interface, described by a constant equilibrium partition coefficient. No undercooling is allowed for.

With the introduction of microprobe analysis, it was seen that the minimum concentration rises during freezing. Brody and Flemings (74) proposed an analytical equation which included the solid-state back diffusion during solidification. The other assumptions of the Scheil equation were kept the same.

It is known that the solidification is a dynamic process. During the freezing of metals, many parameters can change. The secondary arms coarsen, the diffusion decreases with temperature and the equilibrium coefficient can vary with composition. Therefore as Brody and Flemings suggested over twenty years ago, all these parameters can easily be changed by using the numerical techniques for partial differential equations. Also this technique allow us to modify the plate-like dendritic morphology to cylindrical and other morphological cases.

In this study, the partial differential form of Brody and Flemings's equation is used for the primary arm spacing model without varying their assumptions and by applying the moving boundary condition.

Ogilvy-Kirkwood(113) modified the Brody-Flemings's equation for the secondary arm coarsening case by going one step forward: They suggested that the secondary dendrite arm coarsens during solidification by ripening, so that the liquid composition is diluted by the remelting of this initial solid. This new mass balance is obtained by adding the term dL/dt*(Cl-Co) to the element. This dilution is responsible for a reduction in microsegregation. The other advantage of this model is that it considers the true back diffusion distance between secondary dendrite arms. Initially, the secondary arms are small and temperature is high; therefore, back diffusion distance is short and diffusion process is high. This reduces the microsegregation in addition to the ripening of secondary arms. This mechanism gradually becomes less effective with coarsening and temperature at the later stage of solidification. However, the model ignores the TGZM effect. This is the model used for microsegregation between the secondary arms in this project.

In the models, as Ogilvy(57) suggested, constant cooling rate is assumed for UDS experiments, whereas the constant heat extraction gives better agreement for the practical cast situation.

In addition to these, a temperature dependent diffusion(165) and constant partition coefficients for manganese and carbon are used in the calculation.(102) In the literature, a very small carbon effect on the manganese partition coefficient is

reported.(82,81)

5.3 Morphological assumptions of the models

Two of the biggest problems in predicting the microsegregation closely are the morphology of dendrite arms and the true representative back diffusion distance. By considering these effects, five microsegregation models are proposed. One of those models is for secondary dendrite arms with coarsening, whereas the others are for primary dendrite arms with the different morphology.

In the secondary dendrite arm model, it is assumed that the secondary dendrite arms are plate-like. This is an acceptable morphological assumption for carbon steels, because tertiary dendrite arms are not observed, as shown in this study. In the model, the unit element is taken to be between the centre line of a solid arm and the centre line of the liquid separating it from the adjacent arm. Apart from this model, tertiary dendrite arms are reported for highly alloyed steels, such as stainless steel, Hadfield steel(47), Fe-As-Cr alloys(79) and for Al-Cu alloys(156,69).

In the primary arm models, four dendritic morphologies are considered.

1) Cylindrical cellular primary arm model

2) Planar primary arm model

3) Cylindrical primary arm model

4) Concave solidification model (for spot segregation)

The cylindrical cellular primary arm model is developed for low carbon steels (less than 0.2 % C) at low growth rates

(1.5 mm/min and less). Under these conditions, the secondary dendrite arms are poorly-developed and later disappear as a result of high back-diffusion in the delta iron, as shown in figure 21. These primary dendrite arms without secondaries are considered cylindrical. Then, half of the primary arm spacing is taken to be equal to the radius of cylinder as a unit element. T.Matsumiya et al.(104) observed the same morphology under similar conditions for low carbon steels. They considered the primary arm as a hexagonal prism, instead of a cylinder. It is believed that these different models produce similar results. However, when these models are applied to the high cooling rates, the prediction of these models for maximum and minimum concentration of manganese is far from the experimental results. This difference arises from the unjustified assumption of dendrite morphology. In fact, the structure becomes well-developed dendritic when the growth rate (or cooling rate) increases.

Under these circumstances, planar and cylindrical primary dendrite arm models are proposed by considering the shortest diffusion path in the structure. In the close packed arrangement of primary arms, long and short , two kinds of secondary arms are observed, as shown figures 22. Mainly, the segregation took place between the long secondary arms. These long secondary arms are assumed cylindrical in the cylindrical model and planar in the planar model. The unit element is taken to be between the centre line of the long secondary arms and the edge of the secondary arms. This unit distance can be expressed as a L $=\lambda_2/4$ for both cases due to the symmetry, as it is schematically shown in figure 22.

On the longitudinal section, highly segregated spots are observed in the last solidification regions. These regions are between primary arms surrounded by three or four secondary arms, as shown schematically in figure 22. In the model, the unit area is taken by multiplying half of the primary arm spacing (λ_1') times the secondary dendrite arm spacing(λ_2). When this square area is assumed to be equal to the area of cross-section cylinder, the radius of this cylinder may represent the cell distance. The solidification starts from the edge of the cylinder and finishes at its centre, so that all the liquid is concentrated at a point, instead of spreading between secondary and primary dendrite arms. The model apparently over-predicts the maximum concentration of manganese. Modifying the morphology and using the two or three-dimensional back-diffusion models are needed to overcome this simplicity.

In the models, the back diffusion could be easily calculated between the solid/liquid interface and the centre of the dendrite. This back diffusion distance increases from zero to the total element length during solidification.

5.4 Computer modelling of primary arms

5.4.1 Basic model for binary system

The partial differential form of Brody - Flemings's equation can be rewritten as shown in figure-23

$$C_L(1-k_0^{\frac{1}{4}})\frac{\partial V_L}{\partial t} = k_0^{\frac{1}{4}} V_L \frac{\partial C_L}{\partial t} + (V_0 - V_L)\frac{\partial C_L}{\partial t} \qquad 5.2$$

where Vi volume of solid

Vo initial volume

Ai diffusion area of liquid/solid interface

It is known that

$$dV_i = A_i \, dX_i$$

Then using this relationship, equation (5.2) becomes

$$C_i(1-k_o^A) \frac{\partial X_i}{\partial t} = D \left(\frac{\partial C}{\partial x}\right)_{x_i} + \frac{(V_o - V_i)}{A_i} \frac{\partial C_i}{\partial t} \qquad 5.3$$

and

$$M = \frac{(V_o - V_i)}{A_i} \qquad 5.4$$

M depends on the shape and solidification direction. In the case of convex solidification

for planar $M = (L - X_i)$ 5.5

for cylindrical $M = \frac{(L^2 - X_i^2)}{2X_i}$ 5.6

for spherical $M = \frac{(L^3 - X_i^3)}{3X_i^2}$ 5.7

and in the case of concave solidification

for planar $M = (L - X_i)$ 5.8

for cylindrical $M = \frac{(L - X_i)}{2}$ 5.9

for spherical $$M = -\frac{(L - X_i)}{3} \qquad 5.10$$

where L half of dendrite spacing

Xi solidified distance

If cooling rate (W) and the liquidus slope (β) are assumed constant, then

$$W = \beta \left(-\frac{\partial C_l}{\partial t}\right) \qquad 5.11$$

where

$$W = \frac{\partial T}{\partial t} \qquad \text{and} \qquad \beta = -\frac{\partial T}{\partial C_l}$$

thus for planar solidification

$$\frac{\partial X_i}{\partial t} = \frac{D \left(\frac{\partial C}{\partial x}\right)_{x_i} + \frac{W}{\beta} (L - X_i)}{C_l (1 - k\delta)} \qquad 5.12$$

It can be applied for any case by changing the value of M

Equation (5.12) controls the movement of the interface and the new liquid composition can easily be calculated from (5.11) by knowing the time interval. The equilibrium is maintained at the interface and no undercooling is allowed for.

Crank(166) applied the Lagrangian interpolation formula for the moving boundary of the second Fick's equation. By using these numerical equations, the arrangement of node points at the interface position can be defined by r and p, where 1 < p < 2 so that (figure 24)

$$r = \frac{(r-1+P)}{n} \qquad X_i = \frac{(r-1+P)\lambda_i}{2n}$$

where $\frac{\lambda_i}{2n}$ node spacing

f fraction of solid

The composition gradient at the interface becomes

$$\left(\frac{\partial C}{\partial x}\right)_{x_i} = \left(\frac{2n}{\lambda_i}\right)\left\{ P\,\frac{C_{r-2}}{P+1} - \frac{P+1}{P} C_{r-1} + \frac{2P+1}{P(P+1)} C_x \right\} \quad 5.13$$

where

Cj solute concentration at node j

Cx solute concentration at interface

Back diffusion(167)

In the case of planar diffusion, the second Fick equation is

$$\frac{\partial C}{\partial t} = \frac{\partial^2 C}{\partial x^2} \quad 5.14$$

and it can be approximated by using the Taylor's expansion theorem :

$$C_r^* = C_r + \frac{D\,\delta t}{\left(\frac{\lambda_i}{2n}\right)^2}\left\{ C_{r+1} - 2C_r + C_{r-1} \right\} \quad 5.15$$

for $1 < r < r-2$

Where Cj is updated solute concentration at node j

When r=0, Equation (5.15) becomes

r=0

$$C_0^* = C_0 + \frac{2 D \delta t}{(\frac{\Delta r}{2n})^2} \left\{ C_1 - C_0 \right\} \qquad 5.16$$

Due to the surface boundary conditions, the equation (5.15) becomes

r=n

$$C_n^* = C_n + \frac{2 D \delta t}{(\frac{\Delta r}{2n})^2} \left\{ C_{n-1} - C_n \right\} \qquad 5.17$$

For radial diffusion, the second equation of Fick

$$\frac{\partial C}{\partial t} = D \left(\frac{\partial^2 C}{\partial r^2} + \frac{\partial C}{r \partial r} \right) \qquad 5.18$$

in the finite approximation form

for $1 < r < r-2$

$$C_r^* = C_r + \frac{D \delta t}{(2r)(\frac{\Delta r}{2n})^2} \left\{ (2r+1) C_{r-1} - 4r C_r + (2r-1) C_{r-1} \right\} \qquad 5.19$$

for r=0 in the center

$$C_0^* = C_0 + \frac{4 D \delta t}{(\frac{\Delta r}{2n})^2} \left\{ C_1 - C_0 \right\} \qquad 5.20$$

for r=n at the surface

$$C_n^* = C_n + \frac{2 D \delta t}{(\frac{\Delta r}{2n})^2} \left\{ C_{n-1} - C_n \right\} \qquad 5.21$$

and Cr-1 concentration for any case

$$C_{r-1}^* = C_{r-2}^* + \frac{2 D \delta t}{(\frac{\Delta r}{2n})^2} \left\{ \frac{C_{r-2}}{P+1} + \frac{C_{r-1}}{P} + \frac{C_x}{P(P+1)} \right\} \qquad 5.22$$

and the three point lagrangian interpolation formula for Cr

$$C_r^* = C_{r-2}^* \frac{(1-P^*)}{(1+P^*)} + 2\,C_{r-1}\frac{(P^*-1)}{P^*} + P^*\frac{2\,C_x^*}{(P^*+1)} \qquad 5.23$$

The new solid interface concentration Cx is calculated from the new liquid at each stage using the equilibrium partition coefficient.

To keep the system stable, it should be

$$\frac{D\,\delta t}{\left(\frac{\lambda}{2n}\right)^2} \leq \frac{1}{2} \qquad 5.24$$

In the computer programs , we choose it 1/4 in order to ensure that the back diffusion calculations remain stable in the centre. In addition, the number of divisions is chosen as n=100 or 200 in order to obtain the small node spacing, and therefore, to maintain the mass balance in the system as close as possible to 100 percent.

At the beginning of the program, the first three nodes must be calculated with the Scheil equation, in order to proceed to the finite difference calculation. For fast diffusion elements, the lever rule is used.

5.4.2 Basic model for fast diffusion element

By using Ogilvy and Kirkwood' suggestion for a fast diffusion element, it is assumed that the system is at equilibrium with complete mixing in solid and liquid. Then equation(5.2) can be rewritten

$$C_L\,(1-k_o^1)\frac{\partial V_L}{\partial t} = k_o^1\,V_o\frac{\partial C_L}{\partial t} + (V_o-V_L)\frac{\partial C_L}{\partial t} \qquad 5.25$$

and therefore

$$C_L(1-k_o^1)\frac{\partial V_L}{\partial t} = \left\{ V_o + V_L(k_o^1-1) \right\}\frac{\partial C_L}{\partial t} \qquad 5.26$$

This can be used in the Fe- C system for carbon.

5.4.3 Ternary system containing fast diffusion solute element

In order to solve the microsegregation problem in steels, both these systems should be combined to determine the movement of interface, by assuming there is no interaction between elements, therefore

$$\beta_1 \qquad C_L(1-k_o^1)\left(\frac{\partial V_L}{\partial t}\right)_1 = k_o^1\,V_L\frac{\partial C_L}{\partial t} + (V_o-V_L)\frac{\partial C_L}{\partial t} \qquad 5.27$$

$$\beta_2 \qquad B_L(1-k_o^2)\left(\frac{\partial V_L}{\partial t}\right)_2 = A_L D\left(\frac{\partial B}{\partial x}\right)_{x_L} + (V_o-V_L)\frac{\partial B_L}{\partial t} \qquad 5.28$$

If the cooling rate and the liquidus slope are assumed to be constant, then

$$W = \left(\frac{\partial C_L}{\partial t}\right)_{\beta_1} + \left(\frac{\partial B_L}{\partial t}\right)_{\beta_2} \qquad 5.29$$

where

$$\beta_1 = \frac{\partial T}{\partial C_1} \qquad \text{and} \qquad \beta_2 = \frac{\partial T}{\partial C_1}$$

If we multiply equation (5.27) by β_1 and multiply equation (5.28) by β_2 and then add them to eliminate dC/dt , we get,

as

$$\left(\frac{\partial V_1}{\partial t}\right)_1 = \left(\frac{\partial V_1}{\partial t}\right)_2$$

$$\frac{\partial V_1}{\partial t} = \frac{A_1\beta_2\left(\frac{\partial B}{\partial x}\right)_{x1} + (V_0 - V_1)W}{C_1(1-k_0^1)\beta_1 Z + B_1(1-k_0^2)\beta_2} \qquad 5.30$$

where $Z = \dfrac{1 - f}{(1 - (1-k_0^1)f)}$ f : fraction of solid

Initially dCl and the time interval are known and therefore the movement of interface can be calculated from equation.(5.30) By knowing this movement, the increase of the liquid concentration for each element can be obtained from equation (5.27) and (5.28). By adding this to the initial liquid, the new liquid concentration and the new solid concentration can easily be calculated by using the equilibrium coefficient.

The main equation (5.30) may change for each shape and case of solidification.

planar model:

$$\frac{\partial X_t}{\partial t} = \frac{A_t \beta_2 \left(\frac{\partial B}{\partial x}\right)_{x_t} + (L - X_t) W}{C_t (1 - k\delta_1)\beta_1 Z + B_t (1 - k\delta_2)\beta_2} \qquad 5.31$$

convex cylindrical model :

$$\frac{\partial X_t}{\partial t} = \frac{A_t \beta_2 \left(\frac{\partial B}{\partial x}\right)_{x_t} + (L^2 - X_t^2) W}{C_t (1 - k\delta_1)\beta_1 Z + B_t (1 - k\delta_2)\beta_2} \qquad 5.32$$

concave cylindrical model :

$$\frac{\partial X}{\partial t} = \frac{A_t \beta_2 \left(\frac{\partial B}{\partial x}\right)_{x_t} + (L - X_t)^2 W}{C_t (1 - k\delta_1)\beta_1 Z + B_t (1 - k\delta_2)\beta_2} \qquad 5.33$$

The back diffusion calculation is only needed for substitutional elements, because fast diffusing elements assumed to be completely mixed in both phases.

5.5 Computer modelling of secondary arms

5.5.1 Planar coarsening model for binary system

In this model, it is assumed that the secondary arm spacing increases by increasing the length of the melt pool at the same time, with remelting other side arms somewhere in the system. By taking the centre of solid to the centre of liquid as the element spacing, the mass balance can be written similarly to the Brody-Flemings equation with adding extra volume to liquid with original concentration, Co. This assumption is required to conserve

solute in the system. Therefore the mass balance is (figure 25)

Area a = Area b + Area c + Area d

$$Ct(1-ko)\frac{\partial X_t}{\partial t} = D\left(\frac{\partial C}{\partial t}\right)_{xt} + \left(\frac{\lambda 2}{2} - X_t\right)\frac{\partial Ct}{\partial t} + (Ct-Co)\frac{\partial \lambda 2/2}{\partial t} \qquad 5.34$$

It is well known that the secondary arm coarsening can be presented by this equation

$$\lambda 2 = K\, t^n \qquad 5.35$$

Where n coarsening exponent

K experimentally found constant

then

$$\frac{\partial \lambda 2}{\partial t} = n\, K\, t^{n-1} \qquad \text{or} \qquad \frac{\partial \lambda 2/2}{\partial t} = \frac{n}{2}\, K\, t^{n-1} \qquad 5.36$$

By using the constant cooling rate and liquidus slope, as assumed before, the movement of interface is

$$\frac{\partial X_t}{\partial t} = \frac{D\left(\frac{\partial C}{\partial x}\right)_{xt} + \frac{W}{\beta}\left(\frac{\lambda 2}{2} - X_t\right) + \frac{1}{2}(Ct-Co)nK\, t^{n-1}}{Ct(1-ko)} \qquad 5.37$$

This model increases the back diffusion, initially choosing the small arm spacing and allowing it to thicken during the freezing. The extra term, by diluting the liquid, decreases the

segregation. The segregation does not vary practically with solidification time or cooling rate.

5.5.2 Planar coarsening model containing a fast diffusion solute element for ternary system

In the case of fast diffusion solute element such as carbon in steel, the interface equation can be written

$$C_L(1-k_C^1)\frac{\partial X_L}{\partial t} = k_C^1 X_L \frac{\partial C_L}{\partial t} + \left(\frac{\lambda_2}{2} - X_L\right)\frac{\partial C_L}{\partial t} + (C_L - C_o)\frac{\partial \lambda_2/2}{\partial t} \qquad 5.38$$

and for substitutional solute element

$$B_L(1-k_B^2)\frac{\partial X_L}{\partial t} = D\left(\frac{\partial B}{\partial x}\right)_{x_L} + \left(\frac{\lambda_2}{2} - X_L\right)\frac{\partial B_L}{\partial t} + (B_L - B_o)\frac{\partial \lambda_2/2}{\partial t} \qquad 5.39$$

By multiplying two equations by β_1 and β_2 respectively and by adding them to eliminate dC/dt, we get

$$\frac{\partial X_L}{\partial t} = \frac{\beta_2 D\left(\frac{\partial B}{\partial x}\right)_{x_L} + W\left(\frac{\lambda_2}{2} - X_L\right) + \left\{\beta_1(C_L - C_o) + \beta_2(B_L - B_o)\right\}\frac{\partial \lambda_2/2}{\partial t}}{C_L(1-k_C^1)\beta_1 2 + B_L(1-k_B^2)\beta_2} \qquad 5.40$$

Then the precedure is the same as in the primary models.

The computer programs are given in appendix-1. The results are compared with the experimental results and discussed in the next two chapters.

CHAPTER 6 EXPERIMENTAL RESULTS

6.1 Temperature gradient measurements

Having obtained a constant temperature in the furnace, a dummy assembly was moved down and the thermal history was plotted on the servoscribe with 2 mV full scale deflection, using backing off facilities. A discontinuity of the slope of the curve showed the thermal arrest. The average temperature gradients were calculated in the liquid region ahead of the solid-liquid interface (Gl), in the liquid + solid region (Gl+s) and in the solid (Gs). It was assumed that these conditions were always achieved in all specimens without a thermocouple. Therefore the gradients could not be precisely determined in each specimen.

The 0.8 % C specimens were used to determine the temperature gradients under different traverse speeds and induction coil designs. This alloy has the largest solidification range in the experimental alloy series; therefore the phase transformation can be easily recognized. A 0.1 % C alloy was used to check the effect of carbon content on the temperature gradients. It is found that the carbon composition changes did not show a large influence on the temperature gradients. It is interesting that undercooling was observed below the peritectic temperature under all traverse speeds in one 0.1 % C specimen. In the literature, this has been seen at low carbon steels in cast ingots(157,168), but not in the unidirectional experiments. However, when this experiment was repeated with another 0.1 % C specimen, this undercooling could not be seen. Probably, in the previous

specimen, there were some gas gaps which the liquid metal filled at the later stage because of high gas pressure. This could cause an increase of the temperature around the tip of the thermocouple.

The three different induction coils were used to obtain the various temperature gradients. The recorded power inputs were calibrated as series-1, 1.9 KW, series-2, 2.2 KW and series-3, 2.4 KW. Each of the three series of experimentals was carried out over a short period of time without changing the construction of the furnace to minimize changes in the system from the burning of the graphite susceptor.

The calculated temperature gradients and cooling rates are shown on table 2 for each series and speeds. When the traverse speed (growth rate) is increased in a series, the temperature gradients is reduced.

6.2 Metallography and morphology of dendrite arms

A $K_2 S_2O_5$ - Picral colour etch was mostly used to reveal the microstructure since it is very sensitive to composition. The morphology of primary and secondary arms was studied both on the longitudinal and the transverse sections.

The 0.8 % C sample, grown at the lowest growth rate (1.5 mm/min) with a temperature gradient of 8.4 °C/mm in liquid, is shown in figure 26. The quenching was so efficient, that liquid solidified as dendritic up to 3 mm behind the dendrite tips between the primary arms and the microsegregation remained. At the beginning of solidification, manganese and highly segregated carbon caused blueish and reddish colour difference. This colour

contrast increased as a result of segregation at the end of solidification and the bright blue indicated highly segregated liquid between the primary arms. This structure can be explained as a result of coalescence, as Young(42) observed the same structure on Al-Cu alloys. Moving away from the tips into the solid, the secondary arm spacing increased by the process of coarsening. During solidification the secondary arms thickened and rejected the concentrated liquid into spacing between the primary arms, simultaneously. The secondary arm tips eventually touched and coalesced, leaving a highly segregated liquid. This liquid shrank and spheroidised with further cooling(figure 27). As a result of the coalescence process, secondary arms joined each other and completely disappeared at the end of solidification. This solidification mechanism was always found at all the lowest growth rates for all carbon contents and all temperature gradients.

The coalescence process was observed also at the higher growth rates but as a result of high cooling rate, the secondary arms did not entirely disappear at the end of solidification for all carbon contents, except 0.1 % C. The longitudinal sections of 0.8 % C, grown at the rate of 6 mm/min and 15 mm/min, are shown in figures 28 and 29, respectively. In these microphotographs, the bright colours indicated highly segregated liquid between the primary arms as a result of rejected liquid.

In the case of 0.1 % C, the same coalescence process was seen. A typical example of 0.1 % C, grown at 6 mm/min with a temperature gradient of 7.2 °C/mm in liquid, is shown in figures 30

and 6 at different magnifications. Highly segregated liquid remained between the primary arms. As observed in the 0.8 % C specimen, the liquid between the primary arms surrounded by secondaries tended to spheroidise. These regions appeared as yellow spots in figure 31. The secondary arms disappeared completely at the end of solidification, even at the high growth rates, due to the high back diffusion in the delta ferrite and to the poorly developed secondaries.

It is generally found that the process of coalescence is so effective in removing the interdendritic liquid regions between the secondary dendrite arms, that reliable estimates of the final spacing were made more difficult, especially at the low carbon content.

After the secondary arm morphology and spacing had been studied and measured on the longitudinal sections, these specimens were cut in order to investigate the transverse section of the primary arms. Some specimens were chosen to be cut at different distances from the dendrite tips, in order to observe the development of secondaries from the primary arm morphology during solidification.

Mainly two different morphologies were observed:

a) planar flanges(pf)-with a cross section in the form of a plus sign

b) circular flanges(cf)-with a cross section in the form of a four-leaved clover

Typical examples of the approximately circularly developed flanges are shown in figure 32 for 0.8 % C grown at 1.5 mm/min at various distances from the dendrite tips and in figures 33 and 34 for 0.1 % C and 0.2 % C grown at 1.5 mm/min, respectively. As

seen in figure 32, at the beginning of solidification, secondary arms grow from the primary stalks initially in the form of approximately circular flanges (figure 32-a-b). During the course of solidification, secondary arms started to coarsen and became more circular(figures 32-c-d). As dendrites collide with each other, there will be no more growth as indicated in figure 32-e. However, solute rich liquid still remains between the primary arms surrounded by secondaries. Finally, these regions solidify, leaving randomly distributed high segregation points between the primary arms. This morphology was seen at the lowest growth rate(1.5 mm/min) for all conditions and carbon contents(figures 32,33 and 34).

At the high growth rates, the dendrite morphology seems to be different from the lowest growth rates. Typical examples are shown in figures 35 and 36 for 0.8 % C grown at 6 mm/min and 15 mm/min, respectively. As seen in these figures, the secondary arms develop as planar flanges. This may cause a more uniformly distributed segregation pattern at the end of solidification: therefore it requires different computer modelling.

One thing that both morphologies have in common, is that the highest possible segregation will tend to take place in the interdendritic zone between the primary arms.

It may be noticed in figures 32 to 36 that many primary arms grow mainly in the so-called 'close-packed' arrangement(interlocking). Jacobi and Schwerdtfeger(46) defined two, even in some cases three, primary arm spacings in the close packed structure. In

fact, the third was a slightly different orientation of the second primary arm spacing. That is why,in this study, two primary arm spacings are usually defined and measured(figure 22). It is also found that the secondary arm length along the array direction is shorter than the secondary arm length which grow normal to the array direction(figure 37). The same morphology was observed by Jacobi and Schwerdtfeger(46) in carbon steels.

Higher order arms, such as tertiary dendrites or cells, were not observed even at the beginning of solidification as some investigators have recorded in similar alloy systems(44,46). The figures 32,35 and 36 are also proof that primary arm spacings do not change with distance during solidification.

It is generally found that the morphology of the primary arms changed with decreasing carbon content, so that the primary dendrite core became more pronounced and the secondary arms became less well developed.

6.2.1 Peritectic transformation

The peritectic reaction has not been investigated in detail in carbon steel, owing to the difficulty in retaining the solidification structure by rapid quenching, due to the high diffusivity of carbon. However, some evidence of this transformation were observed in this study, although the delta ferrite was not seen directly in the microstructure.

A 0.1 % C specimen, grown at the rate of 6 mm/min with a temperature gradient of 7.2 C/mm, was cut at various distances from the dendrite tips and these transverse sections were colour-etched as seen in figure 38. At approximately 1495 C, the specimen was in the liquid + delta region(figure 38-a). When the

temperature dropped to around 1440 C, the specimen completely solidified, but it was still in the delta ferrite-austenite region(figure 38-b). Then the delta ferrite transformed to austenite with further cooling(figure 38-c).

It is believed that when this specimen was quenched quickly enough, both phases produced different martensitic structures due to the difference of carbon solubility between the delta ferrite and austenite. It can be seen from figure 38 that carbon tended to diffuse into the centre of the primary arms which initially solidified as delta ferrite. This could cause an orientation of martensite such that the needles point into the centre of primary arms(figure 38-b). The similar delta ferrite-austenite phase transformation can be seen in figures 33 and 34. The white regions in the centre of the primary arms indicated the delta ferrite, whereas the colour regions indicated the austenite.

As a consequence of this metallographic evidence, it can be suggested that the peritectic reaction was initiated by the nucleation of the austenite on initially solidified delta ferrite dendrites. Then this austenite grew around delta ferrite and isolated it from contact with the liquid. The thickening rate of austenite could be controlled by the diffusion of carbon through the two-phase boundary in the manganese steels.

6.2.2 Primary arm spacing

Two different primary arm spacings were measured on the transverse sections of the specimens in the liquid-solid region which had been colour-etched. These are presented in table 3.

In figure 39, the primary arm spacings are plotted against the temperature gradient in liquid (G1) on log-log scale for different growth rates and carbon contents. It is clear that the primary arm spacing decreased with increasing the temperature gradient in liquid and with increasing the growth rate.

These data were used to obtain the exponent and the constant of equation 6.1 which defines the primary arm spacing as a function of the growth rate (V) and the temperature gradient in liquid(G1).

$$\lambda_1 = A \; G^{-n} \; V^{-m} \qquad 6.1$$

Where A, m, n are constants

In some cases, there are only two data points which cannot allow good accuracy. For this reason, the calculation has been done only where three data points are available. It is generally found that n is 0.5+-0.1.

It was difficult to obtain the same temperature gradient at different growth rates; therefore the data were taken from the straight lines in figure 39-d. These data are plotted against growth rate at the temperature gradient of 5.5 °C/mm and 8 °C/mm in figure 40. Some data near these temperature gradients were also included in this figure. m is easily calculated from figure 40 and found 0.40+-0.1.

These values are not far from the theoretical predictions of the growth rate exponent, m=1/4, and the temperature gradient exponent, n=1/2. Jacobi and Schwerdtfeger (46) reported these exponents for manganese steels as the same as the theoretical

prediction.

The present experimental results and those available in the literature are plotted as a function of $G^{1/2} V^{1/4}$ to compare with five current models for primary arm spacing in Fe-C binary alloys. As shown in figure 41, a very good correlation is found among four low alloyed carbon steels(43,44,46,48) and the present work. It can be seen that the prediction of the Hunt equation(36) underestimates the true values, whereas Kurz-Fisher equation(31) Laxmanan's minimum undercooling and stability equation(32,33,27) and the Trivedi equation(28) seriously overestimate it. However, Hunt's equation fits at the high cooling rates. One point that should be remembered is that all these data were compared in the case of 0.8 % C, although the carbon content of two specimens is higher than 0.8 % C; the other two are lower and all these theoretical approaches are strictly valid only for binary alloys.

The present data are also plotted against carbon content and as a function of temperature gradient in the liquid for each growth rate as shown in figure 42. It is seen that primary arm spacing is increased with carbon content. But this tendency is not very obvious at the high temperature gradients.

When the present data are compared with Hunt's equation for the 0.1 % C and 0.8 % C cases as a function of $G^{1/2} V^{1/4}$ in figure 43, it is found that the carbon effect on the primary arm spacing is not as much as estimated from the equation.

6.2.3 Secondary arm spacing

The secondary arm spacing was measured on the longitudinal

section of specimens. Each point was calculated by averaging over 6-10 consecutive side arms and then the distance from the dendrite tips was converted to solidification time.

At low carbon contents, side arms could not be measured very effectively because high diffusion, low solidification range and high coarsening rates produced difficulties in obtaining values with accuracy.

These values are plotted against the solidification time on a log-log scale in figures 44 to 53 for each carbon content and each power input series. Using the least square method, the constants of the coarsening equation were calculated for each specimen, although this technique needs a large number of values to obtain a good relationship. The calculated constants of coarsening equation are shown in table 4. It can be seen that there is a good agreement between the literature and the present results which are changed in the range of n=0.35 to 0.55. If we ignore extreme cases, most of the data are between 0.40 and 0.50. Jacobi(168) reported the same kind of variation in similar alloys. This coarsening rate may be the highest one in all known metallic alloy groups: for example, by comparison, for tool steel n=0.24(57) and for Al-Cu alloys n=0.32(42).

Generally, it is found that the pre-exponential secondary arm spacing constant(A) in equation $\lambda_2 = A t^n$ increases with decreasing carbon content and with decreasing temperature gradient in the liquid. The secondary arm spacings are reduced with increasing cooling rates.

6.3 Microsegregation results

In the attempt to follow the process of manganese segregation during solidification, specimens were sectioned longitudinally and transversely at different distances behind the dendrite tips. The distribution of manganese was analysed systematically between the secondary arms and between the primary arms. Figure 54 shows typical chosen analysed lines at different distances, behind the dendrite tips on the longitudinal section.

Specimens were analysed by electron microprobe. Within the accuracy of microprobe measurements, results are presented in table 5 for 0.1 % C, table 6 for 0.2 % C, table 7 for 0.4 % C and table 8 for 0.8 % C. In these tables, the minimum(Cmin) and maximum(Cmax) of the manganese concentrations are shown for the primary and the secondary arms separately, as a function of distance behind the dendrite tips.

6.3.1 Microsegregation of manganese between secondary arms

6.3.1.1 Change in Cmin during growth and the effect of carbon content

The changes in Cmin during growth are plotted in figure 55 to 63 as a function of temperature below the liquidus for each carbon content.

Although poorly developed side arms were rarely measured and analysed for 0.1 % C, it can be seen from figure 55 that back diffusion is very fast, because of high diffusion in delta ferrite. The initial composition at around 5 C below the liquidus is about 1.35 % Mn and this rises to 1.55 % Mn near the end of

solidification, where the side arms disappear. Although the clear effect of growth rate cannot be seen, there is a tendency in the figure to increase Cmin by decreasing the growth rate.

The 0.2 % C alloy solidifies partly as delta ferrite. As shown in figure 56, the same high back diffusion in delta ferrite up to the peritectic temperature(around 20 C below the liquidus) is observed; then the increase in Cmin becomes marginal because of austenite formation. Cmin tends to be in the range of 1.41 to 1.44 % Mn at the end of solidification at the high growth rates. However, at the lowest growth rate, Cmin continuously rises up to around 1.50 % Mn.

Cmin are plotted as a function of temperature below the liquidus for different temperature gradients in figures 57 and 58, in order to see the effect of temperature gradient on Cmin at the growth rates of 6 mm/min and 30 mm/min. It is found that the temperature gradient effect on Cmin at the end of solidification is small at the rate of 30 mm/min, but this effect at the growth rate of 6 mm/min shows a large variation in Cmin. However, Cmin tends to rise up to 1.42 % Mn.

At about 0.40 % C, the 1.6 % Mn steel solidifies as austenite. Therefore Cmin of 0.8 % C and 0.4 % C alloys behaves in a completely different manner to the other two alloys. It can be seen from figures 59 and 60 that the initial composition is around 1.25 % Mn and then it tends to increase up to 1.32. This increase in Cmin was also observed in 1 % C- 1.4 % Cr - Fe steel by Rickinson(44) in primary cores. However, again the lowest growth rate behaves completely different to the higher growth rates and the Cmin rises up to 1.4 % Mn. The structure becomes

nondendritic at the end of solidification. For high carbon contents and growth rates, the effect of temperature gradient on Cmin seems to be small, as shown in figures 61 and 62.

The specimens, grown at 6 mm/min for different carbon contents are compared in figure 63. It can be seen that carbon content plays a significant role in back diffusion. However, diffusion may not be the only process to cause an increase in Cmin, but coarsening and TGZM may also have an big effect.

Although it will be discussed in detail, it can be said as a consequence of these figures, that at the low carbon contents, diffusion is so dominant, that the other two processes are negligible. But at high carbon contents, they all combine together to increase Cmin.

6.3.1.2 Segregation ratio and the effect of carbon content

The changes in Cmax during solidification are shown in figure 64 for some specimens. The Cmax of manganese between secondary arms increases up to 70-80 C below liquidus and then starts to decrease to the level of 1.95 in 0.8 % C due to the back diffusion and nearly the same values are obtained for 0.4 % C. The Cmax concentration at the end of solidification is found to be less for 0.2 % C, being about 1.74 % Mn and there is no clear data obtained for 0.1 % C. These Cmax around 1200 C are plotted as a function of cooling rate for 0.8 % C and 0.4 % C in figure 65 at the same time showing Cmin of them. The Cmax does not change with cooling rate. This can be explained by the coalescence process, in that during freezing, highly concentrated

liquid between the secondaries was expelled to the region between the primaries and segregation mainly occurred there, rather than between the secondary arms. This process seems to be independent of cooling rate.

From these Cmax and Cmin data, the segregation ratios between the secondary dendrite arms are calculated and plotted in figure 66 as a function of cooling rate. It can be seen that there is practically no effect of cooling rate on the segregation ratio of manganese. But the segregation ratio increases with carbon content from 1.02 for 0.1 % C to 1.5 for 0.8 % C at around 1200 deg C. However, the segregation ratios between the secondary arms are found to be less than the segregation ratios between the primary arms.

6.3.1.3 TGZM effect

Saw-tooth profiles were observed throughout this study. This can be explained with the temperature gradient zone melting (TGZM) effect.

As mentioned before, the migrated secondary arm distance is given by an equation due to Hunt and Allen(65).

$$d \cong \frac{D_l}{V(1-k_o)} \ln\left(\frac{C_2}{C_1}\right)$$

where D_l is the diffusion coefficient in liquid

V is tip growth rate

C_1 and C_2 are values of C_l in liquid pool at the beginning and end of solidification, respectively

In this equation, there is only one variable which is the growth

rate for a given alloy. It is assumed that the growth rate does not change the segregation much between the secondary arms, which is most likely true, then the migration distances in the secondary arms at the end of freezing were calculated by using the following data and plotted in figure 67.

$D_l = 7*10^{-2}$ mm^2/sec (171)

C2 and C1 2.70 and 1.65 % Mn, respectively

Kmn = 0.78 for austenite

V = 1.5 to 30 mm/min in this study

It can be seen that at the lowest growth rate(1.5 mm/min) the migration distance is about 60 microns and it decreases with increasing growth rate; for example it is 3 microns at 30 mm/min. Considering that the largest side arm was 120 microns at the 1.5 mm/min for 0.8 % C, it can be said that half of the secondary arms are replaced during growth. This results in significant homogenization, which can be one of the reasons for the disappearence of side arms at the end of freezing for the lowest growth rate. But suprisingly, as shown in figure 68, saw tooth profiles could not be observed under this condition. However, the enormous rise in Cmin can be seen. All these could indicate that although there was very high migration and diffusion during growth, at the same time, highly enriched liquid was removed between the primary dendrite arms by the coalescence process, to reduce the segregation.

In figure 68-e, the solute profile between the primary dendrite arms is shown. The segregation only remained between the primary arms at the end of solidification.

At the high velocities, the saw-tooth profiles were observed as expected. For each growth rate, a series of examples during growth are given in figures 69,70 and 71 for 0.8 % C.

As shown in figure 69-a at the growth rate of 6 mm/min, initially the secondary arms grew symmetrically about 3.2 mm behind tips, after which they solidified only on one side of the surface of side arms towards the tips. The leading edge can be recognized by a sharp peak in concentration. During the growth, side arms thickened and the solid concentration at the peak increased, simultaneously. At 90 C below the liquidus, Cmin reached 1.30 % Mn while Cmax in liquid was around 2 % Mn. This high peak at the leading edge diffused slightly to the back edge of the front secondary arm under a high concentration gradient at the end of solidification. But there was an exception in figure 69-e. This peak at the leading edge was not sharp and short as much as at the beginning. It is believed that this relatively long peak was a result of coalescence of two secondary dendrite arms.

The TGZM was observed at the higher growth rates, such as 15 and 30 mm/min as shown in figures 70 and 71, respectively. Although migration distances were very short, e.g. less than 6 microns under these conditions, at the same time, dendrite arm spacing was also small, resulting in the same compositional history for them. The final manganese concentration of Cmin and Cmax for them at the end of growth is around 1.30 and 1.90 % Mn.

It may be noticed in figures 69,70 and 71 that there is a large variation of Cmin and especially Cmax in side arms. These indicated that the coalescence process of each individual side

arm was different than other arms. The nearly joined secondary arms are marked in figures 69,70 and 71 with an arrow. Also there were sectioning problems in the specimens. These may cause some variation in the Cmax and Cmin, as well. Each section of secondary arms may produce different Cmax, due to the nature of secondary arm morphology. Rickinson(44) and Fredriksson et al.(162) analysed several consecutive secondary dendrite arms with a distance interval and they found that each analysed line produced a different concentration variation and Cmax increased as the region between the primary arms was approached, which were the last points to solidify.

The TGZM effect has been seen in many alloy systems; using unidirectional technique, in Cr steel by Rickinson(44), in Al-Cu alloys by Young(156) and Rickinson(44), in Hadfield steel Schwerdtfeger at al.(47), in stainless steels by Eruslu(159) and El-Nayal(160) and tool steel by Ogilvy(57). Also Fredriksson at al.(164,162) observed TGZM in cast Cr steel ingots and in continueus casting of carbon steels, and E. Schurmann at al.(163) in low alloyed Mn,Mo,Cr cast steel ingot. However, most of the workers did not report the effect of TGZM, although it can be easily recognized in the figures provided.

6.3.2 Microsegregation of manganese between primary arms

The solute concentration between primary arms was analysed on the longitudinal and transverse sections well after the solidification had been completed, when the solid state diffusion had become negligible(figure 95).

6.3.2.1 Change in Cmin during growth and the effect of carbon

The low carbon steels solidify initially as delta ferrite where diffusion coefficient is 42 times higher than for austenite. In this phase region, the change in Cmin during growth is found to be the significantly important parameter for segregation ratio. As shown in figure 72, Cmin increases from 1.36 % Mn to 1.45 % Mn for 0.1 % C and to 1.41 % Mn for 0.2 % C between the primary dendrite arms. This difference may be explained by the percentage of delta ferrite present at the end of solidification, which is almost 100 % for 0.1 % C and 75 % for 0.2 % C. At the high carbon contents, the analysis has been done along the long secondary arms in the close packed arrangement, rather than in the core of the primary dendrite arms because of the small cores. The values are found same as the secondary arms and the Cmin increases from 1.25 to around 1.32 % Mn. (figure 59 and 60)

The Cmin for all carbon contents are plotted as a function of cooling rate as shown in figure 73 corresponding to around 1200 deg C. It may be seen that Cmin between the primary arms increases with carbon content but the cooling rate does not alter it, given the accuracy of measurement.

6.3.2.2 Segregation ratio and the effect of carbon

The maximum concentrations between the primary arms on transverse sections along the long secondary arms were analysed and the results are given in tables 5 to 8. For each specimen, a large variation in Cmax was found, because of the various

geometries developed in the primary interdendritic regions resulting from the way that secondary arms from adjacent primaries impinged on one another.

This large variation in Cmax for each carbon content is shown in figures 74,75,76 and 77 as a function of cooling rate. If either the maximum of Cmax or average of them for each specimen is taken as the maximum, it can be seen that Cmax tends to increase slightly with cooling rate.

Furthermore, all these data are shown in figure 78 to assess the effect of carbon content. It can be seen that Cmax increases from 1.75 to 2.8 % Mn when carbon content increases from 0.1 % C to 0.8 % C, respectively and the cooling rate has little effect.

By using these values, the segregation ratio was calculated by taking the average of Cmax divided by Cmin

$$S=Cmax/Cmin$$

It can be seen in figure 79 that the segregation ratio of manganese increases with carbon content and there is little effect of cooling rate in a similar way to Cmax.

6.3.2.3 Concentration map

Having obtained these large variations in Cmax, two transversely sectioned specimens, one of 0.8 C and the other of 0.1 % C produced at the lowest growth rate(1.5 mm/min) were examined at British Steel, Swinden Lab. in a computerised microprobe analyser which can produce a colour concentration map. From these maps, the distribution pattern of manganese

segregation can be seen between the primary arms and how it is related to the geometry of the arms.

Figures 80 and 81 show these concentration maps, each printed with a different range of composition given by the colours. It can be seen in figure 80-a, that in general concentration between primary arms contains between 2.00 to 2.35 % Mn, indicated by the yellow colour. A similar amount of manganese concentration was obtained with line analysis. In the map, very highly segregated and randomly distributed points are observed, indicated with red colour(higher than 2.35 % Mn). Then when this map was printed in different composition ranges, it was revealed that in the specific points, maximum concentration can go up to almost 4.00 % Mn, which is enormously high. This was shown by the small orange points (3.5 to 4.00 % Mn) in the center of the yellow colour(3.00 to 3.50 % Mn).

By combining this picture with the coalescence process which was mentioned in the section 6.2 and shown in figure 27, it is believed that the highest segregation tends to take place between the primary arms, surrounded by three or four secondary arms(figure 27). These are the last points to solidify. It is called concave point in this study. The sections of these points are shown in figure 22. Details are given in the next part.

In these maps, no attention is paid to the minimum concentration, because it does not vary too much at the high carbon content during growth.

At the 0.1 % C, exactly the same segregation behaviour was observed. The maximum is randomly distributed. In the maps, the

minimum was about 1.45 % Mn while the maximum concentration was around 1.65 % Mn (figure 81-a). But the average for maximum was varied from 1.60 to 1.65, indicated with the yellow colour in figure 81-b.

6.3.2.4 Concave solidification

The high concentrations of manganese were seen at specific points in the microstructure as a result of rejection of interdendritic liquid from between secondary arms to between the primary arms. This situation is sketched in figure 22. When the close packed primary arms are arranged on the transverse section (figure 22-a) as evidenced by metallography in figures 32 to 36, two possible secondary arms are considered as geometrical models: one in which the remaining liquid region is surrounded by four side arms and in the other, it is surrounded by three(figure 22-b). Each secondary arm is also assumed to be like a disc shape as Rickinson(44) has suggested.

In an attempt to follow these ideas, the specimens of 0.8 % C were analysed on the longitudinal section. The results are shown in figures 82,83 and 84. Although the maximum concentration of manganese varied within a large range, generally they were higher than measurements taken between the primary arms on the transverse section and between the secondary arms on the longitudinal section (figure 83). The Cmax was around 3.5 % Mn. The calculated segregation ratios for those data show similar results as in figure 84. The ratio rises from 1.5 between the secondary arms to 2 between the primary arms, while it is 3 in

the last points to solidify(concave points), so that segregation and concentration are related to the geometry in dendritic solidification.

6.3.2.5 Dendrite tips

Figure 85 shows a typical primary tip. Although it is obvious that the segregation is between the brown center and blue edge, it was difficult to see dendrite tips as clearly as in the organic materials because of quenching effects. One of these dendrite tips was analysed by electron microprobe through the centre of a primary arm. Figure 86 shows microprobe profile. Through the centre of the primary dendrite, the manganese profile did not change(Cmin 1.26 % Mn) except close to the dendrite tip. At the tip of the dendrite, the manganese concentration pattern which is attributed to the existence of fine dendrites originated from the quenched liquid. From this data, the effective distribution coefficient(ke) can be calculated approximately.

$$ke = Cs/Cl$$

where Cs is solid concentration at the tip

Cl is liquid concentration

In this case, the value of ke = 1.26/1.59 = 0.79 is in good agreement with previous studies for the equilibrium distribution coefficient of manganese between austenite and liquid, indicating that there is little solute undercooling in this specimen(81,169).

It is found that the value of ke for ferrite is slightly higher than 0.79, as 1.31/1.57 = 0.83.

6.4 Computer results

Four computer models were developed for microsegregation between the primary arms, three of which depended on different arm morphologies and one which considered concave solidification. The secondary dendrite arms with coarsening was developed by Ogilvy and Kirkwood and used also in this study. All models are compared with experimental results as a function of cooling rate which are recorded in tables 5 to 8.

6.4.1 Effect of model variable in coarsening model

The microsegregation of the secondary arm coarsening model in the ternary alloy was used to see the sensitivity of the parameters on the results by changing only one parameter. The results are plotted as concentration of manganese against fraction of solid, which is a fraction of the half secondary arm. It may be noticed in table 4 that the secondary arm results show large variation in coarsening rate(n) and pre-exponential constant(A). The variation is checked with the secondary arm coarsening model. When n is changed from 0.5 to 0.4 by taking A equal to 5 microns/sec, it can be seen in figure 87-a that Cmin and Cmax increase slightly. When n is taken 0.5, A is increased from 5 to 10 microns/sec, so that secondary arm spacing increases twice. Only the Cmin decreases slightly from 1.32 to 1.295 % Mn (figure 87-b)

Also the diffusion value at the liquidus temperature is used instead of temperature dependent diffusion values. It can be seen

in figure 87-c that the increase in Cmin is from 1.32 to 1.34 % Mn. The change in Cmax is very small.

These changes in Cmax and Cmin as a result of varying these parameters cannot be detectable practically. However, when the planar fixed secondary arm model is used to compare with the secondary arm coarsening model, it is seen that the Cmax increases up to 3.5 % Mn. In the case of the coarsening model, it results in 1.94 % Mn.

All these results indicate that the coarsening parameters and diffusion values affect the results marginally, whereas the model with fixed secondary arm seriously overestimates the segregation in the Fe-C-Mn ternary system. The cooling rate also does not change the results.

6.4.2 Computer results of secondary arm coarsening model, the effect of carbon content and cooling rate

The secondary arm coarsening model is compared with experimental results for high carbon(austenite) until the temperature drops to around 1200 C. As shown in figure 65, the model may predict the Cmax and Cmin in 0.4 and 0.8 % C specimens quite closely. It may be noticed that although both of them solidify initially as austenite, 0.4 % C specimens show higher values in Cmin and lower in Cmax than the 0.8 % C specimens, because the solidification is completed for the 0.8 % C around 1350 C, whereas it is at 1425 C for the 0.4 % C. This means that there is longer homogenization time for the low carbon content at the high temperature.

Although the peritectic reaction model was not developed for

microsegregation in this study, the computer can run for 0.1 % C until solidification is complete by assuming that the peritectic reaction is not involved. As plotted in figure 88, it shows very little segregation for both coarsening rates. This low segregation around 1485 deg C can be reduced to a much lower level with further cooling, which means that it can be ignored in practice. In the experimental work, the same results were found as the model predicted.

It may be noticed in figure 89 that cooling rate does not influence the segregation ratio between side arms, unless arm coarsening changes greatly with cooling rate, which has not been observed.

However, the model cannot predict the disappearance of side arms at the lowest cooling rate(1.5 mm/min), because the coalescence mechanism is the dominant process rather than ripening by remelting.

6.4.3 Computer results of primary arm models and the effect of carbon content and cooling rate

The large variation in Cmax was obtained in all specimens. These values are plotted in figures 74,75,76 and 77 as a function of cooling rate including computer results. Three computer models are used. The Cyl-2 model considers the primary arms as a cell by ignoring poorly developed secondaries, whereas Cyl-1 and the planar model consider the long secondary arms in the close packed arrangement as a cylinder and a plane, respectively.

The lowest and highest of Cmax can be predicted by Cyl-1 and

Cyl-2, respectively, for 0.1 % C. But when the Cmin and the segregation ratio are compared for all models in 0.1 % C, it can be seen in figures 90 and 91 that the Cyl-2 can estimate better for the lowest cooling rate(0.25 C/sec), whereas the planar model is better for the high cooling rates. This difference arises from the geometry of primary arms at the lowest cooling rate.

For the austenite solidification case, only the planar and Cyl-1 were compared with experimental results because the cellular dendritic morphology was not observed. The planar model can predict the highest Cmax whereas the Cyl-1 predicts the lowest Cmax for both 0.4 and 0.8 % C contents. When the segregation ratios are plotted in figures 92 and 93 by taking the average of Cmax, it is seen that the Cyl-1 model fits better.

It is found generally that the model prediction of Cmax and segregation ratio increases with cooling rate up to 2 C/sec; then it becomes constant.

6.4.4 Concave solidification results

The computer results are plotted in figure 82. The model overestimates the Cmax although there is a good agreement between the concentration map and the model prediction for the lowest cooling rate. However, when the simplicity of the geometric assumption of the model is overcome, it is believed that good agreement will be found, even at high cooling rates. Also the computer model needs to be compared with a concentration map rather than a line analysis, because the Cmax of the region

cannot be easily obtained with line analysis.

The Cmax tends to increase with increasing the cooling rate up to 2 deg C/sec, whereas the experimental results are constant.

6.4.5 Homogenization

Although the homogenization experimental work was not carried out in this study, the index of residual manganese segregation was calculated by using the planar computer model for primary arms, because this model predicts the maximum of the Cmax. The index of residual segregation is defined by the following equation(51).

$$\delta_t = \frac{C_M - C_m}{C_M^0 - C_m^0}$$

where C_M max concentration of Mn at time t

C_M^0 max concentration of Mn at beginning

C_m min concentration of Mn at time t

C_m^0 min concentration of Mn at beginning

The results are plotted as a function of temperature and homogenization time in figure 94 for the highest and the lowest cooling rate cases in 0.4 % C. It can be seen that there is a big effect of primary arms spacing, homogenization time and temperature. It can be suggested that at least three hours are required at 1200 deg C to reduce the segregation to half of its initial value.

The decrease of Cmax and Cmin is also calculated during the

solid state cooling after solidification is completed. As shown in figure 95, the change in Cmax is up to around 1250 deg C; then with further cooling, the change becomes marginal. The Cmin is practically constant during further cooling.

CHAPTER 7. DISCUSSION

7.1 Morphology of dendrite arms

In practice, alloys usually solidify as dendritic structure. This structure, which is characterized by primary and secondary dendrite arm spacings, significantly determines microsegregation and, therefore, the mechanical properties of cast alloys. Under these circumstances it is essential to understand the mechanism of dendrite arm formation in order to control the properties of cast alloys(51).

7.1.1 Primary arm spacing

Primary arms can grow in both the form of the close packed arrays (interlocking) and of the rectangular arrays in metallic alloys(39,42,43,44,46,47,49,159) (see fig. 36). Both these arrangements were found in all specimens and they were identical to low alloyed carbon steels as observed by several researchers(44,46,47). Jacobi and Schwerdtfeger(46) investigated in detail two carbon steels and defined two different primary arm spacings in the close packed structure. One primary arm spacing is perpendicular to the distance between the rows of aligned secondary arm and the other one is along the rows (figure 22). It is found that spacings which are between rows are mostly 1.07 times higher than spacings which are along rows. This ratio was reported as 1.17 by Jacobi and Schwerdtfeger(46). This difference might have arisen from different experimental conditions and compositions, as well as experimental errors. But these results agree in essence.

In ingot cast structure, the primary arm spacing is usually

related to the inverse square root of the cooling rate(51). However, the solidification conditions in ingots are different from those for steady-state solidification, where growth rate and temperature gradient are independently controlled and can be independently related to primary arms. When primary arm spacings were determined as a function of temperature gradient in the liquid and growth rate (figures 39 and 40) in the present work, it is found that the primary arm spacing decreases with increasing the temperature gradient in the liquid and with increasing the growth rate for the same alloys. These results are correlated by

$$\lambda_1 \propto G^{-0.5\mp0.1} V^{-0.4\mp0.1}$$

However, the accuracy of these results was not very high because even under the best conditions, three data points were taken into account for calculations and there could be experimental errors in the temperature measurements. On the other hand, it seems to be that these data could be expressed by the cooling rate because both exponents are very close to 0.5

$$\lambda_1 \propto W^{-0.5}$$

These results obtained from the present work are in good agreement with the conclusion of other workers(42,44) that the primary arm spacing is inversely proportional to the square root of cooling rate.

The present data were found to be extremely difficult to compare directly with similar low alloyed carbon steels. These

difficulties arose from composition, experimental conditions and technique differences. Jacobi and Schwerdtfeger(46) and Suzuki and Nagoaka(43) used very low growth rate and high temperature gradients, whereas Rickinson(44), Edvardsson at al(48) and the present study used relatively low gradients and high growth rates. For these reasons, all available data in the literature for similar alloys were compared with the theoretical primary spacing relationship of the form $G^{1/2}$ $V^{1/4}$. It is found that the correlation of these experimental measurements is in good agreement, inspite of a composition difference among them (figure 41). In addition, five models, which are Burden and Hunt (B-H)(26), Kurz and Fisher (K-F)(31) and Trivedi (T)(28,29,30), Laxmanan's minimum undercooling (Lmu)(27) and stability (Ls) (32,33) models were compared with them for only the 0.8 % C case. It is seen that the models proposed by K-F ,T, Ls, and Lmu seriously overestimates true values, whereas the model proposed by B-H slightly underestimates it. This was in very good agreement with the experimental work of Taha et al(47) who observed the same behaviour in high alloyed steels, when they compared data only with the B-H and K-F model.

Recently, Tewari(50) reported that primary arm spacing in Pb-8 % Au and Pb- 3 % Pd alloys can be very closely predicted by Laxmanan's minimum undercooling and marginal tip stability models and Trivedi model, whereas the B-H model underestimates it. However, it is interesting that in the calculation of B-H model for Pb- 8 % Au, the experimentally measured equilibrium solidification range ΔT which is between the liquidus and

eutectic temperature was used (53.7 deg K), but in the other models, ΔT was calculated from $\frac{(k_o-1)\beta C_o}{k_o}$ equation. This gives enormously large solidification range as 587941.2 deg K when the below data is used

$$k_o = 0.0001$$

$$C_o = 8\ \%\ Au$$

$$\beta = -7.35$$

This forces the models to agree with experimental results. In fact, when the measured data is used for these models, their results seriously overestimate the primary arm spacing. In addition, k was assumed to be 0.0001. It is suggested that this can describe the true behavior of Pb- 8 % Au. However, there is no experimental data of ko for this binary system. The same arguments are exactly valid for Pb- 3 % Pd alloy.

From equation 1.21, it is seen that the influence of composition on λ_1 in a binary system is mainly based on the change of ΔT, therefore, carbon content should play a significant role on primary arm spacing. However, it is found that the primary arm spacing for ferritic steels is only slightly smaller than for austenitic steels. No strong effect of carbon content has been observed, but there is tendency to increase the arm spacing with increasing carbon content(figure 43). Similarly, Taha et al(47) could not find any clear difference in primary spacing between carbon steels and highly alloyed steels, but a decrease has been observed by decreasing carbon content. These results are consistent to the observation of Suzuki and Nagoaka(43). In contrast, Edvardsson et al(48) reported a slight

decrease in λ_1 with increasing carbon content for low carbon steels. Most probably, there was a large amount of experimental error in temperature gradient measurements, because it is not clear where they are measured and they are only slightly decreased with increasing enormously the growth rate from 10 mm/min to 1000 mm/min at the low gradient apparatus. At the high gradient apparatus, the opposite effect was found. For these reasons, this result cannot alter the conclusion of the present and other workers's observation that the primary arm spacing increases slightly with increasing carbon content. However, two points are certain: the theoretical models do not accurately predict primary arm spacings as a function of composition and in any case are only valid for binary alloys. In the calculations, it is assumed that alloy elements do not affect primary arm spacings. The theory for multicomponent systems has not been established.

Primary arm spacing does not vary with the distance during growth. This is consistent with the observations of other workers(44,69,156,159).

7.1.2 Secondary arm spacing

It is well established that secondary dendrite arm spacings are significantly governed by time spent in the solid-liquid region(26,42,44,51,53,58-61). In this way, they were plotted against solidification time on a logarithmic scale for each specimen as shown in figures 44-53. These lines can be represented by well-known $\lambda_2=At^n$ equation. Results indicated that the exponent of the coarsening equation in these alloys is comparatively high and the statistically calculated average of

the exponent, n, seems to be 0.45. This is the highest coarsening value so far in literature which has been measured in metallic alloys. These frequently remelting or coalescencing side arms can be explained by high surface energy between solid/liquid interface, which is the driving force for coarsening. As a result of this, it may be surmised that the surface energy of these alloys is higher than any other metallic alloys. Another result of this observation is that this enormous increase in secondary arm spacing during growth will reduce microsegregation between secondary arms as obtained in this work.

It may be noticed in figures 44-53 that the data obtained from high growth rates tend to lie below that from low growth rates. These results clearly demonstrate that the secondary arm spacing decreases with increasing growth rate as observed in Al-Cu(42) and Fe-Cr-C alloys(44). However, the effect of the growth rate on the coarsening exponent was not obvious, although there was a slight indication of an increase with growth rate. Rickinson(44) suggested a simple linear coarsening equation for similar alloys and found that the coarsening rate will be higher as the growth rate rises under the same temperature gradient.

The temperature gradient determines the length of solid-liquid region under constant growth rates. Therefore it is expected that the final arm spacing can be increased with decreasing temperature gradient, because of time for solidification varies. It is found that final arm spacings were smaller for high temperature gradient than that for low temperature gradient. However, the sensitivity of coarsening exponent with temperature

gradient was not seen. When final secondary arm spacing was compared with commercial steels, containing from 0.1 to 0.9 % C (fig. 7), as a function of cooling rate, it was found that the final seconadry arm spacing in the present work was smaller than that in commercial steels. This could be explained by different criteria for obtaining the cooling rate since in an industrial ingot the cooling rate will change with time during solidification.

The dependence of coarsening exponent on both growth rate and temperature gradient was mainly based on statistical calculations. Furthermore, in these alloys a large scatter of secondary arms was found, so that the sensitivity of coarsening exponent relating to these variables was found to be more difficult than final arm spacing since it is subject to statistical errors.

The dendrite coarsening can occur by both ripening and coalescence mechanisms(42,51,66). The ripening seems to be predominant at the beginning of solidification, whereas coalescence becomes predominant near the end of solidification. This has been observed in the present study. It is also seen as shown in figures 68-71, that the volume of liquid between secondary arms was significantly reduced between secondary arms. It is indicated that there is solute diffusion from the root of the adjacent secondary arms to their tips. This coalescence process clearly increases coarsening and as a result of this diffusion, the manganese segregation between secondary arms will be less than that between primary arms as observed in the present study. In addition, these secondary arms always disappeared at the lowest growth rate with long diffusion times. The microstructure becomes non-dendritic. This is in very good agreement with the conclusions of Morrensen et al(59).

It can be seen in equation 1.45 that the dendrite arm spacing can

increase with temperature, surface energy and diffusion in liquid. Since increasing the carbon will lower the temperature at which solidification occurs, diffusion of solute in the liquid will decrease leading to reduced coarsening kinetics, assuming the effect on surface tension to be minimal. Therefore the fine dendritic structure can be expected at the high carbon contents. This is observed in the present study.

Jacobi and Schwerdtfeger(46) investigated the final secondary arm morphology in directionally solidified specimens (not quenched during growth). By plotting secondary arm spacings against solidification time, it is found that secondary arms in 0.6 % C steel coarsen as 15.8 and in 1.60 % C steel as 7.16 . The constants in the equation are in excellent agreement with present work, although they used very low growth rates, i.e. long solidification times.

7.2 Cmin measurements

7.2.1 In secondary arms

The back diffusion in these alloys (Fe - 1.6 % Mn - 0.1 to 0.8 % C) should be investigated as a function of carbon content so that the variation in Cmin can be related to the primary phase. This distinction is needed simply because the diffusion coefficient of manganese in ferrite is significantly (42 times) higher than in austenite.

In the 0.1 % C specimens , the value of Cmin increased from 1.35 % Mn to around 1.55 % Mn in many cases (figures 55,56 and tables 5 a,b,c). As a result of this high homogenization, secondary arms completely disappeared at the end of solidification. This can only be explained by high back diffusion in secondary arms.

It may be also noticed in figures 55,56 that the rise in manganese concentration up to 20-30 °C below the liquidus, which is almost at the onset of peritectic reaction, is very high. Because the initial side arm spacings are very small, i.e. the back diffusion path is very short, it can be expected that the Cmin rises very quickly at the early stage of solidification. Then with the formation of austenite at the peritectic reaction, only a marginal increase in manganese concentration was seen, because of low diffusivity in austenite.

A similar increase in Cmin at the 0.2 % C specimens was observed from 1.32 to around 1.42 % Mn. This result is almost identical with the observations in 0.1 % C specimens. The slight difference in Cmin between 0.1 % C and 0.2 % C arises the percentage of ferrite, which is roughly 100 % in 0.1 % C and 75 % in 0.2 % C at the end of solidification. This can also be a reason for secondary arms disappearing in the 0.1 % C alloys and not in the 0.2 % C alloys.

The Cmin determined in 0.4 and 0.8 % C specimens indicated different results from the low carbon because both alloys solidify as only austenite phase. The slow increase in Cmin from 1.26 to around 1.30 % Mn seems to be same in both alloys. Again this can be explained by initially small secondary arms, i.e. short diffusion path. Then the rise in Cmin gradually decreases with increasing dendrite size.

When the initial Cmin can be related to koCo, Cmin/Co should be close to ko if there is no significant undercooling. In the case of 0.8 % C, 1.26/1.59 is 0.79, which is very close to 0.78 the equilibrium distribution coefficient ko of manganese between

austenite and liquid(102). This slightly high value for ko shows that very little solute undercooling existed in these austenitic steels under the present conditions. In the case of 0.1 % C, 1.31/1.57 is 0.83 (ferrite). Both results are in agreement with the calculation of Battle and Pehlke (169).

The effect of TGZM may also contribute to the rise in Cmin. As described before in the section 1.8, in this process it is assumed that the existence of the composition difference under high temperature gradient in the secondary interdendritic pool causes remelting at the trailing edge and solidification at the leading edge, so that this can produce a migration of side arm up the temperature gradient towards the primary tips(64,65). This results in a 'Saw-tooth' profile(56). It can also increase Cmin. This remelting definitely occurs in practice. Although it is difficult to detect in single phase alloys, it has been clearly observed in tool steels(57) that the back side of secondary arms moved into the central delta ferrite by remelting. However, it is not certain how effectively this process can increase Cmin independently of back diffusion. This is quite difficult to determine in single phase alloys.

It seems likely that secondary dendrite arms initially grow symmetrically, i.e. without TGZM effect, so that the initial rise in Cmin can only be attributed to the back diffusion. Then both processes will combine to increase Cmin when TGZM becomes effective at the later stage of growth.

It can be seen from equation 1.50 that the total migration distance at the end of the solidification depends only on the

growth rate, if it is assumed that the final and initial liquid composition do not vary with it, which is likely true(65,56). At 30 mm/min rates, the ratio of the total migration distance to final arm spacing is 3/40 = 0.075, which means that only 7.5 % of arms is replaced by TGZM. Approximately these ratios are 0.50, 0.13 and 0.10 for 1.5, 6 and 15 mm/min growth rates, respectively. Here, it is seen that the half of the secondary arms are replaced at the lowest growth rate. It will be remembered that high coalescence and high back diffusion also occur for these low growth rates, and all this will lead us to expect very high homogenization, i.e. high Cmin, and as a result of it, the disappearence of secondary arms. This expectation was found in all the lowest growth rate specimens. The Cmin increased up to 1.5 % Mn even in the case of austenitic solidification. Segregation only remained significant between primary arms.

As another possibility, the rise in Cmin has been explained by the existence of tertiary cells or arms in some alloys(44). These tertiary arms have usually been observed at the early stage of growth. It is suggested that when these arms are annealed out, the liquid between the arms or cells provide rich solute sources for back diffusion. However, this process cannot clarify the rise in Cmin in the present case, because tertiary arms or cells have been not seen even at the beginning of growth. It has also been noticed in this study that tertiary arms or cells can be easily confused with dendrites formed from the liquid if the quenching is not fast enough.

7.2.2 Within primary arm

The Cmin was analysed on the longitudinal section during growth as well as on the transverse section in the 0.1 % C and 0.2 C % specimens. For other alloys , the analysis of Cmin was usually carried out on the transverse sections rather than the longitudinal ones. It is found that the concentration analysis on both sections are in good agreement. The Cmin in the 0.1 % C specimens increases up to 1.45 % Mn and up to 1.41 % Mn in the 0.2 % C specimens.

There is not much data in the literature with which to compare the present results directly. Matsimuya et al(102) have investigated a unidirectionally solidified low carbon steel (Fe - 0.13 % C - 1.52 % Mn) at 0.05 K/sec. The result of the computer aided microprobe analysis producing an concentration map indicated that poorly developed secondary arms disappeared at the end of the solidification and the manganese segregation remained between the primary arms. If the final Cmin of this specimen for primary arms is compared with the present result, as ke= Cmin/Co for Mn, it can be seen that ke is approximately 0.93 in both cases. Although a slight decrease in Cmin is observed with increasing cooling rate in their work, no clear effect has been observed in the present study given the accuracy of microprobe analysis.

Rickinson(44) investigated Fe - 1.4 % Cr - 1.0 % C steel under similar conditions. He observed a slight rise in Cmin of Cr during growth in the primary arm cores. Although Cmin was not analysed in the core of primary arms for 0.8 % C in this present

study, the result of Cmin obtained between the secondary arms is consistent with his conclusion.

Flemings et al(73) reported that the Cmin increases with decreasing cooling rate in cast Fe -1.5 % Cr - 1 % C alloy. (from chill region, 1.20 % Cr, to ingot centre 1.0 % Cr in cast) If this high concentration of Cr can be attributed to greater back diffusion in fine structure near the chill region and solute undercooling at the high cooling rates, then it can be suggested that there was very little effect of Cmin with cooling rate as observed in the present work for all carbon contents.

In summary, it can be said that the back diffusion of manganese is significantly high only in low carbon steels. The TGZM effect and coarsening of secondary arm also play an important role as well as diffusion for the rise in Cmin, especially at the low cooling rates.

7.3 Final Manganese Microsegregation and Effect of Variables

7.3.1 Between the secondary arms

The microsegregation measurements of manganese during growth between secondary arms were carried out separately from primary arms. The result obtained from both regions indicate that the manganese segregation between side arms is clearly less than that between primary arms. This low segregation in the secondary arms can be explained by several suggestions:

1) Coarsening occurs by ripening or coalescence processes and in the case of ripening, the secondary arms remelt. This initially solidified low solute concentration solid dilutes the liquid, therefore reducing microsegregation(57,99,113).

2) On the other hand, TGZM effect can also dilute the liquid as well(65). However, as shown in the previous section 7.2.1, this total replacement, i.e. remelted part, could be only about 10 % of total arms or less at the high growth rates, so that this dilution of liquid cannot be effective as much as ripening process, if it is considered that initially 2-3 microns of secondary arms coarsen up to 120 microns.

3) Another reasonable suggestion can be made in term of the coalescence process(42). As described before in the section 1.7 , the highly concentrated liquid between the secondary arms can be rejected to regions between the primary arms. As a consequence of this, the segregation is reduced between the secondary arms but is enhanced between the primaries.

It is difficult to separate these three processes. One thing is certain that although they all can reduce segregation between secondary arms , the morphological and the microprobe results indicate that the coarsening of secondary arms by coalescence can be the dominant factor for this reduced segregation between the secondary arms.

The minimum and maximum measurements between secondary arms at the end of solidification were used to calculate the segregation ratio of manganese. As shown in figures 65 and 66 the manganese segregation is mainly determined by carbon content, rather than cooling rate.

The manganese or any other elements have not been separately analysed between secondary and primary arms by other workers and reported in the literature. Therefore these results cannot be

compared directly with any other study.

Hammar and Grunbaum(158) investigated segregation of several elements in low alloyed steels and found in a 0.4 % C steel that manganese segregation values seem to be fairly constant from the chill region at 1.50, to the centre at 1.55, in a 50 kg ingot. These measurements could have been done between secondary arms, although spacings were not mentioned; otherwise they are indeed very low for a 0.4 % C austenitic steel. Similar behaviour was reported for Cr and Ni in the same specimen. This result is in excellent agreement with the conclusion of the present study for secondary arms.

7.3.2 Between the primary arms

The final manganese concentration were analysed on transverse sections which correspond to about 1200 C below which no further homogenization were observed. A variation in Cmax between primaries was observed due to the morphology of dendrites. The change in Cmax with cooling rate does not show any particular trend for different carbon contents (figures 74-78). The only factor that affected the segregation ratio and Cmax is carbon content (figure 78). The ratio increases linearly with carbon content from 1.35 at 0.1 % C to 1.8 at 0.4 % C, then seems to gradually slow down. It finally reached a value of 2.3 at 0.8 % C (figure 96).

Although both 0.4 and 0.8 % C steels solidify as austenitic they produce different results. The most reasonable explanation for this is that the solidification of 0.4 % C steel finishes

carbon steels can reduce more (at a relatively higher temperature i.e. high back diffusion coefficient) than the high carbon one. As shown in figure 95, solid state homogenization during cooling is effective up to around 1250 C.

Another reason for the influence of carbon on the segregation ratio could be the interaction between carbon and manganese in the solid and the liquid phase, i.e. the change of partition coefficient of manganese with carbon content. However, this effect was found to be very small for manganese. Therefore it is difficult to believe that this is the cause for the change in segregation in manganese steel with carbon content.

The rise in manganese segregation has been reported (157) to be from 1.3 at 0.1 % C to 1.9 at 0.8 % C. These results are in good agreement with trend in the present study, but their values are found to be lower at the high carbon end than this work. The most reasonable explanation for this difference could be that the data were taken from several different regions, so that the average could be low.

Rickinson(44) investigated segregation of Cr using random probe analysis in Fe - 1.9 % Cr - 0.5 % C steels under different cooling rates and found that the segregation ratio does not change with cooling rate and it is 1.75. If this value is compared with the 0.4 % C present specimens, an excellent agreement will be seen. These results are consistent with the observation of Doherty and Melford(78) and Fredriksson(162) for similar carbon content, although the cooling rate are different in each work. However, the above results are smaller than the

measurements of Flemings et al (S = 3.3) for a similar alloy(73).

For 1 % C , Rickinson(44) recorded the Cr segregation between 2.20 to 2.50 up to 3 C/sec cooling rate, if the high segregation values at the fast (more than 3 K/sec) and low (less than 0.5 K/sec) cooling rates are ignored. Similarly, the manganese segregation ratio was found around 2.35 for 0.8 % C in the present study. This common behaviour for these different elements leads us to expect that the effect of carbon content on segregation of Cr and Mn will be the same as obtained experimentally, because the distribution and diffusion coefficients for both elements are close to each other.

In the Fe-Cr-C alloys, it was also reported that at the high carbon contents (after about 1.5 % C)(162,73) the eutectic reaction appeared during the solidification. Consequently, the segregation ratio of Cr showed a maximum, found experimentally to be at about 1.6 % C. This eutectic reaction has not been seen in the present study conditions.

7.3.3 Concave Solidification

Highly segregated points were observed between primary arms surrounded by secondaries on the longitudinal section as well as on the transverse sections. These spots were also confirmed with computerised microprobe analyser, which produced a colour concentration map, relating the Mn concentration to the dendrite morphology. Although the line analysis could not reveal the highest concentration, the microprobe results obtained from these points on the longitudinal section showed even higher segregation

points on the longitudinal section showed even higher segregation ratio than for primary arms (figures 82-84).

Most probably, the coalescence process could be the reason for these highly segregated points, as explained in sections 6.2 and 6.3.2.4. It may be expected that they have also more potential for nucleation of porosity, of inclusions or of second phases than any other region. In the present work, specimens contained low sulphur and phosphorus levels (less than 0.005 %). However, in the industrial practice, these elements could be present up to 0.05 % (standard limit), therefore higher manganese segregation may occur with the possibility of forming MnS inclusions.

7.4 Computer Modelling

One of the most important problems in the computer modelling of segregation is the true representative back diffusion distance. To find this distance, we should consider the shortest diffusion path and we should relate it to the actual dendritic growth morphology. Morphological assumptions have been already discussed in section 5.3. Their validity is generally acceptable for all models, except the concave solidification model. This model simply assumes that all solute concentrates towards the centre of a cylinder instead of segregating uniformly between the secondary and the primary arms. It needs definitely two, maybe three dimensional back diffusion and solidification models in order to overcome this oversimplification.

The cylindrical cellular primary arm model also ignores the small area between three primary arms, because the cylindrical shape does not cover this area completely. As shown in appendix

2, the primary arm used in the computer model should be 1.05 times higher than the obtained measurements. However, this difference can cause only 2 % increase in Cmax and decrease in Cmin. Therefore it does not seriously affect the results.

All present computer models used for the comparison of experimental results was applied for the first time seriously to the ternary Fe-C-Mn alloys by Ogilvy(57). These models also consider the carbon effect which significantly controls solidification range of steels. All other computer models in the literature apparently ignore this influence.

It is generally found that the cylindrical primary arm model can estimate the manganese Cmax and segregation ratio better than planar model. The planar secondary dendrite coarsening model is in excellent agreement with experimental results. Only the concave solidification model seriously overestimates the experimental results.

A peritectic solidification model is essential for low carbon steels, in order to check the experimental measurements. It might be also useful to check the models with measurements from castings.

8 CONCLUSIONS

1. The metallography of unidirectionally solidified specimens showed that primary arms grow mainly in the so-called 'close packed' arrangement (interlocking) and their spacings do not increase during the steady-state growth.

2. Measurements of primary arm spacings indicated a decrease with increasing the growth rate and the temperature gradient in the liquid, but only a slight increase with increasing carbon content. These growth variables can be correlated by

$$\lambda_1 \propto G^{-0.5 \mp 0.1} \; V^{-0.4 \mp 0.1}$$

3. There was no evidence of tertiary dendrite arm formation during steady-state growth in all steels investigated, even at the beginning of solidification.

4. Secondary arm spacings decreased with increasing cooling rate. The coarsening exponent in the present steels was found to be higher than any known non-ferrous alloys. The constants in the exponential relationship are

$$\lambda_2 = A \; t^{\wedge}$$

where $A = 10 \mp 5$, $n = 0.45$

λ_2 in micron

t second

5. Manganese back diffusion in the solid phase during the growth has a large influence on microsegregation when the first solid formed is delta - ferrite. A decrease in Cmin after 0.1 % C has

been observed because the fraction of delta phase decreases with increasing carbon content. Only a small rise in Cmin during the growth was found in both 0.4 and 0.8 % C steels but there was no difference between them indicating that both solidify as austenite.

6. Manganese back diffusion in the secondary arms was higher than in the core of the primary arms in the ferritic solidification.

7. Secondary dendrite arms grown at the lowest rate (1.5 mm/min) always disappeared at the end of solidification for all steels. These non-dendritic structures were attributed to high coalescence, back diffusion and TGZM processes.

8. Manganese segregation between the primary arms was significantly higher than between the secondary arms in all conditions and specimens. This was attributed to the coalescence of secondary arms rejecting solute into the region between the primaries.

9. Linear regions such as between the primary arms surrounded by secondaries are last to solidify. These concave solidification 'spots' showed even higher segregation than normal between primary arms.

10. Manganese segregation ratio between the primary arms increased with carbon content from 1.3 at 0.1 % C to 2.25 at 0.8 % C, whereas it increased from 1.03 at 0.1 % C to 1.5 at 0.8 % C between the secondary arms.

11. Manganese segregation between the secondary arms did not vary with cooling rate. Only a slight rise in the manganese segregation between primary arms was obtained with increasing cooling rate.

12. Asymmetric solute distribution profile (saw-tooth or TGZM effect) has been observed between secondary arms in all specimens under present experimental conditions.

13. Predictions from the secondary dendrite arm coarsening model in the ternary Fe-Mn-C alloy proposed by Ogilvy and Kirkwood showed very good agreement with experimental results. The same model without arm coarsening was applied for different primary arm morphologies. The cylindrical primary arm model predicts the minimum of Cmax measurements between the primary arms, whereas the planar one predicts the maximum of Cmax. measurements. The concave solidification model seriously overestimated the experimental measurements made on the 'spots' between primaries.

SUGGESTIONS FOR FURTHER WORK

1. The morphology of segregation pools as shown in fig. 27 should be investigated further to show whether these pools are isolated or interconnected.

2. The temperature gradient should be controlled closely in each specimen and the effect of it on TGZM, for a large variation of temperature gradient, should be investigated.

3. Microsegregation should be investigated using concentration maps rather than line analysis.

4. A peritectic solidification computer model is essential for low carbon steels in order to check the experimental measurements.

APPENDIX-I

```
CLS
REM                    by Altan  TURKELI - 20/8/1989
REM       ***************************************************************
REM        Segregation in Fe-Mn-C alloy
REM             1-Secondary arms with coarsening
REM             2-Planar primary arms
REM             3-Cylindrical primary arms( convex solidification )
REM                  a- for high carbon
REM                  b- for low carbon
REM             4- Concave solidification of spot between primary arms
REM      ***************************************************************
DIM b(600)
GOSUB begin
GOSUB datagive1
GOSUB datagive2
GOSUB setup

REPEAT

GOSUB timediff
GOSUB backdiff
GOSUB grad1
GOSUB moveinterface
GOSUB newintercon

UNTIL xi/l >= 1.000

GOSUB segratio

GOSUB check
PRINT " do you want to do homogenization during solid-state cooling "
INPUT " if yes type 1 ,if no type 2     ",yyy
IF yyy=1 THEN GOTO hom1 ELSE GOTO hom2
LABEL hom1
GOSUB homogen
GOSUB check
GOSUB segratio
LABEL hom2
PRINT " do you want to do homogenization for several hours "
INPUT " if yes type 1 , if no type 2    ",yy1
IF yy1=1 THEN GOTO hom3   ELSE GOTO hom4
LABEL hom3
GOSUB homogen1
LABEL hom4
GOSUB check
GOSUB segratio


END


LABEL begin
PRINT " THESE ARE  TERNARY MICROSEGREGATION COMPUTER PROGRAMS FOR STEEL "
PRINT " WHICH PROGRAM DO YOU WANT ? "
PRINT " TYPE -1  PLANAR SOLIDIFICATION FOR SECONDARY DENDRITE ARM WITH COARSENIN
G "
PRINT " TYPE -2  PLANAR SOLIDIFICATION FOR PRIMARY DENDRITE ARM "
PRINT" TYPE -3  CYLINDRICAL CONVEX SOLIDIFICATION FOR PRIMARY DENDRITE ARM "
PRINT " TYPE -4  CYLINDRICAL CONVEX SOLIDIFICATION FOR CELL ( LOW CARBON )"
PRINT" TYPE -5 CYLINDRICAL CONCAVE SOLIDIFICATION FOR PRIMARY DENDRITE ARM "
INPUT " N   " , ab
RETURN


LABEL datagive1
IF ab=1 THEN GOTO coar ELSE  GOTO pp
```

```
LABEL coar
PRINT " TYPE A AND n  where L2=A*t^n  L2= half of secondary arms as meter "
PRINT "                               A= constant as meter "
PRINT "                               n= exponent      "
PRINT "                               t= time  (sec.) "
INPUT " A  ",a
INPUT " n  ",nn
LABEL pp
IF ab=2 THEN GOTO ppp ELSE GOTO cp
LABEL ppp
PRINT "TYPE  L1    primary arm spacing  as meter "
INPUT " L1  ",l
l=l/4
LABEL cp
IF ab=3 THEN GOTO spp ELSE GOTO scp
LABEL spp
PRINT " TYPE L1    primary arm spacing  as meter "
INPUT "L1  ",l
l=l/4
LABEL scp
IF ab=4 THEN GOTO kel1 ELSE GOTO kel2
LABEL kel1
PRINT " TYPE  L1  primary arm spacing as meter    "
INPUT " L1   ",l
l=l/2
LABEL kel2
IF ab=5 THEN GOTO scpp ELSE GOTO fin
LABEL scpp
PRINT " TYPE  L1   primary arm spacing as meter "
PRINT "       L2 final secondary arm spacing as meter "
INPUT "L1  ", l1
INPUT "L2  " , l2
l=SQR((l1*l2)/(2*PI))
LABEL fin
RETURN


LABEL datagive2
PRINT " These data are used."
PRINT
PRINT " for ferrite                  for austenite "
PRINT "  kmn=0.78                       kmn=0.78 "
PRINT "  kc =0.18                       kc =0.33 "
PRINT "  Do =122E-6                     Do =49E-6 "
PRINT "  q  =55000                      q  =66000 "
PRINT "               %  Mn =1.6  "
PRINT "         % C = 0.1 , 0.4  and 0.8  "
PRINT"number of nodes  N= 30 for secondary  N=200 for primary dendrite arms"
PRINT "             cooling rate W (-),      as   C/sec"
PRINT "     liquidus slope for Fe-Mn   -5 "
PRINT "                        Fe-C    -70 for austenite"
PRINT "                        Fe-C    -81 for 0.1 and 0.4 % C "
INPUT "kmn   ",kb
INPUT "kc    ",kc
INPUT "do    ",do
INPUT "q     ",q
INPUT "% Mn  ",bav
INPUT "% C   ",cav
INPUT "Slope of liquidus for Fe-Mn(-)   ",mb
INPUT "Slope of liquidus for Fe-C(-)    ",mc
INPUT " Cooling rate  C/sec(-)      ", w
t=1535+mc*cav+mb*bav
PRINT " Liquidus Temperature ",t
INPUT " number of nodes  N    ",n
RETURN
```

```
LABEL setup
IF ab=1 THEN GOTO q1 ELSE GOTO q2
LABEL q1
DEF FNs(f)=bav*kb*(1-f)^(kb-1)
FOR i=0 TO 3
b(i)=FNs(i/n)
NEXT i
bl=b(3)/kb
cl=cav/(1-3/n*(1-kc))
cl2=cav/(1-2/n*(1-kc))
dcl=cl-cl2
dt=mc*(cl-cav)+mb*(bl-bav)
z=dt/w
l1=a*z^nn
l=l1
LABEL q2
IF ab=2 THEN GOTO q3 ELSE GOTO q4
LABEL q3
DEF FNs(f)=bav*kb*(1-f)^(kb-1)
FOR i=0 TO 3
b(i)=FNs(i/n)
NEXT i
cl=cav/(1-3/n*(kb-1))
cl2=cav/(1-2/n*(kb-1))
dcl=cl-cl2
LABEL q4
IF ab=3 OR ab=4 THEN GOTO q5 ELSE GOTO q6
LABEL q5
DEF FNs(f)=bav*kb*(1-f)^(kb-1)
FOR i=0 TO 3
b(i)=FNs((i*i)/(n*n))
NEXT i
cl=cav/(1-(9/(n*n))*(1-kc))
cl2=cav/(1-(4/(n*n))*(1-kc))
dcl=cl-cl2
LABEL q6
IF ab=5 THEN GOTO q7 ELSE GOTO q8
LABEL q7
DEF FNs(f)=bav*kb*(1-((n*n-(n-f)^2)/(n*n)))^(kb-1)
FOR i= 0 TO 3
b(i)=FNs(i)
NEXT i
cl=cav/(1-((n*n-(n-3)^2)/(n*n))*(1-kc))
cl2=cav/(1-((n*n-(n-2)^2)/(n*n))*(1-kc))
dcl=cl-cav
LABEL q8
bl=b(3)/kb
bi=b(3)
cs=kc*cl
dt=mc*(cl-cav)+mb*(bl-bav)
z=dt/w
t=t+dt
x=l/n
xi=3*x
r=3
p=1
RETURN


LABEL timediff
d1=do*EXP(-q/(1.986*(t+273)))
dz=x^2/(4*d1)
z=z+dz
dt=w*dz
t=t+dt
```

```
RETURN


LABEL backdiff
IF ab=1 THEN GOTO sv1 ELSE GOTO sv2
LABEL sv1
12=a*z^nn
d1=12-11
LABEL sv2
IF ab=1 OR ab=2 THEN GOTO sv3 ELSE GOTO sv4
LABEL sv3
ba=b(0)
b(0)=(b(0)+b(1))/2
FOR i=1 TO r-2
bb=b(i)
b(i)=b(i)+(b(i+1)-2*b(i)+ba)/4
ba=bb
NEXT i
LABEL sv4
IF ab=3 OR ab=4 THEN GOTO sv5 ELSE GOTO sv6
LABEL sv5
ba=b(0)
b(0)=b(1)
FOR i=1 TO r-2
bb=b(i)
b(i)=b(i)+((2*i+1)*b(i+1)-4*i*b(i)+(2*i-1)*ba)/(8*i)
ba=bb
NEXT i
LABEL sv6
IF ab=5 THEN GOTO sv7 ELSE GOTO sv8
LABEL sv7
ba=b(0)
b(0)=b(0)+(b(1)-b(0))/2
FOR i=1 TO r-2
bb=b(i)
b(i)=b(i)+((2*i-1)*b(i+1)-4*i*b(i)+ba*(2*i+1))/(8*i)
ba=bb
NEXT i
LABEL sv8
RETURN


LABEL grad1
grad=(p*ba/(p+1)-(p+1)*b(r-1)/p+(2*p+1)*bi/(p*(p+1)))/x
b(r-1)=b(r-1)+(b(r-2)/(p+1)-b(r-1)/p+bi/(p*(p+1)))/2
RETURN


LABEL moveinterface
IF ab=1 THEN GOTO vs1 ELSE GOTO vs2
LABEL vs1

dxi=(dz*mb*d1*grad+mc*xi*kc*dcl+dt*(l1-xi)+(mb*(bl-bav)+mc*(cl-cav))*dl)/(bl*mb*
(1-kb)+cl*mc*(1-kc))
dbl=(bl*(1-kb)*dxi-dz*d1*grad-(bl-bav)*dl)/(l1-xi)
dcl=(cl*(1-kc)*dxi-(cl-cav)*dl)/(kc*xi+(l1-xi))

LABEL vs2
IF ab=2 THEN GOTO vs3 ELSE GOTO vs4
LABEL vs3

dxi=(mb*d1*grad*dz+mc*xi*dcl*kc+(1-xi)*w*dz)/(mb*bl*(1-kb)+mc*cl*(1-kc))
dbl=(bl*(1-kb)*dxi-grad*d1*dz)/(1-xi)
dcl=(cl*(1-kc)*dxi)/(kc*xi+(1-xi))

LABEL vs4
```

```
IF ab=3 OR ab=4 THEN GOTO vs5 ELSE GOTO vs6
LABEL vs5

dxi=(mb*d1*grad*dz+mc*(xi/2)*kc*dc1+((1^2-xi^2)/(2*xi))*w*dz)/(mb*b1*(1-kb)+mc*c
1*(1-kc))
db1=(b1*(1-kb)*dxi*xi*2-d1*grad*dz*xi*2)/(1*1-xi*xi)
dc1=(c1*(1-kc)*dxi*2*xi)/(kc*xi*xi+(1*1-xi*xi))

LABEL vs6
IF ab=5 THEN GOTO vs7 ELSE GOTO vs8
LABEL vs7

db1=(b1*(1-kb)*(kc*(1^2-(1-xi)^2)+(1-xi)^2)*dt-mc*c1*(1-kc)*d1*grad*2*(1-xi)*dz)
/(c1*(1-kc)*(1-xi)^2*mc+b1*(1-kb)*(kc*(1^2-(1-xi)^2)+(1-xi)^2)*mb)
dc1=(dt-mb*db1)/mc
dxi=(d1*grad*dz+db1*((1-xi)/2))/(b1*(1-kb))

LABEL vs8
RETURN


LABEL newintercon
xi=xi+dxi
c1=c1+dc1
cs=kc*c1
b1=b1+db1
bi=kb*b1
p=p+dxi/x
gg=FIX(p)-1

FOR j=0 TO gg
b(r+j)=b(r-2)*(1+j)*(1+j-p)/(1+p)+b(r-1)*(2+j)*(p-j-1)/p+bi*(2+j)*(1+j)/(p*(p+1)
)
NEXT j
r=r+gg
p=p-gg
IF ab=1 THEN GOTO ty ELSE GOTO yup
LABEL ty
11=12
1=12
LABEL yup
RETURN

LABEL check
REM
REM  Trapezoidal rule
REM
IF ab=1 OR ab=2 THEN GOTO aaa1 ELSE GOTO aaa2
LABEL aaa1
FOR i=1 TO r
IF b(i)<bav THEN GOTO hus ELSE GOTO ahme
LABEL hus
chc1=chc1+(bav-(b(i)+b(i-1))/2)*(i-(i-1))*x
LABEL ahme
IF b(i)> bav THEN GOTO ali ELSE GOTO veli
LABEL ali
chc2=chc2+((b(i)+b(i-1))/2-bav)*(i-(i-1))*x
LABEL veli
NEXT i
LABEL aaa2

IF ab=3 OR ab=4  THEN GOTO aaa3 ELSE GOTO aaa4

LABEL aaa3
FOR i=1 TO r
IF b(i)<bav THEN GOTO ss1 ELSE GOTO ss2
```

```
LABEL ss1
chc1=chc1+(bav-(b(i)+b(i-1))/2)*((i*x)^2-((i-1)*x)^2)*PI
LABEL ss2
IF b(i)> bav THEN GOTO ss3 ELSE GOTO ss4
LABEL ss3
chc2=chc2+((b(i)+b(i-1))/2-bav)*((i*x)^2-((i-1)*x)^2)*PI
LABEL ss4
NEXT i
LABEL aaa4

IF ab=5 THEN GOTO aaa5 ELSE GOTO aaa6

LABEL aaa5
FOR i=1 TO n
IF b(i) < bav THEN GOTO ddd5 ELSE GOTO ddd6
LABEL ddd5
chc1=chc1+(bav-(b(i)+b(i-1))/2)*((x*(n-i+1))^2-(x*(n-i))^2)*PI
LABEL ddd6
IF b(i) > bav THEN GOTO ddd7 ELSE GOTO ddd8
LABEL ddd7
chc2=chc2+((b(i)+b(i-1))/2-bav)*((x*(n-i+1))^2-(x*(n-i))^2)*PI
LABEL ddd8
NEXT i
LABEL aaa6

PRINT chc1,chc2,chc1/chc2

RETURN


LABEL  homogen

INPUT " Cooling rate  as  C/sec. for solid-state (-)     ",w1
INPUT " Temperature   as C                               ",t1

REPEAT

GOSUB gon

UNTIL  t =< t1

RETURN



LABEL gon
d1=do*EXP(-q/(1.986*(273+t)))
dz=x^2/(4*d1)
z=z+dz
IF  yy1=1 THEN GOTO sel1 ELSE GOTO sel2
LABEL sel2
dt=w1*dz
t=t+dt
LABEL sel1
bc=b(r-1)
ba=b(0)
IF ab=1 OR ab=2 THEN GOTO ert1 ELSE GOTO ertu
LABEL ert1
b(0)=(b(0)+b(1))/2
FOR i=1 TO r-1
bb=b(i)
b(i)=b(i)+(b(i+1)-2*b(i)+ba)/4
ba=bb
NEXT i
b(r)=(b(r)+bc)/2
```

```
LABEL ertu
IF ab=3 OR ab=4 THEN GOTO ertug ELSE GOTO ertugr
LABEL ertug
b(0)=b(1)
FOR i=1 TO r-1
bb=b(i)
b(i)=b(i)+((2*i+1)*b(i+1)-4*i*b(i)+ba*(2*i-1))/(8*i)
ba=bb
NEXT i
b(r)=(b(r)+bc)/2
LABEL ertugr
IF ab=5 THEN GOTO ertugru ELSE GOTO ertugrul
LABEL ertugru
b(0)=(b(1)+b(0))/2
FOR i=1 TO r-1
bb=b(i)
b(i)=b(i)+((2*i-1)*b(i+1)-4*i*b(i)+ba*(2*i+1))/(8*i)
ba=bb
NEXT i
b(r)=bc
LABEL ertugrul

RETURN



LABEL homogen1
INPUT " Homogenization time   as hour       ",zaman
INPUT " Homogenization temperature as C      ",tr
zam=zaman*60*60
z=0
t=tr
REPEAT

GOSUB gon

UNTIL z >= zam

RETURN


LABEL segratio
IF yy1=1 THEN GOTO eee1 ELSE GOTO eee2
LABEL eee2
bmax=b(r)
bmin=b(0)
s=bmax/bmin
PRINT " Seg. Ratio of Mn    ",s
PRINT " Bmax.      % Mn          ",bmax
PRINT " Bmin.      % Mn          ",bmin
LABEL eee1
IF yy1=1 THEN GOTO kkk1 ELSE GOTO kkk2
LABEL kkk1
bmax2=b(r)
bmin2=b(0)
PRINT " Bmax after hom.     % Mn     ",bmax2
PRINT " Bmin after hom.     % Mn     ",bmin2
resegin=(bmax2-bmin2)/(bmax-bmin)
PRINT " Residual Segregation index     ",resegin
LABEL kkk2

RETURN
```

APPENDIX – 2

A_c = area of circle = πr^2

A_h = area of hexagon = $\frac{h\,r}{2}\,6 = \frac{\frac{2\,r}{\sqrt{3}}\,r}{2}\,6 = \frac{6\,r^2}{\sqrt{3}}$

$h^2 = r^2 + (\frac{h}{r})^2 \quad \Rightarrow \quad h = \frac{2\,r}{\sqrt{3}}$

$$\frac{Ah}{Ac} = \frac{\frac{6\,r^2}{\sqrt{3}}}{\pi\,r^2} = \frac{6}{\pi\sqrt{3}} = 1.1026$$

A_h (area of hexagon) = A_c' (area of new circle) = $\pi\ K^2$

$$\frac{Ah}{Ac} = \frac{Ac'}{Ac} = \frac{\pi K^2}{\pi r^2} = 1.1026 \quad \Rightarrow \quad \underline{\underline{K = 1.05\ r}}$$

K radius of new circle

The radius of new circle (half primary arm spacing) should be 1.05 times higher than the radius of circle (measured half primary arm spacing)

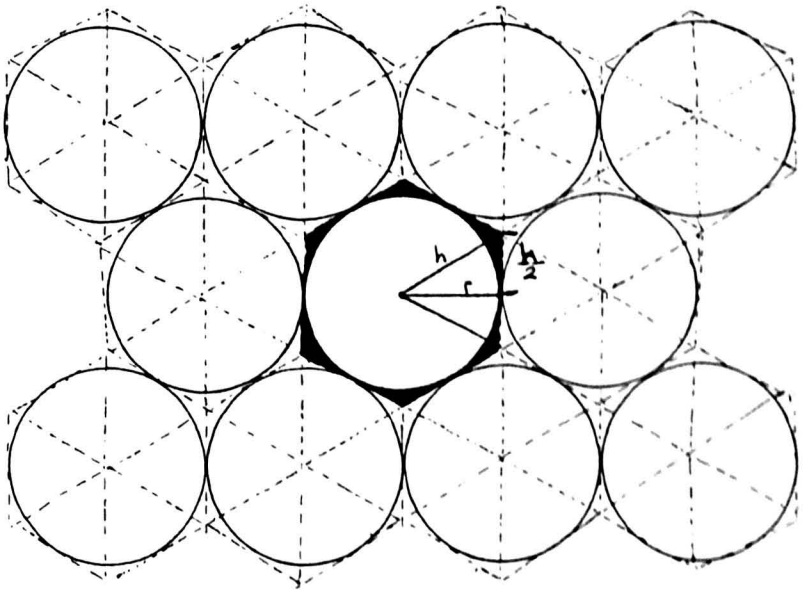

REFERENCES

1. Volmer, M. and Weber, A., Z. Phys. Chem., 1926, 119, 227
2. Becker, R. and Doring, W., Ann. Phys., 1935, 24, 719
3. Turnbull, D. and Fisher, J.C., J. Chem. Phys., 1949, 17, 71
4. Prepezko, J.H. Proc. Conf. ' Solidification and Casting of Metals', Sheffield, 1976, Met. Soc. P 169, London
5. Reed-Hill, R.E., Physical Metallurgy Principles, D.Van Nostrand Company, 1973
6. Jackson, K., Uhlmann, D. and Hunt J., J. Crystal Growth, 1967, 1, 1.
7. Kurz, W. and Fisher, D.J., Fundamentals of Solidification, Trans Tech Publications, 1986
8. Tiller, W.A., Rutter, J.W., Jackson, K.A. and Chalmers, B., Acta Met., 1953, 1, 428
9. Mullins, W.W. and Sekerka, R.F., J. Applied Physics, 1963, 34, 323
10. Mullins, W.W. and Sekerka, R.F., J. Applied Physics, 1964, 35, 444
11. Eshelman, M.A. and Trivedi, R. Acta Metall. 1987, 35, 2443
12. Ivantrov, G.P., Dockl. Akad. Nauk SSSR, 1947, 58, 567
13. Horvay, G. and Cahn, J.W., Acta Metall., 1961, 9, 693
14. Zener, C., Trans. Met. Soc. A.I.M.E., 1946, 167, 550
15. Hillert, M., Metall. Trans. 1975, 6A, 5
16. Huang, S.C. and Glicksman, M.E., Acta Metall., 1981, 29, 701
17. Glicksman, M.E. and Schaeffer, R.J., J. Cryst. Growth, 1967, 1, 297
18. Nash, G.E. and Glicksman, M.E., Acta Metall., 1974, 22, 1283

19. Temkin, D.E., Dokl. Akad. Nauk SSSR, 1969, 132, 1307

20. Oldfield, W., Mater. Sci. Eng., 1973, 11, 211

21. Langer, J.S. and Muller-Krumbhaar H., Acta Metall., 1978, 26, 1681

22. Lipton, J., Glicksman, M.E. and Kurz, W., Metal. Trans., 1987, 18A, 341

23. Lipton, J., Glicksman, M.E. and Kurz, W., Sci. Mater. Eng., 1984, 65, 57

24. Chopra, M.A., Glicksman, M.E. and Singh, N.B., Metal. Trans., 1988, 3087

25. Bower, T.F., Brody, H.D. and Flemings, M.C., Trans. AIME, 1966, 236, 624

26. Burden, M.H. and Hunt, J.D., J. Cryst. Growth, 1974, 22, 109

27. Laxmanan, V., Materials Sciences Under Microgravity, 1984, Nov. 5-7, 403

28. Trivedi, R., Metal. Trans., 1984, 15A, 977

29. Trivedi, R., J. Cryst. Growth, 1980, 49, 219

30. Somboonsuk, K., Mason, J.T. and Trivedi, R., Metall. Trans., 1984, 15A, 967

31. Kurz. W. and Fisher, D.J., Acta Metall., 1981, 29, 11

32. Laxmanan, V., Acta Metall., 1985, 33, 1023

33. Laxmanan, V., Acta Metall., 1985, 33, 1037

34. Jin, I. and Purdy, G.R., J. Cryst. Growth, 1974, 23, 29

35. Kirkdaldy, J.S., Scr. Metall, 1980, 14, 739

36. Hunt, J.D., Proc. Conf. 'Solidification and Casting of Metals', Sheffield, 1977, Metals Soc., London, 1979

37. Chalmers, B. 'Principles of Solidification', John Wiley and Sons, New York, 1964

38. Mason, J.T., Verhoeven, J.D. and Trivedi, R., Metall. Trans. 1984, 15A, 1165

39. Claren, C.M., Verhoeven, J.D. and Trivedi, R., Metall. Trans., 1980, 11A, 1853

40. Mason, J.T., Verhoeven, J.D. and Trivedi, R., J.Cryst. Growth, 1982, 59, 516

41. McCarney, D.G. Hunt, D.J., Acta Metall., 1981, 29, 1851

42. Young, K.P. and Kirkwood, D.H., Met. Trans., 1975, 6A, 197

43. Suzuki, A. and Nagoaka, Y., J. Japan Inst. Met, 1969, 33, 658

44. Rickinson, B.A., Ph.D. Thesis, Sheffield, 1975

45. Bunden, M.H., Hebditch, D.J. and Hunt, J.D., J. Cryst. Growth, 1972, 20, 121

46. Jacobi, H. and Schwerdtfeger, K., Met. Trans., 1976, 7A, 811

47. Taha, M.A., Jacobi, H., Imagumtai, M. and Schwerdtfeger, K., Met. Trans., 13A, 1982, 2131

48. Edvardsson, T., Fredriksson, H. and Svensson, I., Metal Science, 1976, , 10, 298

49. Botas, J.D.F.P., Ph.D. Thesis, Sheffield, 1982

50. Tewari, S.N., Metall. Trans., 1986, 17A, 2279

51. Flemings, M.C., ' Solidification Processing ', McGraw-Hill, New York, 1974

52. Howarth, J.A. and Mondolfo, L.F., Acta Met., 1962, 10, 1037

53. Kattamis, T.Z., Coughlin, J.C. and Flemings, M.C., Trans. Metall. AIME., 1967, 239, 1504

54. Suzuki, A., Suzuki, T., Nagaoka, Y. and Iwata, Y., J. Japan Inst. of Metals, 1968, 1301

55. Okamoto, T., Matsuo, S. and Kishitake, K., Trans. ISIJ, 1978, 18, 289

56. Rickinson, B.A. and Kirkwood, D.H., Proc. Conf. 'Solidification and Casting of Metals', Sheffield, 1977, Met Soc., 1979

57. Ogilvy, A.J.W., Ph.D. Thesis, Sheffield, 1983

58. Kahlweit, M., Scr. Metall., 1968, 2, 251

59. Mortensen, A., Cornie, J.A. and Flemings, M.C., Metall. Trans., 1988, 19A, 709

60. Kirkwood, D.H., Mater. Sci. Eng., 1985, 73, L1

61. Feurer, U. and Wunderlin, R., DGM Fachber, 38, 1977 (Duetche Gesellschaft fur Metallkunde, Oberursel) Kurz, W. and Fisher, D.J. 'Fundamentals of Solidification', Trans Tech Publications, 1984, App. 8

62. Pfann, W.G., Trans. Met. Soc. A.I.M.E., 203, 961

63. Martin, J.W. and Doherty, R.D., 'Stability of Microstructure in Metallic Systems', Cambridge Uni. Press, 1980

64. Allen, D.J. and Hunt, J.D., Met. Trans. 1976, 7A, 767

65. Allen, D.J. and Hunt, J.D., Proc. Conf. 'Solidification and Casting of Metals', Sheffield, 1977, Met. Soc., London, 1979

66. Mortensen, A., Met. Trans., 1989, 20A, 247

67. Cadoff, L.H. and Brody, H.D., University of Pittsburgh, 1988, Unpublished reserch , Private comminication

68. Micheal, A.B. and Bewer, M.B. Trans. Met. Soc. AIME, 1954, 200, 47

69. Bennett, D.A., Ph.D. Thesis, Sheffield, 1978

70. Lavender, J.D. and Jones, F.W., J.I.S.I., 1949, September,14

71. Turkdogan, E.T. and Grande, R.A., J.I.S.I., 1969, May, 482

72. Finniston, H.M. and Fearnehough, T.D., J.I.S.I., 1951, Semtember, 5

73. Flemings, M.C., Poirier, D.R., Baroni, R.V. and Brody, H.D., J.I.S.I, 1970, 208, 371

74. Brody, H.D. and Flemings, M.C., Trans. Met. Soc. AIME, 1966, 236, 615

75. Burton, J.A., Primm, R.C. and Slichter, W.P., J. Chem. Phys., 1953, 21, 1987

76. Bolling, G.F. and Tiller, W.A., J. App. Phy., 1961, 32, 2587

77. Kohn, A. and Philibert, J., Mem. Sci. Rev., 57, 291

78. Doherty, R.D. and Melford, D.A., J.I.S.I., 1966, 204, 1131

79. Subramanian, S.V., Haworth, C.W. and Kirkwood, D.H., J.I.S.I., 1968, 206, 1027

80. Ogilvy, A.J.W., Ostrowski, A. and Kirkwood, D.H., Met. Sci., 1980, April, 168

81. Kagawa, A., Iwata, K., Nofal, A.A. and Okamoto, T., Mat. Sci. and Tec., 1985, 1, 678

82. Morita, Z. and Tanaka, T., Trans. ISIJ., 1983, 23, 824

83. Morita, Z. and Tanaka, T., Trans. ISIJ, 1984, 207

84. Kagawa, A., Moriyama, S. and Okamoto, T., J. Mat. Sci., 1982, 17, 135

85. Kagawa, A. and Okamoto, T., J. Mat. Sci., 1984, 19, 2306

86. Sigworth, G.K. and Elliott, J.F., Metal Science, 1974, 8, 298

87. Bastow, B.D. and Kirkwood, D.H., J.I.M., 1971, 99, 277

88. Rickinson, B.A. and Kirkwood, D.H., Metal Science, 1978, 12, 138

89. Gulliver, G.H., J. Inst. Met., 1913, 9, 120

90. Schiel, E., Z. Metallkunde., 1942, 34, 70

91. Clyne, T.W. and Kurz, W., Trans. AIME, 1981, 12A, 965

92. Ohnaka, I., Trans. ISIJ, 1986, 26, 1045

93. Kobayashi, S., Trans. ISIJ., 1988, 28, 729

94. Kobayashi, S., J. Crystal Growth, 1988, 88, 87

95. Kobayashi, S., Trans. ISIJ., 1988, 28, 535

96. Rohatgi, P.K. and Adams, C.M., Trans. Met. Soc. AIME, 1967, 239, 1737

97. Allen, D.J. and Hunt, J.D., Met. Trans., 1979, 10A, 1389

98. Solari, M. and Biloni, H., J. Crystal Growth, 1980, 49, 451

99. Kirkwood, D.H., Mat. Sci and Eng., 1984, 65(1), 101

100. Kirkwood D.H. and Evans, D.J., Conf on 'Solidification of Metals', ISI, 1968, P 110, 108

101. Schwerdtfeger, K., Arch. Eisenhut., 1970, 9, 923

102. Ueshima, Y., Mizoguchi, S., Matsumiya, T. and Kajioka, H., Met. Trans. 1986, 17A, 845

103. Marsumiya, T., Kajioka, H., Mizoguchi, S., Ueshima, Y. and Esaka, H., Trans. ISIJ, 1984, 24, 873

104. Mizoguchi, S., Ueshima, Y., Matsumiya, T. and Kajioka, H., Conf. on 'Solidification Processing 1987', Inst. of Metals, P 421, 1988, 75

105. Kobayashi, S., Tomono, H. and Gunji, K., Trans. ISIJ., 1988, 28, 215

106. Kobayashi, S., Nagamichi, T. and Gunji., Trans. ISIJ., 1988, 28, 543

107. Clyne, T.W., Metal Science, 1982, 16, 441

108. Cornelissen, M.C.M., Ironmaking and Steelmaking, 1986, 13(4), 204

109. Battle, T.P. and Pehlke, R.D., Conf. on 'Solidification Processing 1987', Inst of Metals, P 421, 1988, 71

110. Feest, E.A. and Doherty, R.D., Met. Trans., 1973, 4, 115

111. Doherty, R.D., Feest, E.A. and Holm, K., Met. Trans., 1973, 4, 120

112. Basaran, M., Met. Trans., 1981, 12A, 1235

113. Ogilvy, A.J.W and Kirkwood, D.H., App. Scie. Res., 1987, 44, 45

114. Howe, A.A. and Kirkwood, D.H., Conf. on 'Solidification Processing 1987', Inst. of Metals, London, P 421, 1988, 63

115. Howe, A.A., App. Scie. res., 1987, 44, 51

116. Roosz, A., Simon, M. and Exner, H.E., Conf. on 'Solidification Processing 1987', Inst. of Metals, P 421, 1988, 59

117. Halder, E., Roosz, A., Exner, H.E. and Fishmeister, H.F., Met. Sci. For., 1987, 13/14, 547

118. Roosz, A., Halder, E. and Exner, H.E., Met. Sci., 1985, 1, 1057

119. Roosz, A., Halder, E. and Exner, H.E., Met. Sci., 1986, 2, 1149

120. Miettinen, J., Conf. on 'Solidification Processing 1987', Inst. of Metals, P 421, 1988, 67

121. Miettinen, J., Scan. J. Metall., 1988, 17, 218

122. Lalli, L.A., 'Modelling of Casting and Welding Processes', Brody, H.D. and Apelian., publication of AIME, 425

123. Elliot, J.F. and Gleiser, M., 'Thermochemistry for Steelmaking', Addison Wesley Vol. 1, 1960

124. Benz, M. and Elliot, J.F., Trans. AIME, 1961, 221, 323

125. Buckley, R.A. and Hume-Rothery, W., JISI, 1960, 196, 403

126. Chipman, J., Met. Trans. 1972, 3, 55

127. Hellawell, A., 'The equilibrium diagram of the system iron and manganese', 1956, London, The institute of Metals

128. Benz, R., Elliot, J.F. and Chipman, J., Met. Trans., 1973, 4, 1449

129. Schurmann, E. and Geissler, I.K., Geissereiforschung, 1977, 29, 153

130. Schenck, S., Frohberg, M.G. and Steinmetz, E., Arch. Eisenhut., 1963, 34, 37

131. Vogel, R. and Doring, W., Arch. Eisenhut., 1935, 9, 247

132. Sshidtmann, E. and Rakoski, F., Ach. Eisenhut., 1983, 54, 357

133. Kerr, H.W., Cisse, J. and Bolling, G.F., Acta Metal., 1974, 22, 677

134. Metals Handbook, Vol. 15, 9 edition, 125

135. Boettinger, W.J., Met. Trans., 1974, 5, 2023

136. Brody, H.D. and David, S.A., Proc. Conf. 'Solidification and Casting of Metals', Sheffield, 1977, Met. Soc., London, 1979, 144

137. Ostrowski, A. and Langer, E.W., Proc. Conf. 'Solidification and Casting of Metals', Sheffield, 1977, Met. Soc., London, 1979,139

138. Bibby, P.A. and Beech, J., J.I.S.I., 1973, April, 290

139. Kohn, A., Mem. Sci. Rev. Met., 1960, 57, 291

140. Fredriksson, H., Scan. J. Metall., 1976, 5, 27

141. Fredriksson, H., Met. Sci., 1976, 11, 77

142. Fredriksson, H., Met. Sci., 1982, 16, 575

143. Fredriksson, H. and Nylen, T., Met. Sci., 1982, 16, 283

144. Chadwick, G.A., Conf on ' Solidification Technology in the Foundary and Cast House', Warwick, 1980, Met. Soc., 207

145. Rutter, J.W. and Chalmers, B., Can. J. Phys., 1953, 31, 15

146. Clyne, T.W., J. Crystal Growth, 1980, 50, 684

147. Clyne, T.W., J. Crystal Growth, 1980, 50, 691

148. Naumann, R.J., J. Crystal Growth, 1982, 58, 569

149. Naumann, R.J., J. Crystal Growth, 1982, 58, 571

150. El Mahallawy, N.A., Aluminium, 1980, 56(3), 224

151. Shpigler and Beraha, 'Colour Metallography', Ame. Soc. for Metal, 1977

152. Haworth, C.W. and Horsfield, J., Private Communication

153. Clayton, D.B., Smith, T.B. and Brown, J.R., J.I.S.I., 1961, 90, 62

154. Crank, J., Quart. J. Mech. App. Math., 1957, 220

155. Kattamis, T.Z. and Flemings, M.C., Met. Trans. AIME, 1965, 233, 993

156. Young, K.P., Ph.D. Thesis, Sheffield, 1972

157. Swedish Institute for Metal Research,'A guide to the solidification of steels', Jernkontorent, Stockholm, 1977

158. Hammer, O. and Grunbaum, G., Scan. J. Metall., 1974, 3, 11

159. Eruslu, M.N., Ph.D. Thesis, Sheffield, 1976

160. Nayal, M.G.E., M. Met. Thesis, Sheffield, 1982

161. Weinberg, F. and Teghtsoonian, E., Met. Trans., 1972, 3, 93

162. Fredriksson, H. and Hellner, L., Scan. J. Metall., 1974, 3, 61

163. Shurmann, E., Baumgartl, S., Nedeljkovic, L. and Tripkovic, M. Steel Research, 1987, 49

164. Schmidt, L. and Fredriksson, H., Ironmaking and Steelmaking, 1975, 1, 61

165. Haworth, C.W., Private Comminication

166. Crank, J., 'Moving Boundary Problems in Heat Flow and Diffusion', Oxford Press, 1975, 192

167. Crank, J., 'Mathematics of Duffusion', Oxford Press, 1964

168. Jacbi, H. ' Casting and Solidification of Steel', ECSC Luxembourg, 1977, 90

169. Battle, T.P. and Pehlke, R.D., Met. Trans., 1989, 20A, 149

170. Metal handbook, Vol 6 , 8 edition

171. Gieger, G.H. and Poirier, Poirier, D.R., 'Transport Phenomena in Metallurgy', 1973, Addison-Wesley, New York

ACKNOWLEDGEMENTS

I would like to extend my sincere gratitude to my supervisor, Dr D.H. Kirkwood, for his encouragement, suggestions and the stimulating discussions throughout the course of this work.

I am indebted to Dr C.H. Haworth for all his help and advice with regard to the electron probe microanalysis and his personal efforts for obtaining the colour concentration maps through British Steel Co. Swindon Lab.

I am grateful to British Steel Co. Swindon Lab. for providing the colour concentration maps.

I would like to thank Prof. B.B. Argent, Prof. G.W. Greenwood, Prof. C.M. Sellars and Prof. H. Jones for the provision of laboratory facilities.

I am indebted to the members of technical staff for their invaluable assistance.

I am grateful to Dr V.S. Gallardo for his useful suggestions and help with Photography, to A.Z Nazir for his help and support with Electron Probe Microanalysis, to A. Howe for his useful discussions, to A. Karavokyris for his many useful comments and discussions.

Finally, I am indebted to thank the Turkish Government's Ministry of Education for the award of the grant to fund the above work.

TABLE - 1
Chemical Composition of Alloys

Cast No	Element	Amount %	Accuracy %	Method
6196	C	0.1	∓ 0.01	Leco
	Mn	1.57	∓ 0.02	Quan.
	S	0.003	∓0.001	Leco
	P	0.005		Quan.
	Other	<0.02		Quan.
6196	C	0.21	∓ 0.01	Leco
	Mn	1.6	∓ 0.02	Quan.
	S	0.003	∓ 0.001	Leco
	P	0.005		Quan.
	Other	<0.02		Quan.
6196	C	1	∓ 0.01	Leco
	Mn	1.58	∓0.02	Quan.
	S	0.003	∓0.001	Leco
	P	0.005		Quan.
	Other	< 0.02		Quan.
6513	C	0.75	∓ 0.01	Leco
	Mn	1.59	∓0.02	Quan.
	S	0.003	∓0.001	Leco
	P	0.005		Quan.
	Other	< 0.02		Quan.

TABLE 2
Temperature gradients and cooling rates in the calibration specimen as a function of growth rate for three series

Series KW	Growth rate mm/min	Gradient C/mm in liquid	in liq+sol	in solid	Cooling rates C/sec in liq+sol	in solid
1.9	1.5	8.4	10.2	11.4	0.25	0.28
	6	5.5	9	9.8	0.9	0.98
	15	4.8	7.4	8.1	1.85	2.02
	30	3.5	6.5	7.2	3.25	3.6
2.2	1.5	10.7	12	12.3	0.3	0.31
	6	7.2	10.5	11.1	1.05	1.11
	15	5.9	9	9.3	2.25	2.3
	30	4.6	7.4	7.8	3.7	3.9
2.4	1.5	13.2	15.6	15.8	0.39	0.4
	6	9.8	11.3	12	1.13	1.2
	15	7.6	9.2	9.9	2.3	2.48
	30	6.9	8.3	8.9	4.15	4.45

TABLE 3
Results of Primary Arm Spacing

Carbon content	Growth rate mm/min	Primary arm spacing (micron) 1 Series low λ_1'	λ_1''	2 Series middle λ_1'	λ_1''	3 Series high λ_1'	λ_1''
0.8	1.5	380	356			234	265
	6	315	345	265	285	204	230
	15	274	290	235	248	175	210
	30	230	255			140	158
0.4	1.5			279	293	248	257
	6			249	268	195	218
	15			210	236	185	184
	30			190	204	174	194
0.2	15	340	367			217	230
	6	289	296	215	238	210	225
	15	240	265	190	213	184	176
	30	208	234	174	185	161	174
0.1	1.5	304	319	256	260	232	223
	6	250	255	237	255	200	217
	15	196	216	172	198	153	168
	30						

TABLE 4
Results of Secondary Arm Spacing $\lambda_2 = At^n$

Carbon content	Growth rate mm/min	Series 1 Const	Exp.	2 Const	Exp.	3 Const	Exp.
0.1	1.5	25.4	0.38	13.2	0.48		
	6	25.8	0.33	18.1	0.31		
	15	18.8	0.43	12.8	0.38		
	30						
0.2	1.5	13.1	0.45			10.3	0.4
	6	9.6	0.56	14.3	0.38	13	0.36
	15	9.5	0.5	11	0.4	11.2	0.32
	30	6.1	0.58	7.6	0.37	8.1	0.38
0.4	1.5			8.1	0.42	9.2	0.47
	6			9.2	0.48	5.7	0.5
	15			5.6	0.52	7.6	0.44
	30			8.5	0.44	6.3	0.46
0.8	1.5	12.6	0.41			6.4	0.45
	6	9.1	0.52	8.8	0.42	7.6	0.41
	15	5.9	0.58	6.4	0.44	6.5	0.46
	30	6.1	0.57			5.2	0.49

TABLE 5-a
Experimental Results of 0.1 % C - 1.60 % Mn

Series	Growth rate mm/min		Distance mm	Temp. C	Between secon. Cmin	Between secon. Cmax	Between prim. Cmin	Between prim. Cmax
1	1.5		1	1510	1.42	1.85		
			2	1500	1.48	1.67		
			5	1470	1.56	1.65		
			7	1445	1.55	1.55	1.5	1.8
		T	7	1445			1.42	1.72
							1.44	1.9
							1.42	1.88
		M	12	1370			1.44	1.73
								1.72
								1.68
	6		2	1500	1.42	1.82		
			3.5	1490	1.47	1.75		
			5	1470	1.5	1.65		
			10	1425			1.5	1.86
								2.21
			24	1280			1.47	1.7
		T	27	1260			1.44	1.74
							1.45	1.77
								1.74
	15		0.5	1515	1.35	1.9	1.34	2.24
			1	1512	1.37	1.75		1.72
			1.5	1509	1.39	1.68		2.53
			3	1498	1.49	1.69		
			5	1480			1.42	1.91
			7	1465			1.42	2.18
								1.81
			15	1400			1.44	1.8
		T	26	1300			1.45	1.98
							1.46	1.82
								1.87
								1.69
								1.72

T taken from tranverse sections
M taken from map

TABLE 5-b
Experimental Results of 0.1 % C - 1.60 % Mn

Series	Growth rate mm/min	Distance mm		Temp. C	Between secon. Cmin	Between secon. Cmax	Between prim. Cmin	Between prim. Cmax
2	1.5	0.5		1515	1.39	1.82	1.37	2.55
		1		1510	1.48	1.66	1.39	2.65
		3		1488			1.42	1.91
								1.93
		6		1450			1.44	1.78
		15		1330			1.44	1.86
								1.74
			T	25	1220			1.46	1.77
							1.47	1.78
								1.74
								1.68
	6	1		1510	1.37	1.78		
		2		1500	1.43	1.76	0.38	2.3
		3.5		1485			1.41	2.42
		4.5		1470			1.42	1.98
		7		1440			1.43	1.95
								1.81
		23		1265			1.44	1.72
								2.01
			T	20	1300			1.44	1.96
							1.45	1.87
								1.82
								2.2
	15	0.5		1515	1.41	1.9	1.39	1.91
		1		1512	1.48	1.7	1.41	2.23
		1.5		1505			1.42	1.98
		3		1490			1.43	1.92
								1.9
		4		1480			1.45	
		8		1440			1.44	1.79
		15		1370			1.45	1.84
		20		1320			1.45	1.8
								1.78
								1.83
			T	28	1240			1.46	1.66
							1.47	1.68
								2.1
								1.96
								1.87

TABLE 5-c
Experimental Results of 0.1 % C - 1.60 % Mn

Series	Growth rate mm/min	Distance mm		Temp. C	Between secon. Cmin	Between secon. Cmax	Between prim. Cmin	Between prim. Cmax
3	1.5		1	1510	1.34		1.33	1.87
			2	1490	1.49	1.69	1.41	2.87
			3	1475			1.42	2.2
								2.42
			7	1410			1.44	1.77
			24	1200			1.48	1.74
								1.84
		T	24	1200			1.46	1.74
							1.48	1.68
								1.8
								1.83
	6		0.5	1515	1.36	1.91	1.33	2.07
								1.98
			1	1510	1.41	1.84	1.41	1.82
								1.97
			2	1500	1.53		1.44	2.03
			4.5	1470			1.44	1.8
								2.01
			8	1430			1.46	1.87
			26	1270			1.47	1.88
								1.74
		T	28	1250			1.45	1.78
							1.46	1.74
								1.66
								1.67
	15		1	1510	1.36	1.85	1.35	2.03
			2	1500	1.4	1.95	1.39	3.04
			3	1485			1.44	2.64
			5	1470			1.44	1.95
			7	1450			1.45	2.01
			9	1410			1.48	2.08
			15	1370			1.48	1.93
								1.82
		T	26	1270			1.46	1.9
							1.45	1.82
								1.82
								1.77
								1.78

TABLE 6-a
Experimental Results of 0.2 % C - 1.6 % Mn

Series	Growth rate mm/min	Distance mm	Temp. C	Between secon. Cmin	Between secon. Cmax	Between prim. Cmin	Between prim. Cmax
1	1.5	1	1500	1.41	1.85		
		5	1460	1.45	1.65		
		10	1405	1.5	1.66		
		13.5	1355			1.45	1.96
		T 25	1225			1.44	1.98
							2.06
	6	2	1480	1.42	1.92		
		3.5	1470	1.4	1.85		
		6	1450	1.45	1.9		
		9	1420	1.45	1.9		
		14	1370	1.46	1.7		
		20	1310			1.45	2.01
		T 23	1285			1.44	2.01
							2.15
	15	3	1490	1.41	1.72		
		7	1460	1.43	2.1		
		12	1410	1.45	1.74	1.45	2.24
		17	1370			1.45	1.97
							1.89
							2.1
		T 27	1260			1.45	2.06
							1.97
							1.89
							2.1
	30	4	1485	1.4	1.78		
		9	1450	1.42	1.95		
		13.5	1410	1.42	1.92		
		17	1390			1.45	2.03
		20	1360			1.42	2.13
		T 24	1330			1.42	2.14
							2.09
							2.11

TABLE 6-b
Experimental Results of 0.2 % C - 1.6 % Mn

Series	Growth rate mm/min	Distance mm	Temp. C	Between secon. Cmin	Between secon. Cmax	Between prim. Cmin	Between prim. Cmax
2	6	2	1490	1.34	1.78		
		4	1470	1.36	1.96		
		6	1445	1.38	1.86		
		12	1380	1.41	1.72		
					1.76		
		22	1270	1.42	1.68	1.41	2.06
		T 21	1275			1.41	2.22
						1.42	2.18
							2.3
							1.99
	15	2	1490	1.32	1.78		
		6	1455	1.36	2.55		
		10	1410	1.39	2.08		
		17	1340	1.4	1.96		
					1.87		
		T 26	1270			1.41	2.04
							2.18
							1.98
	30	2	1495	1.32	2.47		
		4	1480	1.35	2.3		
		7	1460	1.4	1.98		
		12	1415	1.41	2.04		
		17	1370	1.42	1.93	1.41	2.17
					1.98	1.41	2.08
		T 27	1320			1.42	2.31
							2.14
							2.09

TABLE 6-c
Experimental Results of 0.2 % C - 1.6 % Mn

Series	Growth rate mm/min	Distance mm	Temp. C	Between secon. Cmin	Between secon. Cmax	Between prim. Cmin	Between prim. Cmax
2	1.5	0.5	1500	1.35	2.09	1.35	1.95
		1.5	1485	1.38	2.3		2.35
		3	1460	1.4	2.06		2.31
		5	1430	1.41	1.86		2.88
		15	1270			1.41	1.91
		26	1100			1.41	1.83
		T 25	1120			1.41	1.84
							1.96
							2.04
	6	1	1500	1.35	2.1		
		2	1490	1.39	2.3	1.39	2.4
		3.5	1470	1.4	1.98		
		10	1390	1.46	1.7		
		18	1300			1.4	2.08
		20	1270			1.41	2.14
		T 26	1200			1.42	1.98
							2.19
							2.24
							1.97
	15	0.5	1505	1.34	1.79		
		1.5	1495	1.37	1.75		1.9
		2.5	1485		1.84		2.38
		5	1460				2.06
		7	1440	1.4	1.76	1.4	2.18
		12	1390	1.41	1.74	1.41	2.28
		20	1310			1.41	1.93
		T 22	1290			1.41	1.98
							2.18
							2.06
	30	1	1500	13	2.16		
		3	1485	1.36	2.3		
		6	1455	1.39	1.97		
		12	1400	1.41	1.87	1.41	2.06
		19	1340	1.42	1.74	1.41	2.19
		T 27	1270			1.41	1.97
							2.19
							2.06
							2.13

TABLE 7-b
Experimental Results of 0.4 % C - 1.6 % Mn

Series	Growth rate mm/min	Distance mm	Temp. C	Between secon. Cmin	Between secon. Cmax	Between prim. Cmin	Between prim. Cmax
2	1.5	1	1480	1.27	1.97		
		3	1455	1.28	1.86		
		6	1415	1.3	1.67		
		25	1180			1.31	2.19
		T 24	1200			1.31	2.18
	6	1	1480	1.26	1.78		
		2.5	1465	1.27	2.06		
		6	1430	1.27	2.47	1.27	2.41
		9	1390	1.29	2.14		
		15	1325	1.3	1.99		
		21	1255	1.31	1.86	1.3	2.32
		T 26	1270			1.3	2.34
							2.27
	15	1	1480	1.26	1.6		2.14
		3	146	1.29	2.34	1.29	2.8
		5	1445	1.31	2.41		
		12	1380	1.34	1.89		
		24	1265	1.33	1.97	1.3	2.29
		T 24	1265			1.29	2.74
							2.48
							2.37
	30	1	1485	1.25	1.78		
		4	1460	1.28	2.57		
		7	1435	1.29	2.12		
		15	1370	1.31	1.97		
		22	1315	1.32	1.92	1.29	2.62
		T 23	1310			1.29	2.17
							2.48
							2.54

TABLE 7-c
Experimental Results of 0.4 % C - 1.6 % Mn

Series	Growth rate mm/min		Distance mm	Temp. C	Between secon. Cmin	Between secon. Cmax	Between prim. Cmin	Between prim. Cmax
3	1.5		1	1475	1.28	1.98		
			2.5	1450	1.29	2.18		
			4	1430	1.3	1.79		
			7	1380	1.36	1.71		
			21	1160			1.34	2.34
		T	23	1130			1.34	2.34
								2.06
	6		0.5	1485	1.27	1.47		
			2	1470	1.28	2.31		
			5	1435	1.28	2.41		
			10	1375	1.3	2.12	1.29	
			15.5	1305	1.32	1.98		
			21	1240	1.32	1.85	1.3	
		T	26	1180			1.31	2.47
								1.99
								2.17
								2.32
	15		1	1480	1.27	1.74		
			4.5	1445	1.28	1.98		
			8	1410	1.28	2.19		
			11.5	1375	1.3	2.04		
			19	1300	1.31	1.98	1.29	2.41
		T	24	1265			1.29	2.69
								2.43
								2.36
								2.21
	30		2	1475	1.25	1.79		
			5	1450	1.26	2.13		
			8	1425	1.26	2.19		
			14	1365	1.29	1.97		
			23	1285	1.31	1.86	1.3	2.67
		T	21	1305			1.3	2.19
								2.67
								2.54
								2.32

TABLE 8-a-b
Experimental Results of 0.8 % C - 1.6 % Mn

Series	Growth rate mm/min	Distance mm	Temp. C	Between secon. Cmin	Between secon. Cmax	Between prim. Cmin	Between prim. Cmax
1	1.5	1	1460	1.26	1.69		
		2	1450	1.32	1.89		1.19
		4	1430	1.45	2.13		
		6	1400	1.47	2.23		2.45
		26	1175			1.28	2.02
		T				1.29	2.7
							1.9
							3.37
	6	2	1450	1.26	1.78		
		5	1425	1.25	2.06		
		15.5	1320	1.27	1.87	1.28	2.41
		T				1.28	2.42
							2.92
	15	3	1450	1.25	1.56		
		5.5	1430	1.26	2.03		
		8	1410	1.26	2.19		
		13	1380	1.29	2.1		
		18	1325	1.31	1.96	1.29	2.26
		T				1.29	2.8
							2.85
	30	6.5	1450	1.25	1.56		
		15.5	1370	1.26	2.03		
		19.5	1340	1.29	2.19		
		26.5	1280	1.31	1.96	1.29	2.26
		T				1.28	2.48
							3.02
							2.78
2	6	19	1260	1.35	1.92		
		T				1.28	3.02
							3.12
							2.68
	15	18	1300	1.3	1.82		
		T				1.29	2.95
							2.56
							2.63

TABLE 8-c
Experimental Results of 0.8 % C - 1.6 % Mn

Series	Growth rate mm/min	Distance mm	Temp. C	Between secon. Cmin	Between secon. Cmax	Between prim. Cmin	Between prim. Cmax
3	1.5	0.5	1460	1.26	1.8		
		2	1440	1.29	2.44		
		4.5	1400	1.27	2.06		
		6.5	1370	1.48	2.64		
		15	1235			1.34	2.42
		21	1140			1.39	1.95
		T				1.29	1.95
							2.16
	6	1	1460	1.26	1.75		
		4	1425	1.25	2.03		
		8	1380	1.26	3.04		2.86
		18	1250	1.27	2.21		
		21	1220	1.28	1.97	1.28	2.47
		T				1.27	2.74
							2.41
	15	0.5	1465	1.25	1.71		
		2	1450	1.26	1.85		
		4	1435	1.27	2.91		
		8.5	1390	1.28	2.47		2.67
		15.5	1315	1.3	2.52		
		22	1250	1.31	2.04	1.3	2.81
		T				1.29	2.35
							2.01
	30	1.5	1455	1.28	1.78		
		3	1445	1.29	1.85		
		7	1411	1.3	2.34		
		11	1380	1.31	2.16		2.57
		15	1335	1.3	1.79		
		22	1275	1.34	1.87		2.89
		T				1.28	3.24
							2.86
							2.63